IMPERIAL COLLEGE LONDON

UNIVERSITY OF LONDON

SOUND PROPAGATION IN LOSSLESS WAVEGUIDES COATED WITH ATTENUATIVE MATERIALS

by

Francesco Simonetti

A thesis submitted to the University of London for the degree of

Doctor of Philosophy

Imperial College London

Mechanical Engineering Department

Exhibition Road

London SW7 2AZ

October 2003

Abstract

Research into ultrasonic guided wave non-destructive testing for the long range inspection of large metallic structures is now well advanced. The main advantage of this method is that a large area can be covered from a given transducer position, so avoiding expensive scanning of all the structure surface. However, in the presence of attenuative coatings the test range can be dramatically reduced. As a consequence, it is of great practical interest to characterise those modes and frequencies which minimise the guided wave attenuation.

This thesis investigates the nature of shear horizontal (SH) and Lamb waves propagating in elastic plates coated with viscoelastic layers, this geometry being also representative of coated pipelines with large diameter to wall thickness ratio. For both SH and Lamb waves the mode which exhibits the highest potential for long range inspection purposes is identified and analysed. It is demonstrated that Lamb modes provide longer propagation distance than SH waves. Moreover, it is shown that the acoustic properties of the coating play a major role in the attenuation of the guided waves. In order to measure these properties for a broad variety of viscoelastic materials, two novel techniques are developed.

The bulk velocities and attenuation of the coating may be obtained by measuring the phase velocity and attenuation of guided waves propagating in a hollow waveguide filled with the viscoelastic material. This method is feasible when the material flows sufficiently easily for the cylinder to be filled. An alternative, when the material does not flow easily, is to clamp a sample of the coating between two rod waveguides and to measure the reflection and transmission of guided waves across the sample. This has enabled the acoustic properties of the bitumen used to provide corrosion protection on pipes in the chemical industry to be measured both when it is applied in its viscous liquid state and when it has been in place for many years and become solid.

Acknowledgements

I would like to express my gratitude to my supervisors Prof P. Cawley and Dr M. J .S. Lowe for their superb guidance and for creating a collaborative and intellectually stimulating research environment.

A special thanks goes to all my colleagues in the Nondestructive Testing Laboratory. In particular, I would like to thank, Dr M. Evans for being always ready to support me during the experimental work, Dr T. K. Vogt for many critical discussions and for the help provided with Latex, Mr J. Fong for sorting out the endless troubles with my PC and Dr A. Demma for introducing me to the group in November 2000.

Finally, I would like to thank my family and Yoko for standing by me at all times.

Contents

List of Figures

List of Tables

Nomenclature

a	complex sound velocity
b	half plate thickness
$\mathbf{b}$	unit vector parallel to the imaginary part of $\mathbf{k}$
c	bulk velocity
c_{ph}	phase velocity
$\mathbf{c}_1, \mathbf{c}_2, \mathbf{c}_3$	unit vectors of the frame of reference with coordinates x_1, x_2, x_3
d	plate thickness
e_s	SH wave peak strain energy per unit volume
E	SH wave peak strain energy
f	frequency
h_1, h_2, h_3	components of the mode shape
$\mathbf{H}$	vector potential
i	$\sqrt{-1}$
$Im\{\}$	imaginary part of the quantity
J_0, J_1	Bessel functions of the first kind
k_{im}	modulus of the imaginary part of $\mathbf{k}$
k_r	modulus of the real part of $\mathbf{k}$
$k_{\hat{r}}$	radial projection of $\mathbf{k}$
K	peak kinetic energy
$\mathbf{k}$	wavenumber vector
$\mathbf{n}$	unit vector parallel to the real part of $\mathbf{k}$
p_d	average dissipated power per unit volume
P_d	average dissipated power
P_{x_1}	complex power flow along x_1
$< P >$	average power flow along x_1
$\mathbf{P}$	Poynting vector
q	$\mathbf{k}$ component perpendicular to the plate
Q_{E}	SH wave first energy factor

Q_Δ	Lamb wave dilatational first energy factor
Q_Γ	Lamb wave distortional first energy factor
r, θ, z	cylindrical coordinates
R	reflection coefficient
$Re\{\}$	real part of the quantity
T	transmission coefficient
T_{ij}	stress tensor per unit density-wave amplitude product
u_1, u_2, u_3	displacement components in Crtesian coordinates
u_r, u_θ, u_z	displacement components in cylindrical coordinates
U	peak strain energy
V_{gr}	group velocity
x_1, x_2, x_3	Cartesian coordinates
X	non-dimensional frequency
$\mathbf{x}$	position vector
Y	non-dimensional attenuation
Y_0, Y_1	Bessel functions of the second kind
Z	impedance
α	bulk attenuation per unit length (np/m)
$\bar{\alpha}$	bulk attenuation per wavelength (np/wl)
γ	Lamb wave peak distortional strain energy per unit volume
Γ	Lamb Wave peak distortional strain energy
δ	Lamb wave peak dilatational strain energy per unit volume
δ_{ij}	Kronecker symbol
Δ	Lamb wave peak dilatational strain energy
ε_{ij}	strain tensor
ε_0	first strain tensor invariant
ζ	guided wave attenuation
η	correction factor

λ, μ	Lamé moduli
Λ	wavelength
ξ	$\mathbf{k}$ projection along the propagation direction
$\bar{\xi}$	non dimensional ξ
Π	second energy factor
ρ	density
σ_{ij}	stress tensor
$\tau_{r\theta}, \tau_{z\theta}$	tangential shear stresses
Υ	real part of the axial projection of $\mathbf{k}$
ϕ	scalar potential
χ	generalized impedance
ω	angular frequency
Ω	non dimensional frequency
$\times$	vector product
$\cdot$	scalar product
$*$	conjugate
∇	three-dimensional differential operator
im	subscript, denotes the imaginary part
r	subscript, denotes the real part
s	subscript, refers to shear type waves
l	subscript, refers to longitudinal type waves
v	subscript/superscript denote viscoelastic
e	subscript/superscript denote elastic
Bold typeface	denotes a vector.

Chapter 1

Introduction

1.1 Motivation

The extraordinary development of new and advanced technologies over the past century has boosted the growth of non-destructive testing (NDT) leading to a well established engineering discipline. In order to assess structural integrity, residual life and so to ensure higher safety standards, NDT methods have been tailored to suit the inspection requirements of a large variety of structures and materials. In this context, ultrasound has been playing a major role as leading technique for the detection of flaws and for the characterisation of the mechanical properties of a wide range of materials.

More recently, new technologies employing ultrasonic guided waves have been developed for the long range inspection of large metallic structures. These techniques are particularly advantageous since the acoustic signal is guided by the structure so a large length of one dimensional structures (such pipes) or area of two dimensional structures (like plates) can be inspected. (Note that for lossless one dimensional structures the signal propagates without being attenuated, while in two dimensional structures, the signal decays approximately with the square root of the distance [1]).

The detection of flaws is achieved by exciting the acoustic guided wave at one location of the structure and by looking at the echoes produced by the defects. Moreover, in contrast with traditional NDT techniques which are based on the propagation of

Figure 1.1: Typical oil steel pipeline coated with bitumen.

longitudinal and shear bulk waves, a broad range of guided waves can be excited. Depending on the geometry of the structure, on the position of the defects and on the surrounding environment, a mode can be selected in order to obtain the highest sensitivity. The use of either extensional [2, 3, 4, 5, 6, 7, 8, 9, 10, 11, 12, 13, 14] or distortional [15, 16] modes for inspecting small diameter heat exchangers, large diameter pipelines and storage tank plates has been studied extensively and screening devices have been designed and commercialized for routine testing [17, 18].

In the oil, gas, chemical and petro-chemical industries highly attenuative materials, such as bitumen, are often used as coatings in order to protect pipe networks from corrosion as shown in Fig. 1.1. The possibility of performing long range inspection of these systems with guided waves is very attractive since with conventional ultrasonic NDT the scanning of the entire pipeline surface would be required. The scanning which can be performed from outside the pipe, provided the coating is removed, or from the inside with a so called "pig" (a mechanical device which moves inside the pipe) is time consuming and often prohibitively expensive. For instance, the introduction of the pig inside a pipe carrying liquids requires the shutdown of the pipeline and maneuverability issues arise in proximity of bends and cross section variations. On the other hand, guided waves could overcome all these problems since guided

Figure 1.2: Transducer array employed for guided wave inspection of pipelines.

modes can be excited from outside the pipe by means of an array of transducers which occupies only a few square centimeters of the pipe surface as shown in Fig. 1.2. As a consequence, tests could be carried out by removing a limited portion of the coating while the pipeline is still in service. However, the full potential of guided waves can only be exploited if the acoustic signal propagates for a sufficiently large distance while maintaining an energy level higher than the background noise. The presence of attenuative coatings, as in the case of bitumen coated pipelines, can dramatically attenuate the signal due to the conversion of the mechanical energy of the wave into heat. As a consequence, there is an urgent need for the characterisation of the attenuation of guided waves propagating in metallic structures coated with lossy materials in order to maximise the distance over which flaws can be detected.

The aim of this thesis is to investigate the feasibility of long range guided wave inspection of metallic structures coated with bitumen, by identifying those modes and frequencies which minimise the guided wave attenuation. It should be emphasized that the extensive use of metallic structures with adhesive joints in the automotive and aerospace industries together with the need for vibration damping and electrical insulation have led to a massive presence of metallic structures coated with attenuative materials. Therefore, even though the direct application of the study

conducted in this thesis is the inspection of coated pipelines, the results are applicable to a large number of NDT problems.

1.2   Thesis outline

For pipe testing, longitudinal and torsional guided waves are commonly employed. Moreover, since the vast majority of coated pipelines is characterised by large diameter to wall thickness ratio, the effects of the pipe curvature on the guided modes are negligible (see for instance [19]) and the propagation of torsional and longitudinal modes in pipes is equivalent to the propagation of shear horizontal (SH) and Lamb waves in plates, respectively. Therefore, this thesis will focus on the characterisation of the attenuation of SH and Lamb waves propagating in elastic plates coated with viscoelastic layers.

There have been few studies on this subject. Jones [20] and Laperre [21] considered the propagation of Lamb waves in bilayered elastic plates but they did not explore the effects of internal losses. On the other hand, the influence of a Newtonian viscous fluid layer on the dispersion of Lamb waves in metallic plates was investigated by Zhu et al. [22], Yapura et al. [23] and by Nayfeh [24]. However, the hypothesis of a viscous liquid fails to model the material adequately when the shear elasticity cannot be neglected.

The thesis is divided into several Chapters each of them dealing with a particular subject. References on specific topics are given in the relevant Chapters.

Since guided waves can be thought of as a superposition of bulk waves opportunely polarized, Chapter 2 provides a review of the basic concepts of bulk wave propagation in viscoelastic materials and emphasizes the differences with the elastic case.

Chapter 3 is a comprehensive analysis of SH wave propagation in elastic plates coated with viscoelastic layers. The phase velocity and guided wave attenuation as

a function of the frequency (dispersion curves) are studied for a perfectly elastic bilayer and for the same system with low and large material damping.

In Chapter 4 the study of SH waves is extended to the case of Lamb waves, by considering the same bilayer as in Chapter 2. Moreover, as Lamb waves originate from the superposition of longitudinal and shear bulk waves (while SH waves depend on shear bulk waves only), the effects of the longitudinal and shear material damping on the attenuation of Lamb waves are taken into account separately.

In Chapter 5 the dispersion curves of SH and Lamb waves are compared in order to identify the best test conditions for long range inspections. Moreover, while the dispersion curves presented in Chapters 3 and 4 always refer to a particular geometry and mechanical properties of the bilayer, in this Chapter approximate non-dimensional dispersion curves are derived. These curves enable the prediction of the guided wave attenuation of either extensional or distortional modes propagating in any bilayer.

In Chapter 6 an anomalous behaviour of Lamb waves observed in Chapter 5 is explained by considering the propagating and nonpropagating modes of the elastic bilayer.

The guided wave attenuation is strongly dependent on the material properties of the coating, as will be shown in Chapters 3, 4 and 5. However, due to the lack of techniques able to measure the properties of highly attenuative materials, in Chapter 7 a novel method for the characterisation of the acoustic properties of fluid viscoelastic materials is presented. This technique allows the properties of bitumen coatings to be measured when it is applied in its liquid state.

Due to the fact that the properties of viscoelastic materials are extremely sensitive to temperature variations and oxidation phenomena which strongly depend on the surrounding environment, there is a need for a technique which allows rapid in-situ measurements of the coating properties to be performed. These measurements to-

gether with the non-dimensional curves derived in Chapter 7 would enable a quick estimate of the maximum distance over which defects can be detected. However, the main difficulty comes from the limited dimensions of samples (typically the size of a coin) due to the breakage of the coating as it is detached from the metallic substrate. To overcome this problem in Chapter 8 a new technique for the measurement of the properties of solid viscoelastic materials is presented.

The main conclusions of the thesis are summarised in Chapter 10 where possible future applications are illustrated.

Chapter 2

Bulk wave propagation in viscoelastic materials

2.1   Background

The aim of this Chapter is to introduce wave propagation in unbounded attenuative materials. This is an important step towards the understanding of sound propagation in waveguides since guided waves originate from the reverberations of bulk waves within the waveguide.

The behaviour of a bulk wave can be substantially different depending on whether the propagation occurs in a lossy or a perfectly elastic medium. In particular, well known properties of elastic waves, such as the coincidence between phase and energy propagation directions, no longer apply to viscoelastic waves.

The theoretical model employed to account for material damping and the properties of viscoelastic waves are discussed and compared with the elastic case. Moreover, the definition of the material acoustic properties is provided.

2.2 Equations of motion for linear viscoelastic materials

Viscoelasticity is universally recognised as the most suitable approach for introducing material damping, being able to represent the hysteretic nature of attenuative materials. This subject has attracted considerable attention over the past century and comprehensive treatises are provided in a number of textbooks (see, for example, Christensen [25], Haddad [26]).

The mechanical energy required to statically deform a viscoelastic material is in part stored as strain energy, which can be released when the sample is unloaded, and in part is converted into heat. The conversion mechanism is due to the complex nature of viscoelastic materials in which a number of internal processes such as bond breakage and bond formation occur. The main implication of these phenomena is that the response of the material depends on the sample deformation-time history rather than on the instantaneous value of the strain as in the case of elastic materials (this is the reason why it is said that viscoelastic materials have "memory"). The theory of linear viscoelasticity provides the simplest model to account for such a hysteretic behaviour.

Let us consider an isotropic and homogeneous viscoelastic medium and a system of Cartesian coordinates $\{O, x_1, x_2, x_3\}$. According to the linear viscoelastic theory, the stress tensor, σ_{ij}, at a given time, t, is given by

$$\sigma_{ij}(t) = \delta_{ij} \int_{-\infty}^{t} \lambda(t - \tau) \frac{d\varepsilon_{kk}(\tau)}{d\tau} d\tau + 2 \int_{-\infty}^{t} \mu(t - \tau) \frac{d\varepsilon_{ij}(\tau)}{d\tau} d\tau, \qquad (2.1)$$

where δ_{ij} is the Kronecker symbol and ε_{ij} is the strain tensor given by

$$\varepsilon_{ij} = \frac{1}{2} \left(\frac{\partial u_i}{\partial x_j} + \frac{\partial u_j}{\partial x_i} \right), \qquad (2.2)$$

where u_i is the displacement component along $\hat{x}_i$. The functions $\lambda(t)$ and $\mu(t)$ are the Lamé relaxation functions, which provide the stress relaxation in the material when a step deformation is applied. As an example, the function $\mu(t)$ can be measured by applying a state of pure shear deformation, ε_{12}, to a material sample

$$\varepsilon_{12}(t) = h(t), \qquad (2.3)$$
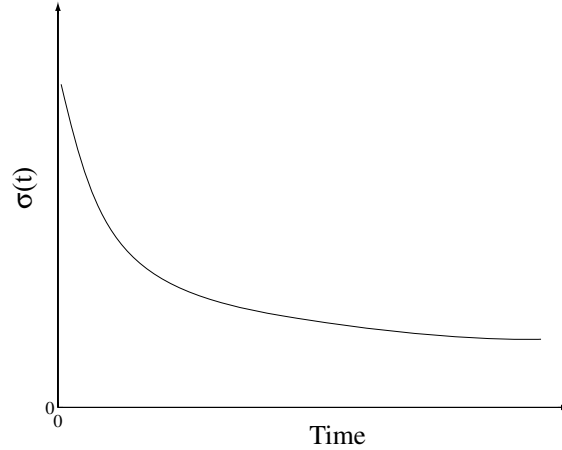
Figure 2.1: Schematic representation of the relaxation phenomenon.

where h(t) is the Heaviside function. If the material were elastic, the stress would instantaneously rise to the shear modulus of the material and then remain constant with time. On the other hand, for a viscoelastic material, the stress is maximum at $t = 0$ and then decays monotonically as shown schematically in Fig. 2.1. The stress-time curve provides the relaxation curve

$$\mu(t) = \sigma_{12}(t). \tag{2.4}$$

Depending on whether the asymptotic value of this curve is zero or not the material is referred to as viscoelastic fluid or viscoelastic solid, respectively.

The constitutive equations (2.1) are based on the assumption that the effect of an arbitrary deformation history can be thought of as a superposition of the relaxations of elementary deformation increments, which satisfy (2.4), taken separately. Therefore, the stress field corresponding to an arbitrary deformation history can be determined from two relaxation functions only [i.e. $\lambda(t)$ and $\mu(t)$].

Let us now consider the equations of motion for a continuous medium in the absence of body forces

$$\rho \ddot{u}_i = \sigma_{ij,j}, \tag{2.5}$$

where ρ is the material density and the subscript $,j$ represents the partial derivative $\partial/\partial x_j$. These equations represent through the constitutive equations (2.1) and the

compatibility equations (2.2) a system of integro-differential equations in the three unknown displacement components u_i. However, it can be observed that by taking the Fourier transform of (2.5) the system reduces to a linear set of differential equations

$$(\tilde{\lambda} + \tilde{\mu})\nabla(\nabla \cdot \mathbf{u}) + \tilde{\mu}\nabla^2\mathbf{u} + \rho\omega^2\mathbf{u} = 0, \tag{2.6}$$

where ω is the angular frequency, ∇ the three-dimensional differential operator and $\mathbf{u}$ is the Fourier transform of the displacement field. Note that in the rest of this thesis only the Fourier transform of all the time dependent functions (displacements, stresses etc.) are considered, unless explicitly specified. The linearity of (2.6) is a consequence of the constitutive equations (2.1) and the convolution theorem which, in the frequency domain, lead to constitutive relationships which are formally equivalent to those of the elastic case

$$\sigma_{ij} = \tilde{\lambda}\delta_{ij}\varepsilon_{kk} + 2\tilde{\mu}\varepsilon_{ij}, \tag{2.7}$$

with

$$\tilde{\lambda}(\omega) = \lambda_\infty + i\omega\int_0^\infty \Big(\lambda(t) - \lambda_\infty\Big)e^{i\omega t}dt, \tag{2.8}$$

$$\tilde{\mu}(\omega) = \mu_\infty + i\omega\int_0^\infty \Big(\mu(t) - \mu_\infty\Big)e^{i\omega t}dt, \tag{2.9}$$

where λ_∞ and μ_∞ are the asymptotic values of the relaxation curves.

It is interesting to observe that in the time domain, in order to characterise monochromatic wave propagation, the functions $\mu(t)$ and $\lambda(t)$ need to be known over the entire time domain $[0 \quad \infty]$. On the other hand, by replacing the time dependence with the frequency through the Fourier transform, a monochromatic wave is completely characterised by two parameters only, i.e. $\tilde{\lambda}$ and $\tilde{\mu}$. Moreover, these constants can directly be measured by means of experimental techniques which provide the values of $\tilde{\lambda}$ and $\tilde{\mu}$ either at a single frequency or over wide frequency ranges.

2.3   Solution to the wave equation

By using the Helmholtz decomposition [27] the displacement field can be expressed as a sum of the gradient of a compressional scalar potential, ϕ, and the curl of an equivoluminal vector potential, $\mathbf{H}$,

$$\mathbf{u} = \nabla\phi + \nabla \times \mathbf{H}, \tag{2.10}$$

with

$$\nabla \cdot \mathbf{H} = 0. \tag{2.11}$$

By substituting (2.10) into (2.6) the equations of motion break down into two uncoupled equations for the two unknown potentials

$$a_{\mathrm{L}}^2 \nabla^2 \phi + \omega^2 \phi = 0, \tag{2.12}$$

$$a_{\mathrm{S}}^2 \nabla^2 \mathbf{H} + \omega^2 \mathbf{H} = 0, \tag{2.13}$$

where the frequency-dependent complex velocities a_{L} and a_{S} are given by

$$a_{\mathrm{L}}^2 = \frac{\tilde{\lambda} + 2\tilde{\mu}}{\rho}, \tag{2.14}$$

$$a_{\mathrm{S}}^2 = \frac{\tilde{\mu}}{\rho}. \tag{2.15}$$

For an unbounded space the solution to (2.12) and (2.13) are

$$\phi = \phi_0 e^{-i\mathbf{k}_{\mathrm{L}} \cdot \mathbf{x}}, \tag{2.16}$$

$$\mathbf{H} = \mathbf{H}_0 e^{-i\mathbf{k}_{\mathrm{S}} \cdot \mathbf{x}}, \tag{2.17}$$

where ϕ_0 and $\mathbf{H}_0$ are arbitrary constants and $\mathbf{k}_{\mathrm{L,S}}$ are the wavenumber vectors which have to satisfy the secular equations

$$\mathbf{k}_{\mathrm{L,S}} \cdot \mathbf{k}_{\mathrm{L,S}} = \frac{\omega^2}{a_{\mathrm{L,S}}^2}. \tag{2.18}$$

In general $\mathbf{k}$ is a complex vector which can be divided into its real and imaginary parts

$$\mathbf{k} = k_r \mathbf{n} - i k_{im} \mathbf{b}, \tag{2.19}$$

where $\mathbf{n}$ and $\mathbf{b}$ are the unit vectors directed parallel to the real and imaginary parts of $\mathbf{k}$, respectively. As a consequence, the secular equation becomes

$$k_r^2 - 2i k_r k_{im} \mathbf{n} \cdot \mathbf{b} - k_{im}^2 = \frac{\omega^2}{a^2}. \tag{2.20}$$

This equation admits an infinite number of solutions depending on the angle between the vectors $\mathbf{n}$ and $\mathbf{b}$. Note that $\mathbf{k}$ is frequency dependent because ω appears explicitly in (2.20) and implicitly in the complex velocity a. The next two subsections discuss the displacement and stress fields associated with viscoelastic bulk waves.

2.3.1 Displacement fields

The displacement field corresponding to ϕ is irrotational ($\nabla \times \nabla \phi = 0$) and is given by

$$\mathbf{u}_{\mathrm{L}} = \nabla \left(\phi_0 e^{-i\mathbf{k}_{\mathrm{L}} \cdot \mathbf{x}} \right) = A \left(\mathbf{n} - i\frac{k_{im}}{k_r}\mathbf{b} \right) e^{-k_{im}\mathbf{b} \cdot \mathbf{x}} e^{-ik_r\mathbf{n} \cdot \mathbf{x}}, \tag{2.21}$$

where A is an arbitrary constant. Expression (2.21) describes the motion of a bulk longitudinal wave. The quantity $(\mathbf{n} - ik_{im}/k_r\mathbf{b})$ indicates the polarization of the displacement, the exponential $exp(-k_{im}\mathbf{b} \cdot \mathbf{x})$ represents the decay of the wave, which is maximum along $\mathbf{b}$ while $exp(-ik_r\mathbf{n} \cdot \mathbf{x})$ accounts for the phase propagation along $\mathbf{n}$ and leads to the definition of the phase velocity c_{ph}

$$c_{ph} = \frac{\omega}{k_r}. \tag{2.22}$$

Let us now calculate the displacement field associated with $\mathbf{H}$. It can be observed that by applying the condition $\nabla \cdot \mathbf{H} = 0$ to (2.17) two cases are possible. First, the vector potential can be written as

$$\mathbf{H}_0 = h_0\mathbf{e}, \tag{2.23}$$

where $\mathbf{e}$ is a unit vector belonging to $\Re^3$ and h_0 is a complex scalar constant. The condition $\nabla \cdot \mathbf{H} = 0$ requires that $\mathbf{H}_0$ is perpendicular to the plane described by $\mathbf{n}$ and $\mathbf{b}$

$$\mathbf{H}_0 \cdot \mathbf{n} = 0 \quad \mathbf{H}_0 \cdot \mathbf{b} = 0, \tag{2.24}$$

and (2.17) can be rewritten as

$$\mathbf{H} = h_0 \frac{\mathbf{n} \times \mathbf{b}}{|\mathbf{n} \times \mathbf{b}|} e^{-i\mathbf{k}_{\mathrm{S}} \cdot \mathbf{x}}. \tag{2.25}$$

The second condition corresponds to the case in which $\mathbf{H}_0$ is a complex vector

$$\mathbf{H}_0 = h_{01}\mathbf{e_1} + ih_{02}\mathbf{e_2}, \tag{2.26}$$

where h_{01} and h_{02} are real constants, while $\mathbf{e_1}$ and $\mathbf{e_2}$ are unit vectors of $\Re^3$. Since $\mathbf{H}$ has to be equivoluminal, it follows that $\mathbf{e_1}$ and $\mathbf{e_2}$ have to be perpendicular to $\mathbf{n}$ and $\mathbf{b}$, respectively. Moreover, both the vectors are contained in the plane described by $\mathbf{n}$ and $\mathbf{b}$, thus

$$\mathbf{H} = h_0(\mathbf{n} \times \mathbf{b}) \times \left(\mathbf{n} - i\frac{k_{im}}{k_r}\mathbf{b}\right)e^{-ik_r\mathbf{n}\cdot\mathbf{x}}, \tag{2.27}$$

where h_0 is a complex scalar constant.

The displacement fields associated with the two vector potentials (2.25) and (2.27) are

$$\mathbf{u}_S^{sv} = B(\mathbf{n} \times \mathbf{b}) \times \left(\mathbf{n} - i\frac{k_{im}}{k_r}\mathbf{b}\right)e^{-k_{im}\mathbf{b}\cdot\mathbf{x}}e^{-ik_r\mathbf{n}\cdot\mathbf{x}}, \tag{2.28}$$

$$\mathbf{u}_S^{sh} = B(\mathbf{n} \times \mathbf{b})e^{-ik_r\mathbf{n}\cdot\mathbf{x}}, \tag{2.29}$$

where B is an arbitrary complex constant and the superscripts sv and sh refer to different polarizations. These expressions, which describe the propagation of bulk shear waves, are formally similar to (2.21) except for the polarizations which are perpendicular to that of (2.21). Note that the polarization of (2.28) is parallel to the plane describe by $\mathbf{b}$ and $\mathbf{n}$ whereas the polarization of (2.29) is perpendicular. Note also that (2.21) involves the longitudinal wavenumber, $\mathbf{k}_L$, while (2.28) (2.29) include the shear wavenumber $\mathbf{k}_S$.
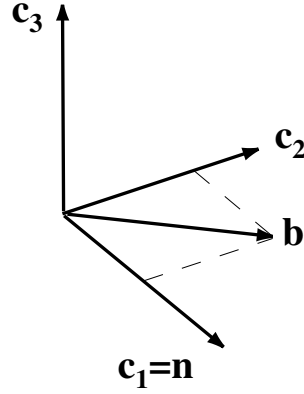
Figure 2.2: Frame of reference.

2.3.2 Characterisation of stresses and energy flux

In order to calculate the stress tensors is more convenient to introduce a frame of reference $\{O, \mathbf{c}_1, \mathbf{c}_2, \mathbf{c}_3\}$ in which $\mathbf{c}_1$ is parallel to $\mathbf{n}$, $\mathbf{c}_3 = \mathbf{n} \times \mathbf{b}$ and $\mathbf{c}_2 = -\mathbf{c}_1 \times \mathbf{c}_3$ as shown in Fig. 2.2. In such a frame, the components of the displacement field are

$$\mathbf{u}_{\mathrm{L}} = A_{\mathrm{L}} \begin{bmatrix} 1 \\ \frac{\mathbf{k}_{\mathrm{L}} \cdot \mathbf{c}_2}{\mathbf{k}_{\mathrm{L}} \cdot \mathbf{n}} \\ 0 \end{bmatrix} e^{-i\mathbf{k}_{\mathrm{L}} \cdot \mathbf{x}}, \tag{2.30}$$

$$\mathbf{u}_{\mathrm{S}}^{sv} = A_{\mathrm{S}}^{sv} \begin{bmatrix} -\frac{\mathbf{k}_{\mathrm{S}} \cdot \mathbf{c}_2}{\mathbf{k}_{\mathrm{S}} \cdot \mathbf{n}} \\ 1 \\ 0 \end{bmatrix} e^{-i\mathbf{k}_{\mathrm{S}} \cdot \mathbf{x}} \tag{2.31}$$

$$\mathbf{u}_{\mathrm{S}}^{sh} = A_{\mathrm{S}}^{sh} \begin{bmatrix} 0 \\ 0 \\ 1 \end{bmatrix} e^{-i\mathbf{k}_{\mathrm{S}} \cdot \mathbf{x}}. \tag{2.32}$$

$$\tag{2.33}$$

The stress tensors can be derived through the constitutive equations (2.7) by substituting the displacement expressions (2.30), (2.31) and (2.32)into (2.2)

$$\sigma_{\text{L}} = -iA_{\text{L}} \begin{bmatrix} \tilde{\lambda}\frac{\mathbf{k}\cdot\mathbf{k}}{\mathbf{k}\cdot\mathbf{n}} + 2\tilde{\mu}\mathbf{k}\cdot\mathbf{n} & 2\tilde{\mu}\mathbf{k}\cdot\mathbf{c}_2 & 0 \\ 2\tilde{\mu}\mathbf{k}\cdot\mathbf{c}_2 & \tilde{\lambda}\frac{\mathbf{k}\cdot\mathbf{k}}{\mathbf{k}\cdot\mathbf{n}} + 2\tilde{\mu}\frac{(\mathbf{k}\cdot\mathbf{c}_2)^2}{\mathbf{k}\cdot\mathbf{n}} & 0 \\ 0 & 0 & \tilde{\lambda}\frac{\mathbf{k}\cdot\mathbf{k}}{\mathbf{k}\cdot\mathbf{n}} \end{bmatrix} e^{-i\mathbf{k}\cdot\mathbf{x}}, \tag{2.34}$$

$$\sigma_{\text{S}}^{sv} = -i\tilde{\mu}A_{\text{S}}^{sv} \begin{bmatrix} -2\mathbf{k}\cdot\mathbf{c}_2 & \frac{(\mathbf{k}\cdot\mathbf{n})^2-(\mathbf{k}\cdot\mathbf{c}_2)^2}{\mathbf{k}\cdot\mathbf{n}} & 0 \\ \frac{(\mathbf{k}\cdot\mathbf{n})^2-(\mathbf{k}\cdot\mathbf{c}_2)^2}{\mathbf{k}\cdot\mathbf{n}} & 2\mathbf{k}\cdot\mathbf{c}_2 & 0 \\ 0 & 0 & 0 \end{bmatrix} e^{-i\mathbf{k}\cdot\mathbf{x}}, \tag{2.35}$$

$$\sigma_{\text{S}}^{sh} = -i\tilde{\mu}A_{\text{S}}^{sh} \begin{bmatrix} 0 & 0 & \mathbf{k}\cdot\mathbf{n} \\ 0 & 0 & \mathbf{k}\cdot\mathbf{c}_2 \\ \mathbf{k}\cdot\mathbf{n} & \mathbf{k}\cdot\mathbf{c}_2 & 0 \end{bmatrix} e^{-i\mathbf{k}\cdot\mathbf{x}}. \tag{2.36}$$

$$\tag{2.37}$$

The characterisation of the stress and displacement fields enables the study of the energy carried by a bulk wave. Most importantly, for a prescribed direction of the phase propagation, $\mathbf{n}$, it is now possible to study how the energy propagates in the surrounding space. This can be done by means of the complex Poynting vector [28], $\mathbf{P}$, which is defined in analogy with the electromagnetic case and is given by

$$P_j = -\frac{v_i^* \sigma_{ij}}{2}, \tag{2.38}$$

where v_i is the velocity component along $\hat{x}_i$ ($v_i = i\omega u_i$) and the superscript $*$ refers to complex conjugate of the quantity. The energy rate per unit area across an elementary surface $d\Sigma$ with normal $\mathbf{y}$ can be characterised by the scalar product $\mathbf{P}\cdot\mathbf{y}$. The real part of $\mathbf{P}\cdot\mathbf{y}$ coincides with the average of the power flow along $\mathbf{y}$ over one cycle [28]. On the other hand, the imaginary part is the peak reactive power which accounts for the instantaneous energy flux [28].

In order to study the energy propagation the real part of the Poynting vector has to be considered, as this provides the direction of maximum power flow. Moreover, since a wave propagates energy and not matter, the propagation direction has to coincide with the direction of the real part of $\mathbf{P}$.

The following expressions provide the Poynting vectors of longitudinal and shear bulk waves.

$$\mathbf{P}_{\mathrm{L}} = \frac{1}{2}\omega|A_{\mathrm{L}}|^2 \begin{bmatrix} \tilde{\lambda}\frac{\mathbf{k}\cdot\mathbf{k}}{\mathbf{k}\cdot\mathbf{n}} + 2\tilde{\mu}\frac{|\mathbf{k}|^2}{(\mathbf{k}\cdot\mathbf{n})^*} \\ \frac{\mathbf{k}\cdot\mathbf{c}_2}{|\mathbf{k}\cdot\mathbf{n}|^2}\left(-\tilde{\lambda}\mathbf{k}\cdot\mathbf{k} + 2\tilde{\mu}|\mathbf{k}|^2\right) \\ 0 \end{bmatrix} e^{-2k_{im}\mathbf{b}\cdot\mathbf{x}}. \tag{2.39}$$

$$\mathbf{P}_{\mathrm{s}}^{sv} = \frac{1}{2}\omega\tilde{\mu}|A_{\mathrm{s}}^{sv}|^2 \begin{bmatrix} \frac{1}{|\mathbf{k}\cdot\mathbf{n}|^2}\left(2|\mathbf{k}\cdot\mathbf{c}_2|^2\mathbf{k}\cdot\mathbf{n} + (\mathbf{k}\cdot\mathbf{n})|\mathbf{k}\cdot\mathbf{n}|^2 - (\mathbf{k}\cdot\mathbf{c}_2)^2(\mathbf{k}\cdot\mathbf{n})^*\right) \\ \frac{\mathbf{k}\cdot\mathbf{c}_2}{|\mathbf{k}\cdot\mathbf{n}|^2}\left((\mathbf{k}\cdot\mathbf{n})^2 + |\mathbf{k}\cdot\mathbf{c}_2|^2 + 2|\mathbf{k}\cdot\mathbf{n}|^2\right) \\ 0 \end{bmatrix} e^{-2k_{im}\mathbf{b}\cdot\mathbf{x}}, \tag{2.40}$$

$$\mathbf{P}_{\mathrm{s}}^{sh} = \frac{1}{2}\omega\tilde{\mu}|A_{\mathrm{s}}^{sh}|^2 \begin{bmatrix} \mathbf{k}\cdot\mathbf{n} \\ \mathbf{k}\cdot\mathbf{c}_2 \\ 0 \end{bmatrix} e^{-2k_{im}\mathbf{b}\cdot\mathbf{x}}. \tag{2.41}$$

It can be observed that the Poynting vector belongs to the plane described by $\mathbf{b}$ and $\mathbf{n}$ as $P_3 = 0$. Moreover, its direction does not depend on the position vector, $\mathbf{x}$. This means, that in any point of the space the energy always propagates in the same direction. However, the exponential decay $exp(-2k_{im}\mathbf{b}\cdot\mathbf{x})$, which is present in all the expressions, shows that the wave is attenuated with distance due to the conversion of mechanical energy into heat.
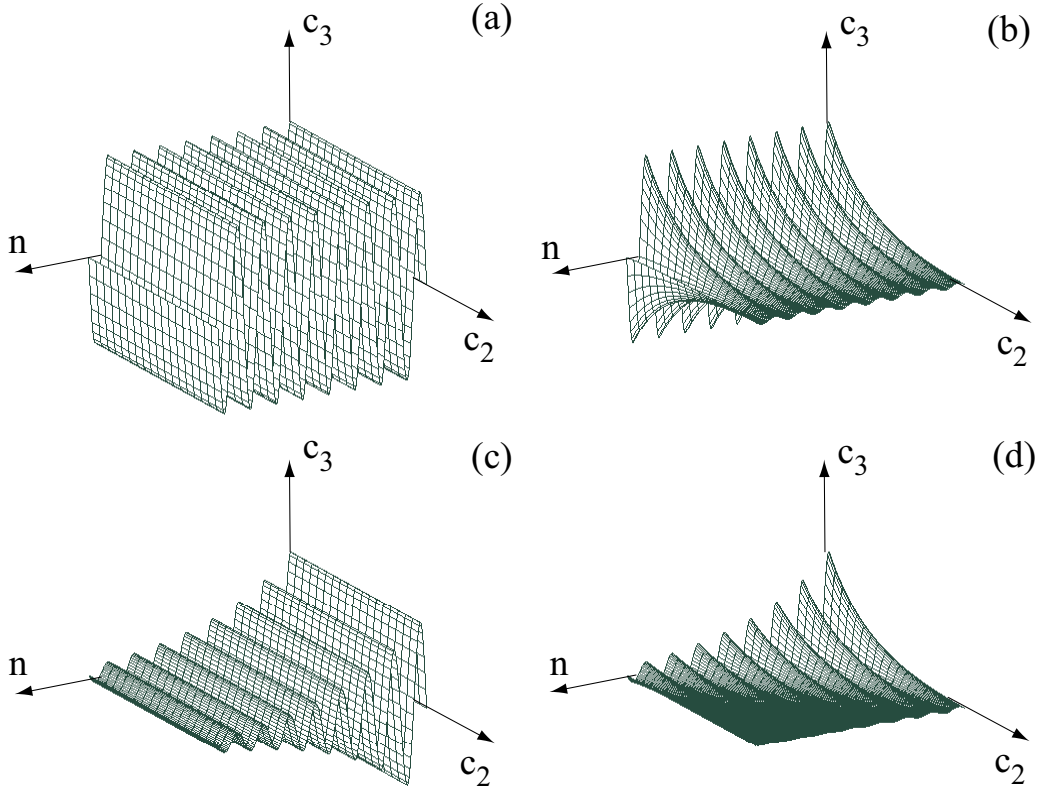
Figure 2.3: Wave fields over the plane $x_3 = 0$: (a) plane elastic wave; (b) evanescent elastic wave; (c) viscoelastic wave with $\mathbf{n} \parallel \mathbf{b}$; (d) viscoelastic wave with $\mathbf{n} \times \mathbf{b} \neq \mathbf{0}$.

2.4 Comparison between elastic and viscoelastic waves

The viscoelastic model presented in the previous sections is a generalization of the theory of elasticity. As a consequence, the wave propagation in elastic media can be derived from the former expressions by assuming that the quantities $\tilde{\mu}$ and $\tilde{\lambda}$ are real. The aim of this section is to show the main differences between elastic and viscoelastic bulk waves.

When $\tilde{\mu}$ and $\tilde{\lambda}$ are real, the velocities $a_{\mathrm{L,s}}$ are also real and the wavenumber solution to the secular equation (2.20) can be either real or complex.

A real wavenumber corresponds to the case of plane wave propagation and is related

to the acoustic velocities $a_{\mathrm{L,S}}$ by a simple expression

$$\mathbf{k} = \frac{\omega}{a_{\mathrm{L,S}}}\mathbf{n}. \tag{2.42}$$

Note that since k_{im} vanishes, the vector $\mathbf{b}$ can be in any direction. Moreover, from (2.30), (2.31) and (2.32) it follows that longitudinal waves are polarized parallel to the direction $\mathbf{n}$ while shear waves have polarization perpendicular to $\mathbf{n}$.

Furthermore, both the real and imaginary parts of the Poynting vector are always parallel to $\mathbf{n}$ as can be deduced from (2.39), (2.40) and (2.41)(note that $\mathbf{k} \cdot \mathbf{c}_2 = 0$). As a result, the propagation direction coincides with $\mathbf{n}$. Figure 2.3a shows a typical distribution of the field functions associated with a plane wave over the plane $x_3 = 0$.

The complex solutions to (2.20) correspond to evanescent waves. In this case, since the right hand term in (2.20) is real, $\mathbf{n}$ and $\mathbf{b}$ have to be perpendicular and the secular equation becomes

$$k_r^2 - k_{im}^2 = \frac{\omega^2}{a^2}. \tag{2.43}$$

Longitudinal and shear evanescent waves have displacement components in both $\mathbf{n}$ and $\mathbf{b}$ directions, expressions (2.30) and (2.31), or along $\mathbf{c}_3$ only (2.29) as in the case of plane waves. The wave fields exponentially decay along $\mathbf{b}$, the typical field distribution being shown in Fig. 2.3b. However, the real part of the Poynting vector is still parallel to $\mathbf{n}$. This can be shown by observing that in (2.39), (2.40) and (2.41) the second row is always imaginary ($\mathbf{k} \cdot \mathbf{c}_2 = -ik_{im}$). As a consequence, along the directions perpendicular to $\mathbf{n}$ the average power flow vanishes, while the peak reactive power is non zero. Therefore, it can be concluded that in the elastic case the propagation direction and phase propagation direction are always coincident. It has to be emphasized that this is a consequence of the elastic hypothesis only. For a viscoelastic material, the real part of the Poynting vector is never parallel to $\mathbf{n}$ [see, (2.39) (2.40) and (2.41)], unless $\mathbf{b}$ is parallel to $\mathbf{n}$. This is shown in Fig. 2.4 which provides the angle between the real part of $\mathbf{P}$ and $\mathbf{n}$ as a function of the angle between $\mathbf{n}$ and $\mathbf{b}$. This curve refers to the case of a shear wave propagating in a highly attenuative viscoelastic medium ($\mu = 0.18 + i0.13 \quad GPa$ and $\rho = 1200 Kg/m^3$) at $50 kHz$ and polarized parallel to the plane described by $\mathbf{b}$ and $\mathbf{n}$. When $\mathbf{b}$ is parallel
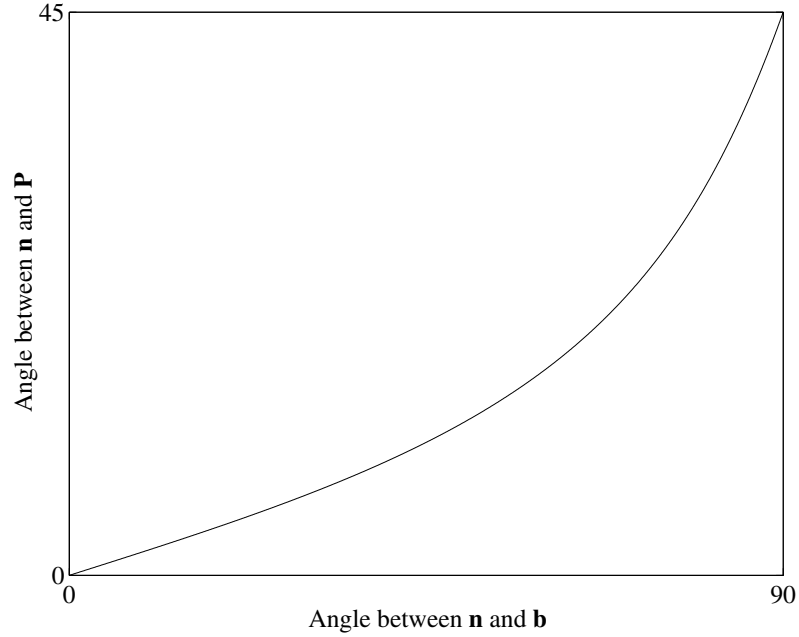
Figure 2.4: Angle formed between the real part of the Poynting vector and **n** versus the angle between **n** and **b** for a shear bulk wave propagating in a viscoelastic material.

to **n**, the power flows along **n**. However, as the angle between **b** and **n** increases, **P** rotates. The maximum angle between **P** and **n** is $\pi/4$ and is reached when **b** is perpendicular to **n**. However, this is a limit condition as **b** and **n** can never be perpendicular for a viscoelastic material [see eq. (2.20)]. Moreover, Fig. 2.4 shows that the direction of the Poynting vector is always between **b** and **n**.

Figure 2.3c shows the field distributions for a viscoelastic bulk wave when **b** is parallel to **n**. In this case the wave fields decay along **n** only. Moreover, the Poynting vector is parallel to **n**. On the other hand, when $\mathbf{n} \times \mathbf{b} \neq 0$ (Fig. 2.3d) the wave fields are exponentially damped along **n** and $\mathbf{c}_2$, and the Poynting vector is directed somewhere between **n** and **b**.

2.5 Acoustic properties of viscoelastic materials

The acoustic behaviour of an isotropic and homogeneous viscoelastic medium is completely characterised by four real, frequency dependent parameters, which can be related to the two complex Lamé moduli, as pointed out in Sec. 2.2. Since longitudinal and shear waves are independent acoustic responses of the medium, it follows that the acoustic properties have to be specified in terms of longitudinal and shear waves. On the other hand, for a prescribed material, an infinite number of bulk waves can propagate depending on the angle between $\mathbf{b}$ and $\mathbf{n}$. However, if this angle is fixed the wavenumber becomes uniquely linked to the material properties. On the basis of such an argument, the acoustic properties are defined by considering the case in which $\mathbf{b}$ and $\mathbf{n}$ are parallel (Fig. 2.3c). It should be emphasized that such a definition is due to experimental reasons, since the ideal condition of parallelism between $\mathbf{b}$ and $\mathbf{n}$ is the easiest to achieve during laboratory experiments. Moreover, this definition includes the case of elastic materials for which the acoustic properties are defined by considering shear and longitudinal plane waves (see Fig. 2.3a).

The acoustic properties are given in terms of phase velocity, c, and attenuation, α, of longitudinal and shear bulk waves, the attenuation corresponding to the imaginary part of the wavenumber

$$c_{\mathrm{L,S}} = \frac{\omega}{Re\{k_{\mathrm{L,S}}\}} \qquad \alpha_{\mathrm{L,S}} = -Im\{k_{\mathrm{L,S}}\} \qquad \mathbf{b} \parallel \mathbf{n}, \qquad (2.44)$$

where $Re\{\cdot\}$ and $Im\{\cdot\}$ refer to the real and imaginary parts of the quantity. In the following, the phase velocity c will be referred to as the bulk velocity and α as the bulk attenuation (np/unit length or dB/unit length). Note that the bulk velocities and attenuations are frequency dependent since $\mathbf{k}_{\mathrm{L,S}}$ also depend on the frequency. The attenuation can alternatively be expressed in terms of Neper per wavelength (np/wl), $\bar{\alpha}$.

$$\bar{\alpha} = \alpha \Lambda, \qquad (2.45)$$

where Λ is the wavelength. This definition turns useful for those materials whose attenuation per unit length is a linear function of the frequency while the bulk velocity is mainly constant with frequency, since $\bar{\alpha}$ becomes constant.

The bulk velocity and attenuation can be related to the complex velocities (2.14) and (2.15) through (2.20)

$$a_{\mathrm{L,S}} = \frac{c_{\mathrm{L,S}}}{1 - i\frac{\alpha_{\mathrm{L,S}} c_{\mathrm{L,S}}}{\omega}},\tag{2.46}$$

which also allow the acoustic properties to be related to the Lamé moduli through (2.14) and (2.15).

2.6 Summary

The theory of bulk wave propagation in viscoelastic media and a comparison with the elastic case have been presented.

In the viscoelastic case bulk waves can be divided into longitudinal and shear waves. The longitudinal displacement field is irrotational while the shear one is equivolu-minal. Moreover, for an elastic wave the propagation direction and the phase prop-agation direction are always coincident, whereas in the viscoelastic case this only occurs when the real and imaginary parts of the wavenumber vector are parallel.

Chapter 3

SH wave propagation in bilayers

3.1 Background

This Chapter addresses the dispersion of shear horizontal (SH) waves propagating in metallic plates coated with viscoelastic layers. The results obtained for this type of geometry can be extended to the case of torsional waves propagating in hollow cylinders with large diameter to wall thickness ratio as discussed in Chapter 1.

The dispersion of SH waves is due to the frequency dependence of the acoustic properties of the viscoelastic layer (see Chapter 2) and to the interaction between the wavelength and the geometry of the bilayer. Previous studies have considered the propagation of Lamb waves in an elastic plate bordered with a viscous liquid [23, 22]. However, the hypothesis of a viscous liquid does not consider the shear elasticity of the material. Moreover, while for a Newtonian fluid the frequency dependence of the acoustic properties is known as a function of the viscosity, for a viscoelastic material it is not possible to state a general frequency dependence which can take into account all the different viscoelastic materials (the generalized Kelvin-Voigt, or Maxwell models depend on an infinite number of parameters).

While the frequency dependence of the viscoelastic material cannot be predicted, the effect of the interaction between the wavelength and the geometry can be studied by using an ideal frequency dependence model for the acoustic properties of the viscoelastic layer. The ideal model takes into account the elasticity and the damping

of the material separately. In particular, the elasticity is considered by assuming that the bulk velocity is independent of the frequency (as in the case of perfectly elastic materials) whereas the damping is taken into account by considering a bulk material attenuation linearly proportional to the frequency. As the acoustic properties of a generic viscoelastic material can always be thought of as a perturbation of the ideal model, it follows that the dispersion curves of the ideal bilayer can also be generalized through a perturbation procedure.

The dispersion equation for SH wave propagation in bilayers is derived in Sec. 3.2. In order to study the interaction between the wavelength and the geometry of the bilayer, the possibility of relating the attenuation of SH modes to the energy distribution over the cross section of the bilayer, considered to be elastic, is investigated in Sec. 3.3. The dispersion curves of the elastic bilayer are studied in Sec. 3.4. The effects of low material damping are considered in Sections 3.5 and 3.6 while large material absorption is examined in Sec. 3.7.

3.2   SH waves in bilayered plates

Let us consider an elastic and isotropic plate of infinite extent in the $\hat{x}_2$ direction and a viscoelastic layer rigidly coupled together (Fig. 3.1). Shear horizontal waves in multilayered systems are given by the superposition of bulk shear waves [of the form (2.29)] polarized parallel to the boundaries of the layers and with the vectors **b** and **n** parallel to the plane $x_2 = 0$. In particular, in the case of the bilayer, the solution is obtained by considering one pair of bulk waves in each layer (see Fig. 3.1). These waves are frequently referred to as partial waves [29].

The Lamé moduli can be expressed as a function of the complex velocities, $a_{\mathrm{L,S}}$, and the density by inverting (2.14) and (2.15), it follows that the stress tensor (2.7) can be regarded as the product of the density, a suitable tensor T_{ij} which depends on
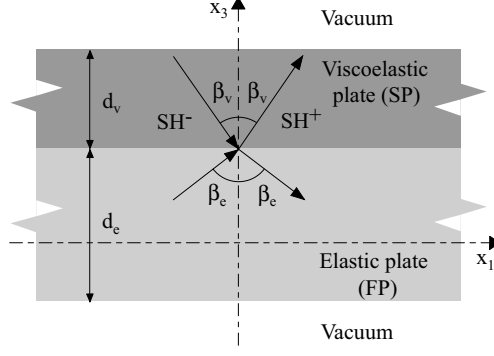
Figure 3.1: Partial waves diagram.

the bulk velocities only and the amplitude, A, of the bulk wave

$$\sigma_{ij} = \rho \mathrm{T}_{ij} A, \tag{3.1}$$

$$\mathrm{T}_{ij} A = (a_{\mathrm{L}}^2 - 2a_{\mathrm{S}}^2)\delta_{ij}\varepsilon_0 + 2a_{\mathrm{S}}^2\varepsilon_{ij}. \tag{3.2}$$

The secular equation for the bilayer can be found by imposing continuity of stress and displacement at the interface between the two layers, and the zero traction condition at the free boundaries of the bilayer [30]. This leads to a system of four equations in the four unknown bulk shear wave amplitudes, $A^{\mathrm{SH}_{v,e}^{\pm}}$

$$\begin{bmatrix} \mathrm{T}_{3,2_{top}}^{\mathrm{SH}_v^+} & \mathrm{T}_{3,2_{top}}^{\mathrm{SH}_v^-} & 0 & 0 \\ u_{2_{int}}^{\mathrm{SH}_v^+} & u_{2_{int}}^{\mathrm{SH}_v^-} & -u_{2_{int}}^{\mathrm{SH}_e^+} & -u_{2_{int}}^{\mathrm{SH}_e^-} \\ \frac{\rho_v}{\rho_e}\mathrm{T}_{3,2_{int}}^{\mathrm{SH}_v^+} & \frac{\rho_v}{\rho_e}\mathrm{T}_{3,2_{int}}^{\mathrm{SH}_v^-} & -\mathrm{T}_{3,2_{int}}^{\mathrm{SH}_e^+} & -\mathrm{T}_{3,2_{int}}^{\mathrm{SH}_e^-} \\ 0 & 0 & \mathrm{T}_{3,2_{bot}}^{\mathrm{SH}_e^+} & \mathrm{T}_{3,2_{bot}}^{\mathrm{SH}^-e} \end{bmatrix} \begin{bmatrix} A^{\mathrm{SH}_v^+} \\ A^{\mathrm{SH}_v^-} \\ A^{\mathrm{SH}_e^+} \\ A^{\mathrm{SH}_e^-} \end{bmatrix} = 0, \tag{3.3}$$

where the subscripts v and e refer to the viscoelastic and elastic layers respectively, while the signs $\pm$ indicate the upward and downward directions of the bulk waves, respectively. Since the displacement is polarized parallel to $\hat{x}_2$ and is constant along this direction, it follows that the stress on the planes $x_3 = const.$ is parallel to $\hat{x}_2$. The first row in the equation (3.3) gives the traction free condition on the top of the bilayer, the second and third provide the continuity of displacement and stress at the interface respectively, and the last gives the traction free condition at the bottom of the bilayer. The system (3.3) admits non trivial solutions only if the determinant of the matrix vanishes. This condition provides the secular equation for SH waves in bilayered plates.

The phase velocity of the resulting guided wave is

$$c_{ph} = \frac{\omega}{Re\{\xi\}},\tag{3.4}$$

where ξ is the projection of the wavenumber along the interface (ξ is an invariant for all the partial waves as Snell's law holds). Moreover, the $-Im\{\xi\}$ gives the guided wave attenuation, ζ. Furthermore, the Fourier transformed displacement field has the form

$$u_2(x_1, x_3, \omega) = h_2(qx_3)e^{-\zeta x_1}e^{-i\frac{\omega}{c_{ph}}x_1},\tag{3.5}$$

where the function h_2 is the mode shape and q the wave number projection along the $\hat{x}_3$ direction (q is different in the two layers).

3.3 Guided wave attenuation

Since the guided wave attenuation depends on the amount of energy dissipated in the viscoelastic layer, it is of crucial importance to investigate the relationship between the mechanical energy, the guided wave attenuation, ζ, and the acoustic properties of the viscoelastic layer. This analysis can be carried out by means of the complex acoustic Poynting's theorem [28]. According to this theorem, for a volume, V, bounded by the closed surface, S, the sum of the net flux of the complex Poynting vector into S and the average power dissipated over one cycle within V, P_d, equals the Fourier transformed time derivative of the difference between the peak strain energy, U, stored in V and the peak kinetic energy, K, contained in the same volume giving

$$\oint_S \mathbf{P} \cdot \mathbf{y}dS - i\omega(U - K) + P_d = 0,\tag{3.6}$$

where $\mathbf{y}$ is the outward normal to S and $\mathbf{P}$ is the Poynting vector (2.38). The real part of the complex Poynting vector flux is the average net power flow into S over one cycle [28]. Moreover, by considering the real part of eq. (3.6) it follows that the dissipated power, P_d, equals in magnitude the average power flow through S (since U, E and P_d are real). This allows the guided wave attenuation to be linked to
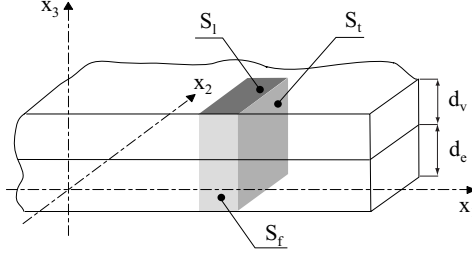
Figure 3.2: Volume considered for the energy balance.

the energy dissipation. In order to determine this relationship for the bilayer, let us calculate the net flux into a rectangular parallelepiped of unit width in the $\hat{x}_2$ direction, and with height equal to the thickness of the bilayer (see Fig. 3.2). As the stress field can be related to the displacement field through the complex Lamé constants, by substituting (3.5) into (2.38) the flux through a transversal surface perpendicular to $\hat{x}_1$, S_t, at the position x_1 can be written as

$$P_{x_1} = \frac{1}{2}\omega\xi e^{-2\zeta x_1} \int_{d_e+d_v} \left(\tilde{\mu} \mid h_2(qx_3) \mid^2 \right) dx_3. \tag{3.7}$$

Moreover, the flux through each lateral surface perpendicular to $\hat{x}_3$, S_l, is zero as the stresses vanish on the free surfaces of the bilayer. Furthermore, the flow across the faces perpendicular to $\hat{x}_2$, S_f, vanishes as the stress is perpendicular to the displacement along these surfaces. As a result, the total flow through the parallelepiped, which corresponds to the integral in eq. (3.6), is the difference between the fluxes calculated at the two transversal surfaces. Moreover, by considering the real part of (3.6), the power balance can be written as

$$\Delta Re\{P_{x_1}\} + P_d = 0, \tag{3.8}$$

where Δ refers to the difference between the power flows through the transversal surfaces. Expression (3.8) indicates that the power flow decay along the propagation direction equals the power loss. Moreover, while for an elastic bilayer a mode is propagating only above its cutoff frequency and is not propagating below it [31], for a bilayer with internal damping a mode is always propagating. If there were nonpropagating modes (zero in-plane power flow), the in-plane average power flow would be zero by the definition of nonpropagating modes and consequently, from (3.8) the power loss would be zero, which is physically inconsistent.

By substituting (3.7) into (3.8) and differentiating with respect to x_1 one obtains

$$\zeta = \frac{\frac{dP_d}{dx_1}}{2Re\{P_{x_1}\}}, \tag{3.9}$$

which provides the guided wave attenuation as the ratio of the average dissipated power per unit volume over the average in-plane power flow per unit width.

Generally speaking, at a prescribed point of a viscoelastic medium, the average dissipated power per unit volume can be related to the peak strain energy per unit volume [28]. In particular, for SH waves the peak strain energy per unit volume, e_s, is

$$e_s = 2\tilde{\mu}_r^v(\varepsilon_{12}\varepsilon_{12}^* + \varepsilon_{23}\varepsilon_{23}^*), \tag{3.10}$$

in which the subscript r refers to the real part of the quantity. On the other hand, the average dissipated power per unit volume, p_d, is given by

$$p_d = 2\omega\tilde{\mu}_{im}^v(\varepsilon_{12}\varepsilon_{12}^* + \varepsilon_{23}\varepsilon_{23}^*), \tag{3.11}$$

where the subscript im refers to the imaginary part of the quantity. Since for the bilayer all the field functions are constant along the $\hat{x}_2$ direction it follows that the total power dissipated in V has to satisfy

$$\frac{dP_d}{dx_1} = \int_{d_v} p_d dx_3 = \omega\frac{\mu_{im}^v}{\mu_r^v}\int_{d_v} e_s dx_3 = \omega\frac{\mu_{im}^v}{\mu_r^v}\frac{dE}{dx_1}, \tag{3.12}$$

where E is the peak strain energy of the portion of the viscoelastic layer contained in V

$$\frac{dE}{dx_1} = \int_{d_v} 2\tilde{\mu}_r^v(\varepsilon_{12}\varepsilon_{12}^* + \varepsilon_{23}\varepsilon_{23}^*)dx_3. \tag{3.13}$$

As a result, the guided wave attenuation can be expressed as

$$\zeta = \frac{1}{2}\omega\frac{\tilde{\mu}_{im}^v}{\tilde{\mu}_r^v}Q_E, \tag{3.14}$$

where

$$Q_E = \frac{\frac{dE}{dx_1}}{<P>}, \tag{3.15}$$

is the first energy factor. (Q_E has been termed an energy factor as this gives an appreciation of its application). It follows that the guided wave attenuation is

proportional to the first energy factor multiplied by the ratio of the imaginary to the real part of $\tilde{\mu}^v$. Generally speaking, Q_{E} also depends on $\tilde{\mu}^v$ as the wavenumbers and the mode shapes contained in (3.13) and (3.7) depend on $\tilde{\mu}^v$. However, for weakly attenuative materials $\tilde{\mu}_{im}^v$ is considerably smaller than $\tilde{\mu}_r^v$. As a consequence, in the first order approximation the guided wave attenuation can be related to the first energy factor of the elastic bilayer (obtained by assuming $\tilde{\mu}^v = \tilde{\mu}_r^v$) by considering the Maclaurin expansion of the function $\zeta(\tilde{\mu}_{im}^v)$ up to the first order

$$\zeta \simeq \frac{1}{2}\omega \frac{\tilde{\mu}_{im}^v}{\tilde{\mu}_r^v} Q_{\mathrm{E}}\big|_{\tilde{\mu}_{im}^v=0} . \tag{3.16}$$

However, (3.16) does not provide the guided wave attenuation when the frequency is lower than the cutoff frequency of the elastic mode to which Q_{E} refers. At these frequencies, the power flow P_{x_1} is purely imaginary as the elastic mode is nonpropagating. As a consequence, Q_{E} becomes singular and the Maclaurin expansion can no longer be employed. Nevertheless, the guided wave attenuation can be still related to the nonpropagating modes. For this purpose, it is sufficient to consider the imaginary part of Poynting's theorem (3.6) which, by following an argument similar to that employed for obtaining eq. (3.8), leads to another expression for the energy balance

$$\Delta Im\{P_{x_1}\} - \omega(U - K) = 0. \tag{3.17}$$

By differentiating this expression with respect to x_1 and by taking into account (3.7), a new expression for the guided wave attenuation is obtained

$$\zeta = \omega \frac{\frac{d}{dx_1}(U - K)}{2Im\{P_{x_1}\}}, \tag{3.18}$$

which relates the energy decay to the guided wave attenuation. As a consequence, the guided wave attenuation can be expressed as a function of the second energy factor, Π

$$\zeta = \frac{1}{2}\omega\Pi, \tag{3.19}$$

where Π is defined according to

$$\Pi = \frac{\frac{d}{dx_1}(U - K)}{Im\{P_{x_1}\}}. \tag{3.20}$$

In a similar fashion to the earlier approximation of equation (3.14), the guided wave attenuation in the case of low loss materials can be approximated by considering the Maclaurin series of the function $\zeta(\tilde{\mu}_{im}^v)$ up to zero order

$$\zeta \simeq \frac{1}{2}\omega\Pi\big|_{\tilde{\mu}_{im}^v=0} \,, \tag{3.21}$$

which allows the guided wave attenuation to be derived from the nonpropagating modes of the elastic bilayer. Since ζ is the projection of the imaginary part of the wavenumber along the interface, $\Pi\big|_{\tilde{\mu}_{im}^v=0}$ can be obtained from the value of the imaginary part of the wavenumber of the non propagating mode through (3.21)

$$\Pi = \frac{2}{\omega}\xi\big|_{\tilde{\mu}_{im}^v=0} \,. \tag{3.22}$$

It follows that, under the zero order approximation, the guided wave attenuation in the attenuative system corresponds to the projection of the wavenumber of the nonpropagating mode of the corresponding elastic system along the interface.

The energy factors, Q_{E} and Π, allow the attenuation of the lossy bilayer modes to be derived from the elastic theory, once the frequency domain of each elastic mode is divided into the nonpropagating and propagating regions. Moreover, while in the nonpropagating region the zero order approximation is valid for low loss materials, in the second region the first order approximation is needed (the zero order approximation would give zero guided wave attenuation). This type of approach suggests that the guided wave attenuation can be studied by considering two different regimes of material damping which can be classified as low and high attenuation regimes respectively. In the first regime, the zero and first order approximations are allowed, and the guided wave attenuation can be predicted by using the two energy factors, Q_{E} and Π, while in the high attenuation regime, higher order terms in the Maclaurin expansion have to be taken into account.

The results obtained so far are based on a monochromatic approach. As a consequence, they are valid whatever the frequency dependence of the material is. However, as the goal of this Chapter is the understanding of the effects of the viscoelastic layer on the dispersion of the free elastic plate, it is necessary to derive a theory which, starting from the dispersion curves of the elastic bilayer leads, through some

approximation, to the dispersion of the attenuative bilayer. Here, it has been shown that at a given frequency the guided wave attenuation can be derived from the energy factors of the elastic bilayer which is obtained by setting the imaginary part of the shear modulus of the viscoelastic layer to zero, with the real part remaining unchanged. Strictly speaking, this bilayer is artificially elastic as the frequency dependence of the shear modulus requires the existence of its imaginary part as can be deduced from the Kramers-Krönig relationship [32]. However, it is always possible to assume that the real part of $\tilde{\mu}^v$ consists of the sum of a constant part and a frequency dependent term

$$\tilde{\mu}_r^v = \mu_0^v + \mu_1^v(\omega). \tag{3.23}$$

The dispersion of the pseudo elastic bilayer (obtained by considering the frequency dependent real part of $\tilde{\mu}^v$), can be obtained as a perturbation of the dispersion of an equivalent elastic bilayer which is defined as the bilayer with $\tilde{\mu}^v = \mu_0^v$. The perturbation term, Q_p, can be calculated by employing the Taylor expansion of the generic energy factor Q (either Q_{E} or Π)

$$Q(\omega, \tilde{\mu}_r^v) = Q(\omega, \mu_0^v) + \sum_{m=1}^{\infty} \frac{1}{m!} \frac{\partial Q^{(m)}}{\partial \tilde{\mu}_r^v} (\mu_1^v(\omega))^m, \tag{3.24}$$

in which the series in the right hand term is Q_p. As a result, the dispersion of the guided wave can be regarded, in the zero and first order approximation, as a superposition of the guided wave attenuation due to the equivalent elastic bilayer plus the guided wave attenuation due to the perturbation term Q_p. However, weakly attenuative materials are characterised by $\tilde{\mu}_r^v$ being only slightly dispersive, which implies that Q_p is negligible whenever the zero and first order approximations hold.
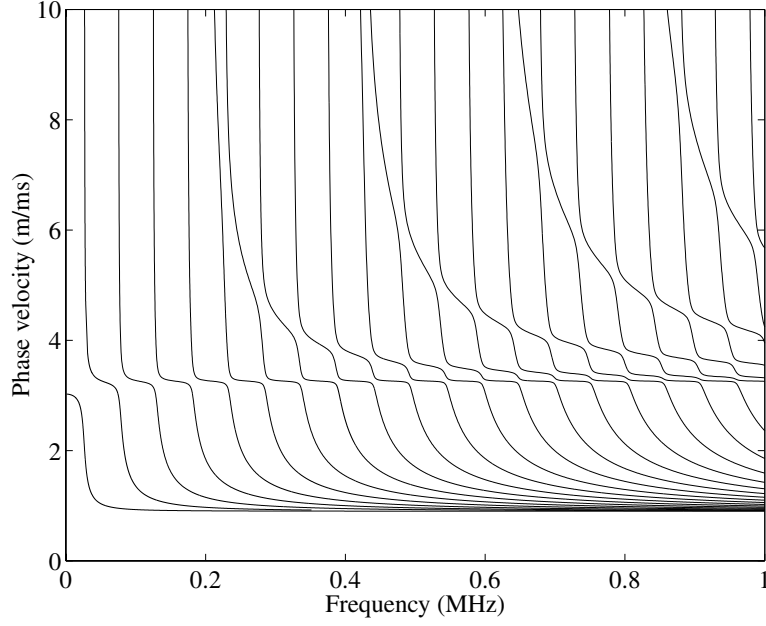
Figure 3.3: Phase velocity dispersion curves for the elastic bilayer described in table 3.1 with $\bar{\alpha}_{\mathrm{S}} = 0$.

3.4 SH modes in elastic bilayers

Since the bulk shear velocities of viscoelastic materials are lower than those of metals, in the rest of this Chapter the metallic plate is referred to as the "fast plate" (FP) while the viscoelastic layer is termed the "slow plate" (SP).

For elastic materials, the characteristic equation (3.3) can be rewritten as (see, for instance, Nayfeh [33])

$$\sin(d_{\mathrm{F}}q_{\mathrm{F}})\cos(d_{\mathrm{S}}q_{\mathrm{S}})\frac{q_{\mathrm{F}}}{q_{\mathrm{S}}} + \cos(d_{\mathrm{F}}q_{\mathrm{F}})\sin(d_{\mathrm{S}}q_{\mathrm{S}})\frac{\mu_{\mathrm{S}}}{\mu_{\mathrm{F}}} = 0, \qquad (3.25)$$

where the subscripts S and F refer to the slow and fast plates respectively; $d_{\mathrm{F,S}}$ are the thicknesses of the plates. It should be emphasised that only the shear properties of the bilayer are involved in the propagation of SH waves. Therefore, in the rest of this chapter, all the bulk velocities and attenuations are meant to be of the shear type, and the subscript S always refers to the slow layer. The quantities $q_{\mathrm{F,S}}$ are the projections of the wavenumber along the normal to the bilayer, $\hat{x}_3$. Moreover, the trigonometric functions are complex as their arguments are in general complex.
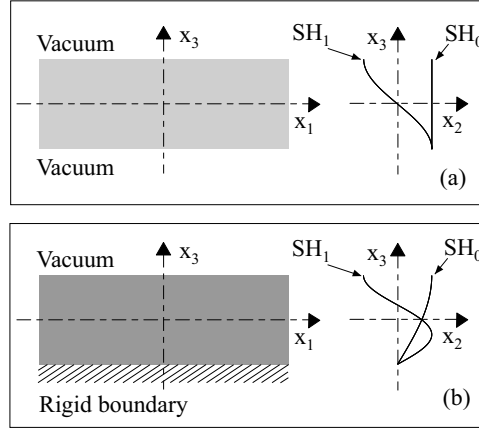
Figure 3.4: Different boundary conditions and corresponding displacement fields for the first two modes: (a) free plate; (b) clamped-free plate.

Figure 3.3 shows typical dispersion curves of all the propagating modes in the range of frequency from 0 to $1MHz$ for the bilayer whose acoustic properties and geometry are summarized in table 3.1, the attenuation in the slow layer being neglected. The curves have been traced by using Disperse [34] which essentially solves eq. (3.25). By contrast with the case of a single free plate, for the bilayer it is not possible to express the phase velocity as a function of the frequency-thickness product only. Therefore, all the dispersion curves shown in this and in the next Chapter will refer to a specific geometry and acoustic properties of the bilayer, while in Chapter 5 approximate non-dimensional dispersion curves will be considered.

In order to characterise the dispersion curves of the bilayer, let us consider the modes of both the free SP and the free FP (Fig. 3.4a). SH wave propagation in free elastic plates represents the simplest case of guided waves, and the analytical expression

Table 3.1: Material and geometric properties of the bilayer used for the study of SH wave propagation.

	Shear velocity (m/s)	$\bar{\alpha}$ (np/wl)	ρ (Kg/m^3)	Thickness (mm)
Slow plate	900	0.10	1250	9.00
Fast plate	3260	-	7930	8.00
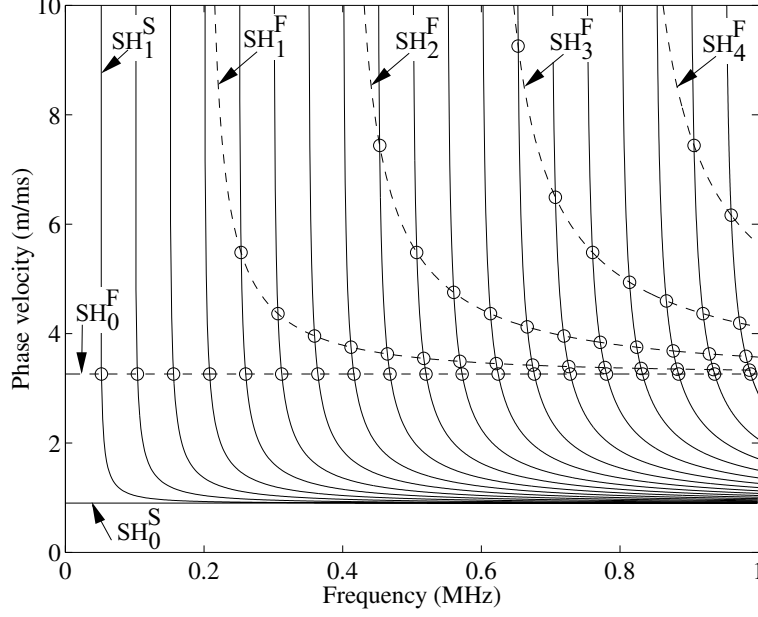
Figure 3.5: Phase velocity dispersion curves for the free plates (Tab. 3.1 with $\bar{\alpha}_\mathrm{S} = 0$): (———) slow plate; ($---$) fast plate; ($\circ$) transition points.

for the Nth order mode, SH_N, is given by [35]

$$\frac{f^2}{c^2} - \frac{f^2}{c_{ph}^2} = \left(\frac{N}{2d} \right)^2, \tag{3.26}$$

where $N \epsilon \{0, 1, 2, ...\}$, d and c are the thickness and the shear velocity of the plate respectively. As shown in Fig. 3.5 an infinite number of intersections between the modes of the FP and those of the SP occur. The frequencies, $f_{m,n}$, where the SH_m^F modes of the free FP intersect the SH_n^s modes of the free SP are given by

$$f_{m,n}^2 = \frac{c_\mathrm{F}^2 c_\mathrm{S}^2}{c_\mathrm{F}^2 - c_\mathrm{S}^2} \left[\left(\frac{n}{2d_\mathrm{s}} \right)^2 - \left(\frac{m}{2d_\mathrm{F}} \right)^2 \right]. \tag{3.27}$$

Since at the frequency $f_{m,n}$ the SH_m^F mode propagates at the same speed, $c_{phm,n}$, as SH_n^s, and as the stress vanishes on the boundaries, it follows that these two modes can also propagate in the joined plates. As a result, it is possible to conclude that the intersection points of the isolated plates belong to the modes of the bilayer. Moreover, these intersections are characterised by zero stress at the interface of the bilayer.

Of particular interest are the intersections of the SH_n^{S} modes with the SH_0^{F} mode, which occur at the frequencies

$$f_{0,n}^2 = \frac{c_{\mathrm{F}}^2 c_{\mathrm{S}}^2}{c_{\mathrm{F}}^2 - c_{\mathrm{S}}^2} \left(\frac{n}{2d_{\mathrm{s}}} \right)^2, \tag{3.28}$$

for $n \neq 0$. The frequencies provided by this expression coincide with the transition frequencies of Love waves. Love waves are SH waves propagating in a plate rigidly bonded to a half space and polarized parallel to the plate [36]. The transitions occur when the phase velocity equals the shear bulk velocity of the half space, which can happen only if the plate bulk velocity is lower than that of the half space. Below the transition frequency, energy leakage from the plate into the half space occurs. However, as the frequency reaches the transition value, no more leakage occurs and the wave energy is mainly trapped in the plate. A similar phenomenon occurs in the case of the bilayer. Above the transition frequency, the partial waves in the FP become evanescent and the guided wave energy is trapped in the slow layer. Since this effect occurs at all the intersections, in the rest of this Chapter, the term "transition frequency" is used with reference to all the frequencies provided by (3.27). Moreover, the term "transition point" refers to the points $(f_{m,n}, c_{phm,n})$ of the dispersion curves.

Let us consider the dispersion curves in the case in which only one face of the plate is free while the other is rigidly clamped (Fig. 3.4b). In this case the dispersion curve for the Mth order mode, SH'_M, is

$$\frac{f^2}{c^2} - \frac{f^2}{c_{ph}^2} = \left(\frac{2M+1}{4d} \right)^2, \tag{3.29}$$

where $M \epsilon \{0, 1, 2, ...\}$. Figure 3.6 shows the dispersion curves for both the FP and SP in the clamped-free case. The intersection of the $SH_m'^{\mathrm{F}}$ mode of the clamped-free FP with the $SH_n'^{\mathrm{S}}$ mode of the clamped-free SP occurs at

$$f'^2_{m,n} = \frac{c_{\mathrm{F}}^2 c_{\mathrm{S}}^2}{c_{\mathrm{F}}^2 - c_{\mathrm{S}}^2} \left[\left(\frac{n}{4d_{\mathrm{s}}} \right)^2 - \left(\frac{m}{4d_{\mathrm{F}}} \right)^2 \right]. \tag{3.30}$$

The intersections of the clamped-free plate modes also belong to the dispersion curves of the bilayer. At the frequency $f'_{m,n}$, the $SH_m'^{\mathrm{F}}$ mode propagates at the same phase velocity as $SH_n'^{\mathrm{S}}$. As a consequence, since the displacement at the clamped boundary vanishes, the two modes can also propagate if the clamps are removed and the plates are joined together. Moreover, at these frequencies the bilayer
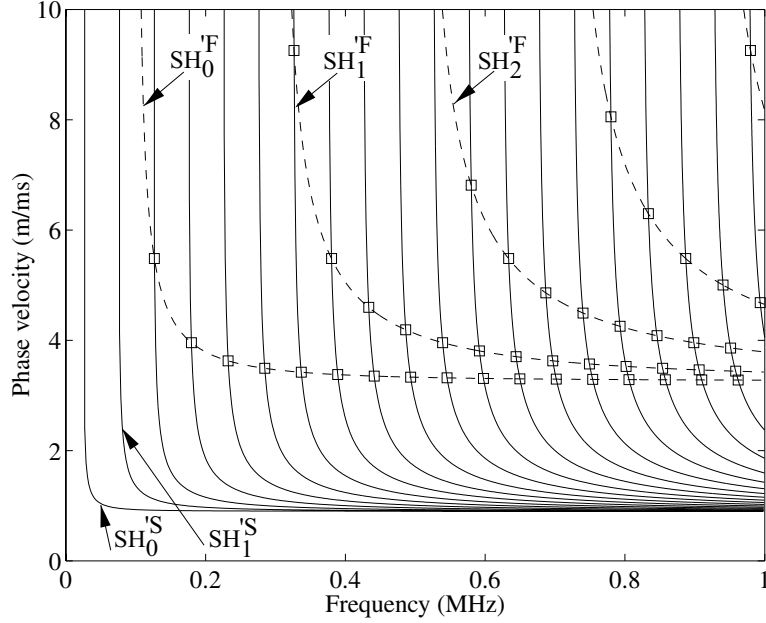
Figure 3.6: Phase velocity dispersion curves for clamped-free plates (Tab. 3.1 with $\bar{\alpha}_\mathrm{S} = 0$): (————) slow plate; $(---)$ fast plate; ($\square$) nodal points.

displacement field vanishes at the interface of the bilayer. In other words, at the frequencies $f'_{m,n}$, the interface is a nodal plane. For this reason, in the following, the intersection points of the clamped-free plate modes will be referred to as "nodal points" and the frequencies $f'_{m,n}$ as "nodal frequencies".

A further insight into the dispersion of SH modes in the bilayer is provided by an asymptotic solution obtained by considering the limit as the stiffness and the density of the FP go to infinity at constant shear velocity c_F. For this purpose, it can be observed that the matrix in (3.3) can be partitioned into four square matrices and the characteristic equation can be written according to

$$det \begin{bmatrix} \mathbf{C}_{11} & \mathbf{C}_{12} \\ \mathbf{C}_{21} & \mathbf{C}_{22} \end{bmatrix} = 0, \tag{3.31}$$

where the matrices $\mathbf{C}_{ij}$ have dimension 2×2. As a consequence, by considering the limit as the stiffness and the density of the FP go to infinity, the matrices $\mathbf{C}_{ij}$ remain unchanged except for $\mathbf{C}_{21}$ which vanishes (since $\rho_v/\rho_e \to 0$), since the displacements and the quantities T_{ij} depend only on the two bulk velocities. As a result, for this

asymptotic condition, the characteristic equation becomes [37]

$$det \begin{bmatrix} \mathbf{C}_{11} & \mathbf{C}_{12} \\ \mathbf{0} & \mathbf{C}_{22} \end{bmatrix} = det(\mathbf{C}_{11})det(\mathbf{C}_{22}) = 0, \tag{3.32}$$

which is satisfied if either $det(\mathbf{C}_{22}) = 0$ or $det(\mathbf{C}_{11}) = 0$. These conditions define two families of modes.

The first condition coincides with the characteristic equation for the free FP as $\mathbf{C}_{22}$ is a function of the stress on the two faces of the FP. The asymptotic modes belonging to this family are given by

$$q_{\mathrm{F}} = \frac{n\pi}{d_{\mathrm{F}}}. \tag{3.33}$$

The second condition corresponds to wave propagation in the SP if it were rigidly clamped at the interface. This is due to the fact that $\mathbf{C}_{11}$ is a function of the stress at the top of the bilayer and the displacement of the SP at the interface. Therefore the modes of the second family are characterised by

$$q_{\mathrm{S}} = \left(p - \frac{1}{2} \right) \frac{\pi}{d_{\mathrm{S}}}, \tag{3.34}$$

where p is an integer. The two families of asymptotic modes are shown in Fig. 3.7. It has to be emphasized that the asymptotic solution holds also in the case of attenuative bilayers since (3.3) has been derived for the general case of viscoelastic materials.

As the the stiffness and the density of the FP become large compared to those of the SP the dispersion curves of the bilayer tend to the asymptotic modes. However, the dispersion curves of the bilayer only intersect the asymptotic solution at specific points as shown in Fig. 3.8. The intersections with the first family occur at the transition points as they do not depend on the stiffness and density of the material (see equation (3.27)). For the same reason, the intersections with the second family occur at the nodal points.
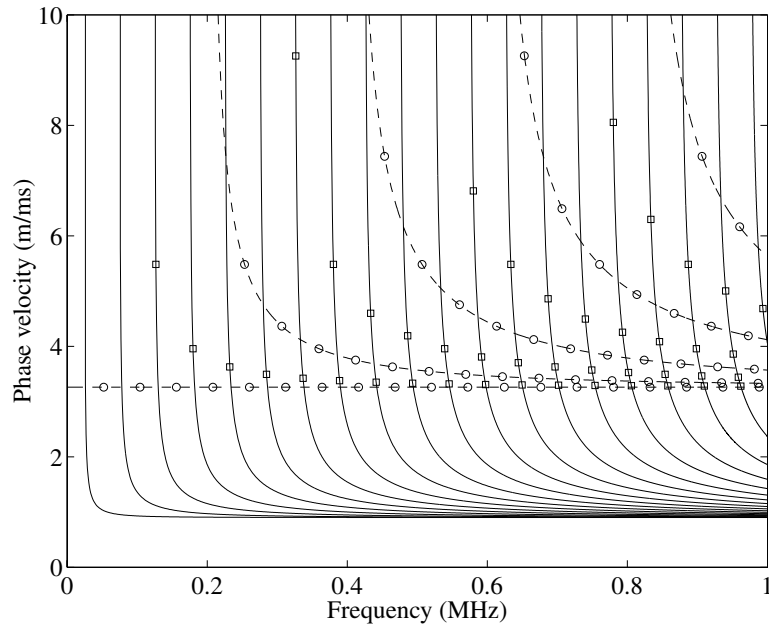
Figure 3.7: Phase velocity dispersion curves of the bilayer as the FP density and stiffness go to infinity at constant shear velocity: $(- - -)$ first family; (———) second family; $(\circ)$ transition points; $(\square)$ nodal points.
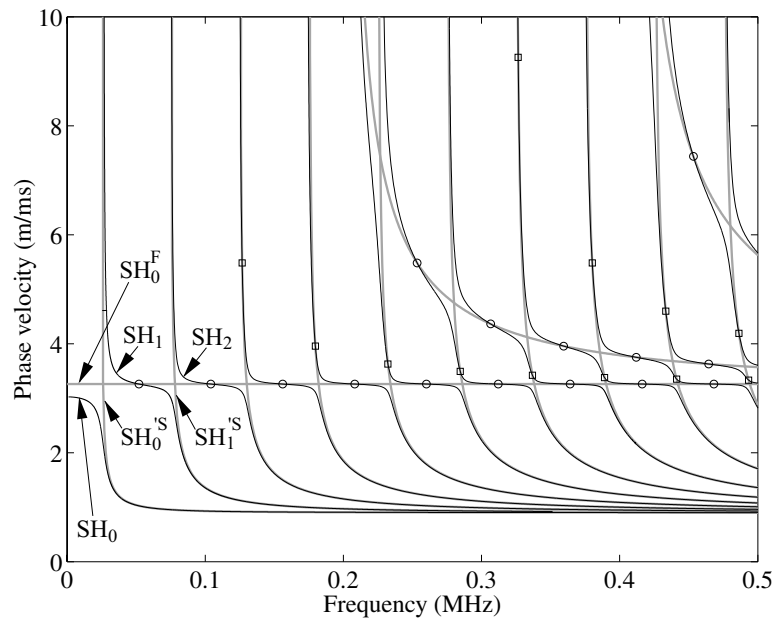
Figure 3.8: Phase velocity dispersion curves of the system of table 3.1 with $\bar{\alpha}_s = 0$: (———) asymptotic solution; (———) bilayer modes; $(\circ)$ transition frequencies; $(\square)$ nodal points.

The two families of asymptotic modes cross each other at several points but it is interesting to note that the dispersion curves for different modes of the bilayer (Fig. 3.3) never cross. Each mode follows a path close to that of the asymptotic solution but veers away from it at the points where modes for the different asymptotic families cross, as these points cannot belong to the bilayer mode.

This mode repulsion phenomenon is similar to that seen in Lamb waves. According to Überall *et al.* [38] the Lamb modes in a free plate can be regarded as an interaction between the modes of a fluid layer in vacuum (which has zero shear velocity) and those of an artificial layer in vacuum which only supports shear waves (with zero longitudinal velocity). The interaction results in the mode repulsion, which causes the change of a Lamb mode character from primarily longitudinal to primarily shear or vice versa.

It can be concluded that the modes of the elastic bilayer originate from the coupling of the modes of the free FP and those of the clamped-free SP (Fig. 3.4). Moreover, the coupling mechanism causes the jumping of a bilayer mode path between several asymptotic modes. For instance, as the frequency increases, the trajectory of the SH_1 mode jumps from the SH'^{S}_0 into the FP mode, SH^{F}_0, and then jumps again into the SH'^{S}_1 mode as shown in Fig. 3.8. In this thesis this phenomenon will be referred to as "mode jumping".
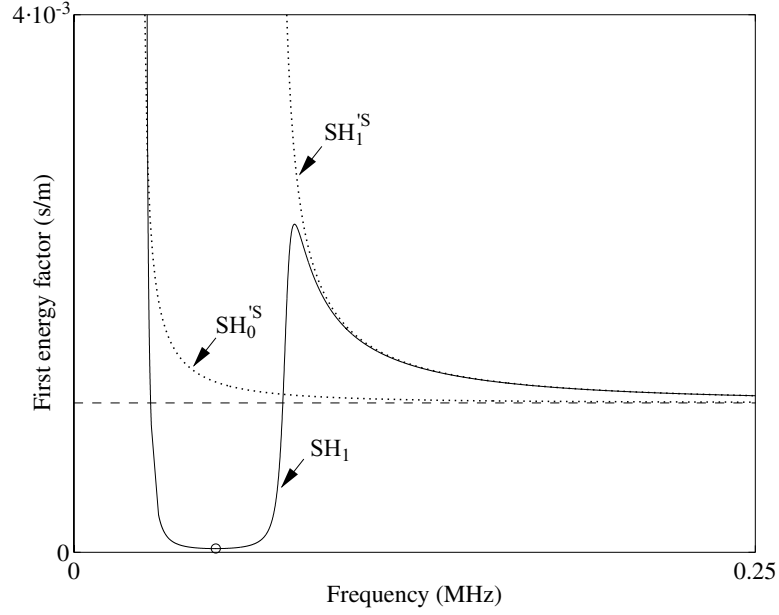
Figure 3.9: First energy factor for the SH_1 mode of the elastic bilayer defined in Tab. 3.1 with $\bar{\alpha}_{\mathrm{S}} = 0$: (———) bilayer; ($\cdots$) clamped-free SP; ($\circ$) transition frequency; ($---$) Q_{E} asymptotic.

3.5 Low material attenuation regime

In the low attenuation regime the zero and first order approximations are satisfactory and the perturbation factor of eq. (3.24) can be neglected. As a consequence, the frequency dependence of the guided wave attenuation can be analysed by studying the dispersion of the equivalent elastic bilayer factors Q_{E} and Π. Fig. 3.9 shows the first energy factor as a function of frequency for the SH_1 mode of the elastic bilayer studied in Sec. 3.4 (see Fig. 3.8). The dotted lines provide Q_{E} for the two asymptotic modes, SH'^{S}_0 and SH'^{S}_1, which best approximate SH_1. For the clamped-free configuration, the analytical expression for Q_{E} can be derived from (3.7) and (3.13)

$$Q_{\mathrm{E}} = \frac{c_{ph}}{c_s^2}, \tag{3.35}$$

where c_s is the shear velocity in the slow layer and the phase velocity is related to the frequency by (3.29).

As the frequency goes to infinity, the SH_1 mode of the bilayer tends to the SH'^{S}_1

mode of the clamped-free SP and, as a consequence, Q_E of the SH_1 mode tends to Q_E of the SH'^S_1 mode. Since the phase velocity of SH'^S_1 tends to c_s, it follows that

$$\lim_{f\to\infty} Q_E = \frac{1}{c_s}, \tag{3.36}$$

which corresponds to the dashed line in Fig. 3.9. On the other hand, as the frequency approaches the bilayer cutoff frequency, Q_E becomes singular as the in-plane power flow vanishes.

At the Love transition frequency Q_E has a minimum. As the mode shapes in the two plates, at this frequency, are the same as those of the isolated plates (constant displacement for the FP and sinusoidal distribution for SP as shown in Fig. 3.4) the Q_E value can be calculated by using (3.7) and (3.13)

$$Q_E = \frac{1}{c_s} \frac{1}{\frac{c_s}{c_F} + 2\frac{c_F \rho_F d_F}{c_s \rho_s d_s}}. \tag{3.37}$$

Since the functions involved in the integrals (3.7) and (3.13) depend on the square of sinusoidal functions, these integrals do not depend on the order of the SP mode. As a result, (3.37) is independent of the mode considered. Moreover, it is usually lower than $1/c_s$ as the product $c_F \rho_F d_F$ involves the acoustic impedance ($c_F \rho_F$) of the fast plate which is much larger than that of the slow plate. Consequently, since in the limit as f goes to infinity, Q_E tends to $1/c_s$ with a negative slope, it follows that a Q_E maximum has to occur after the transition frequency (see Fig. 3.9). The steep positive slope of Q_E after the transition frequency marks the rapid energy migration from the FP towards the SP which is in agreement with Love wave theory.

According to Sec. 3.3, the guided wave attenuation can be derived from the Q factors of the equivalent elastic plate and the perturbation factor. In particular, since for low loss materials the complex shear modulus can be related to the bulk attenuation per wavelength, $\bar{\alpha}_s$, according to

$$\bar{\alpha}_s \simeq \pi \frac{Im\{\tilde{\mu}_s\}}{Re\{\tilde{\mu}_s\}}, \tag{3.38}$$

the guided wave attenuation can be expressed as

$$\zeta \simeq f\bar{\alpha}_s Q_E. \tag{3.39}$$
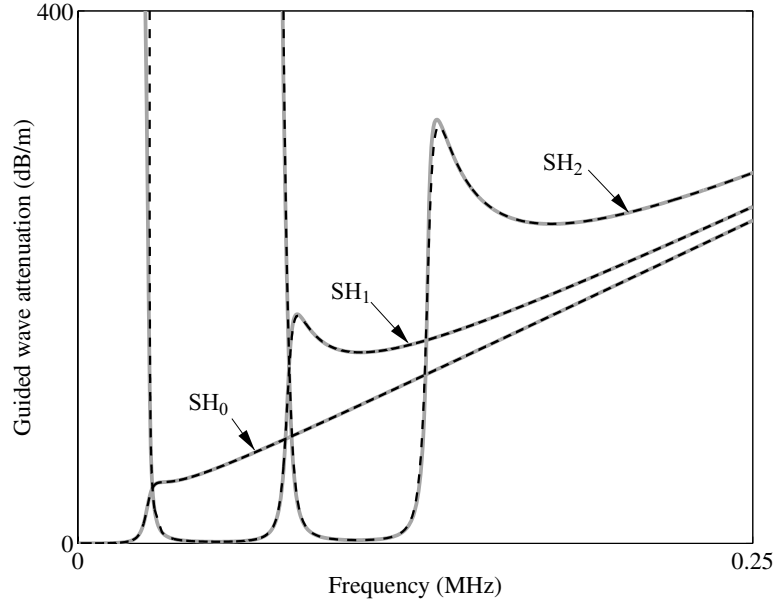
Figure 3.10: Guided wave attenuation versus frequency for the bilayer defined in Tab. 3.1, with $0.1 np/wl$ bulk attenuation in the SP: (———) numerical solution from Disperse; $(- - -)$ first order approximation.

Moreover, for many low loss materials, the bulk attenuation is approximately proportional to the frequency, so the bulk attenuation per wavelength is constant (since the real part of the shear modulus is almost non-dispersive). Figure 3.10 shows the guided wave attenuation calculated by the Disperse software which solves numerically the exact secular equation (solid grey line), and the first order approximation (dashed line) in the propagating domain for the first three modes of the bilayer. The excellent agreement between the two different calculations proves the validity of (3.16). Moreover, the strong frequency dependence of the guided wave attenuation is mainly due to the dispersion of the first energy factor of the elastic bilayer. Also, minima of the guided wave attenuation spectrum must occur around the Love transition frequencies since the energy factors have minima at those frequencies.

Figure 3.11 shows the comparison between the solution obtained from Disperse (solid grey line) and the zero order approximation obtained through the Π factor (dashed line). For each mode, the approximation is in agreement with the Disperse prediction for frequencies up to the cutoff frequency of the corresponding equivalent
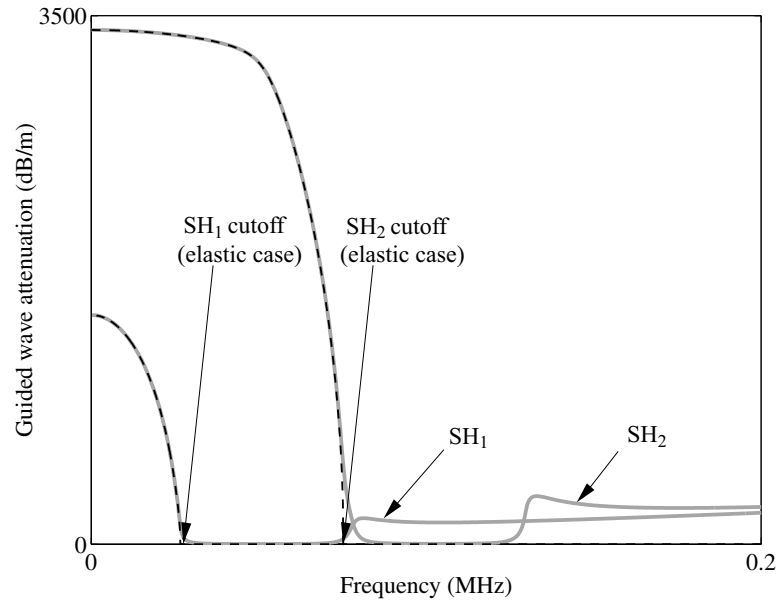
Figure 3.11: Guided wave attenuation versus frequency for the same bilayer as figure 3.10: (———) numerical solution from Disperse; $(- - -)$ zero order approximation.

elastic mode. Figure 3.11 also shows the numerical solution in the propagating region of the first two equivalent elastic modes, which correspond to the first two modes shown in Fig. 3.10. It can be noticed that, for each mode, below the cutoff frequency of the equivalent elastic mode the guided wave attenuation is extremely high while it rapidly drops as the frequency approaches the cutoff. As a consequence, for practical purposes, the modes can be regarded as nonpropagating below the cutoff frequencies of the equivalent elastic bilayer.
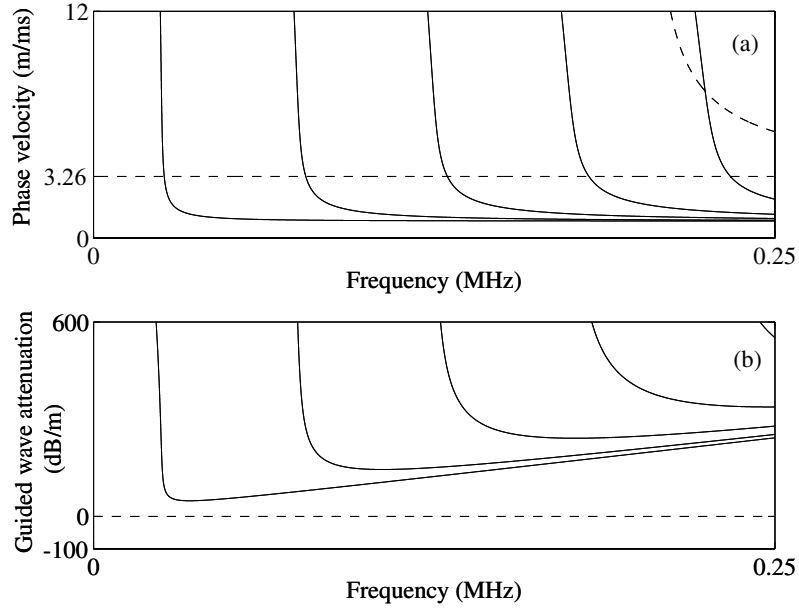
Figure 3.12: Asymptotic phase velocity (a) and guided wave attenuation (b) dispersion curves: $(---)$ first family; (———) second family.

3.6 Mode jumping

In Sec. 3.4 it has been shown that for the equivalent elastic bilayer, each mode originates from the coupling of different asymptotic modes which results in the mode jumping previously studied. In this section it will be shown that, if the material attenuation is considered, the bilayer mode paths do not necessarily jump.

This phenomenon becomes evident if an asymptotic solution for the attenuative bilayer is considered. In particular, by taking the limit as the stiffness and the density of the FP go to infinity at constant shear velocity, it can be shown that the dispersion curves tend to two families of modes which correspond to those discussed in Sec. 3.4. The first family coincides with the free FP modes, which propagate without being attenuated as all the energy flows in the elastic FP. The second family corresponds to the clamped-free modes of the SP, which are highly attenuated. Figure 3.12 shows the phase velocity and guided wave attenuation dispersion for the two families. The curves have been obtained by modelling the SP according to Tab. 3.1 and assuming constant bulk wave attenuation per wavelength ($\bar{\alpha} = 0.1 np/wl$).

As can be deduced from Fig. 3.12a, an infinite number of intersections occur between the phase velocities of the first and second families. However, no intersections occur in the guided wave attenuation versus frequency plane, as the guided wave attenuation of the first family is always zero (Fig. 3.12b). Since two modes intersect each other when both the phase velocity and guided wave attenuation are equal, it follows that the asymptotic modes do not intersect each other.

For large stiffness and density of the FP, the bilayer mode paths approach the asymptotic families since the asymptotic solution is the limit condition of the bilayer modes. Moreover, due to the absence of intersection between the asymptotic families, as the stiffness and density increase, a bilayer mode cannot tend to two different asymptotic modes simultaneously. As a result, the bilayer modes cannot jump from one asymptotic mode to another, provided the FP stiffness and density are large enough. On the other hand, the mode jumping studied in Sec. 3.4 for the elastic bilayer is due to the existence of the asymptotic mode intersections, which allow a bilayer mode to tend to two different asymptotic modes simultaneously.

From the previous discussion it follows that, for a particular value of the FP stiffness and density, a transition between jumping and non-jumping behaviour must occur. Moreover, the transition is characterised by the intersection of two different modes which occurs when, at the same frequency, the two modes have the same phase velocity and guided wave attenuation.

As an example, let us consider the bilayer studied in Sec. 3.5 when the density and the stiffness of the FP are increased by about a factor of four while all the other parameters are kept constant (the shear velocity of the FP is unchanged). According to Fig. 3.13, the bilayer SH_0 mode jumps from the free FP SH_0^{F} mode into the clamped-free SP $SH_0'^{\mathrm{S}}$ mode, while the SH_1 mode jumps from $SH_0'^{\mathrm{S}}$ into SH_0^{F} below the first transition frequency. Around the first cutoff frequency of the equivalent elastic bilayer, SH_0 and SH_1 cross in attenuation (Fig. 3.13b) while their phase velocities do not because of the mode jumping. However, if the FP stiffness and density were increased further mode jumping would not occur at this frequency.
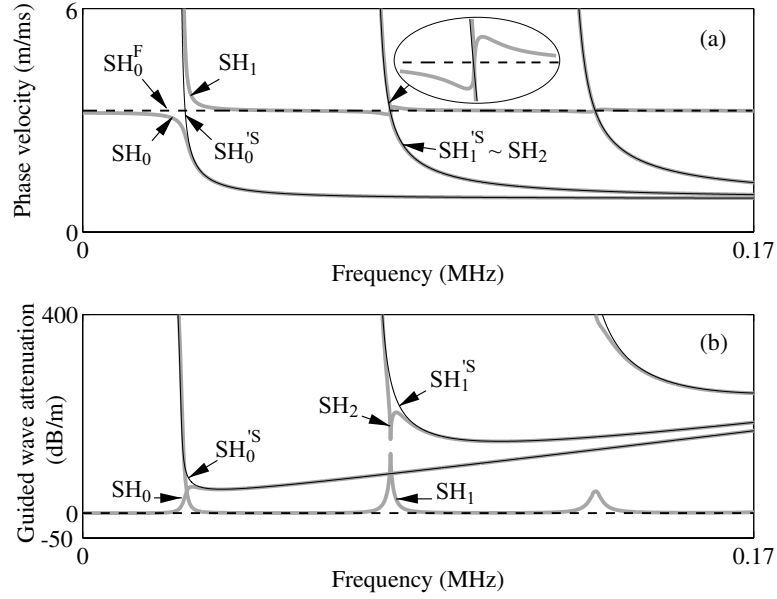
Figure 3.13: Phase velocity (a) and guided wave attenuation (b) versus frequency for Tab. 3.1 bilayer with $\rho_{\mathrm{F}} = 33000 Kg/m^3$ and $\bar{\alpha} = 0.1 np/wl$: (——) numerical solution from Disperse; ($---$) first family; (——) second family.

For frequencies higher than the first transition frequency, the SH_1 mode follows the path of the SH_0^{F} mode rather than jumping down to the SH'^{S}_1 mode (Fig. 3.13a) as happened at lower value of the stiffness and density for the elastic bilayer (Fig. 3.8). Instead, SH_1 and SH_2 modes cross in phase velocity but they do not in attenuation (Fig. 3.13b). Since an intersection between two modes occurs when at one frequency the couples (c_{ph}, ζ) are the same for both modes, it follows that for the case considered here, the modes never intersect each other.

A similar phenomenon has been observed in the case of Lamb waves propagating in elastic anisotropic plates loaded with an inviscid fluid [39]. Rohklin $et\ al.$ [40] showed for the isotropic case that while for low fluid density the mode paths essentially overlap those of free plate modes, increasing the fluid-solid density ratio (at constant bulk velocities) leads to an interaction and mutual exchange between portions of various mode branches. On the other hand, Dabirikhah $et\ al.$ [41] showed that as the fluid-solid density ratio decreases, the antisymmetric A_0 mode couples with the AS antisymmetrical interface Scholte wave. Moreover, mode "switch over"

between the two lowest-order longitudinal modes of a free rod occurs when it is loaded with a high density inviscid fluid [42].

The occurrence of the transition between jumping and non-jumping behaviour depends on all the bilayer parameters and on the frequency. Numerical calculations carried out for different geometries and material properties have shown that the transition occurs when the impedance-thickness product of the two layers, the shear velocity of the fast plate and the material attenuation of the slow plate satisfy the approximate relationship

$$c_{\mathrm{F}} \frac{c_{\mathrm{F}} \rho_{\mathrm{F}} d_{\mathrm{F}}}{c_{\mathrm{S}} \rho_{\mathrm{S}} d_{\mathrm{S}}} (2M-1)^2 \bar{\alpha}^2 = const., \tag{3.40}$$

where $M \epsilon \{0, 1, 2, ...\}$ is the order of the clamped-free SP mode where the transition occurs and accounts for the influence of frequency. The value of the constant is roughly $25 m/ms$. If the left hand side of (3.40) is larger than the constant, the modes do not jump, whereas if it is lower, the modes jump. Even though (3.40) is only an approximate relationship, it provides a complete description of the role of the bilayer parameters in the mode jumping phenomenon.

For non attenuative materials ($\bar{\alpha} = 0$), (3.40) implies that jumping always occurs as the left hand term is zero whatever the geometry and the acoustic properties are (this is in agreement with Sec. 3.4). Moreover, (3.40) shows that, for a given value of the material damping, the occurrence of the jumping depends on the ratio of the impedance-density product of the FP to that of the SP. This ratio provides a measure of the acoustic-geometric coupling of the two layers. As a consequence, the stiffer, heavier and thicker the FP compared to the SP the more unlikely is the mode jumping. This is a direct consequence of the fact that the energy tends to flow primarily in the fast plate.

With reference to the former example (Fig. 3.13), the SH_0 mode jumps since the value of the left hand term of (3.40) is $2.8 m/ms$ which is below the transition limit. On the other hand, the SH_1 mode does not jump because the value of the left hand term of (3.40) is 25.2 ($M = 1$) which is slightly higher than the transition

limit ($25m/ms$). This proximity to the limit is the reason why SH_1 and SH_2 almost touch each other in the guided wave attenuation-frequency plane as shown in Fig. 3.13b (i.e. this condition is close to the mode intersection which characterises the transition).

The factor M accounts for the role of the frequency in the transition mechanism. In order to show this it has to be noticed that the two partial waves which generate the SP vibration (see Fig. 3.1) have an important physical interpretation: the partial wave which leaves the interface, SH^+, accounts for the energy transmitted from the FP to the SP, while that which enters the interface, SH^-, represents the portion of transmitted energy which returns to the FP. In the elastic case the two partial waves have the same amplitude by energy conservation. As M increases (i.e. the frequency increases) the material damping increases as well. As a consequence, the SH^- amplitude decays, while the SH^+ amplitude remains almost unchanged. In other words, SH^+ becomes dominant with respect to SH^-. For very low SH^- amplitude the bilayer behaves as if the FP was loaded with a viscoelastic half space, as the solution for this case is obtained by considering only one partial wave in the half space. Since for this type of geometry no mode jumping occurs, it follows that modes can jump only for low values of M. This argument will be explored in more detail in the next section.

The relationship (3.40) leads to a more rigorous definition of the low material attenuation regime. The low regime corresponds to those values of the bulk attenuation which allow the modes to jump, for given geometry and elastic properties of the bilayer. Under this hypothesis, the zero and first order approximations can be applied. Moreover, even though these approximations can only strictly describe jumping modes, they still provide accurate results when modes do not jump. Figure 3.14 shows the comparison between the dispersion curves of the case studied in Fig. 3.13 and the first order approximation prediction obtained by considering the first three modes of the elastic bilayer only. With the exception of the frequencies where the mode jumping is expected, the first order solution is generally quite accurate over all the frequency spectrum. Note that the first order approximation covers up to
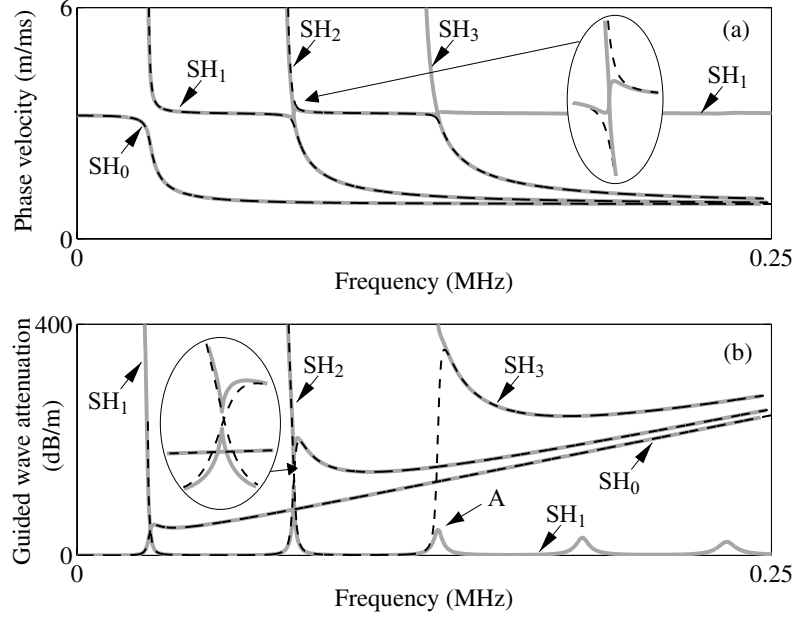
Figure 3.14: Phase velocity (a) and guided wave attenuation (b) versus frequency for the bilayer described in Tab. 3.1 with $\rho_F = 33000 Kg/m^3$ and $\bar{\alpha} = 0.1 np/wl$: (———) numerical solution from Disperse, $(---)$ first order approximation for the first three modes only

the peak A of SH_0 (Fig. 3.14b) since it has been calculated by considering just the first three modes of the elastic bilayer.

As has been shown in the previous section, the minima of Q_E for the elastic bilayer occur at the Love transition frequencies which are roughly located at the centre of the plateau regions of the phase velocity dispersion curves. The accuracy of the first order approximation in these regions suggests that the minima of Q_E of the viscoelastic bilayer have to occur at the Love transition frequencies indeed. As a consequence, by virtue of (3.14) it follows that the guided wave attenuation minima have to occur around the Love transition frequencies also.
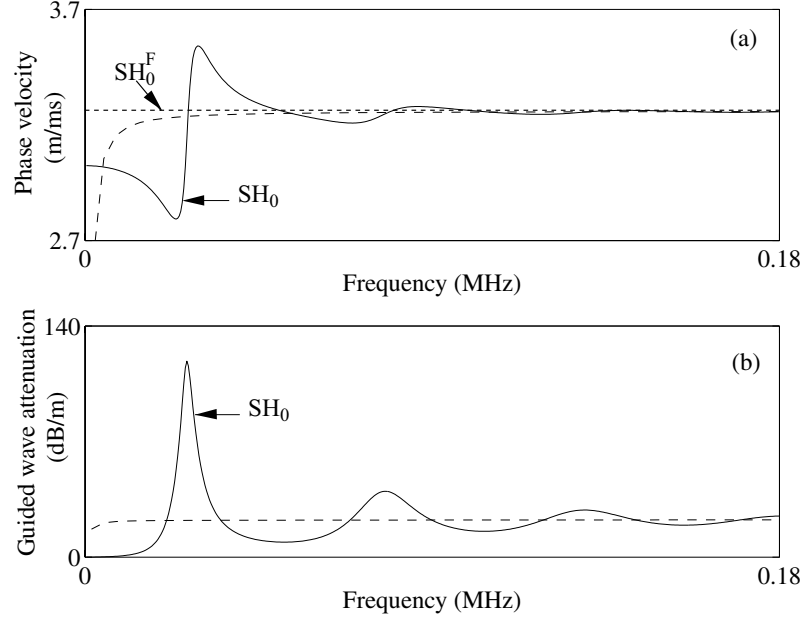
Figure 3.15: Phase velocity (a) and guided wave attenuation (b) dispersion curves; (———) Tab. 3.1 bilayer with $\bar{\alpha} = 0.8np/wl$; ($\cdots$) free FP; ($---$) FP bonded to a viscoelastic half space.

3.7 High material attenuation regime

In the case of highly attenuative materials the attenuation levels are large and mode jumping cannot occur. Moreover, the zero and first order approximations become less accurate, due to the large imaginary part of the shear stiffness. On the other hand, the perturbation factor Q_p (eq. 3.24) becomes significant since the shear modulus of the viscoelastic material is more dispersive. However, in order to study the effects of the interaction between the wavelength and the geometry on the guided wave dispersion the perturbation factor will be neglected in this study. Moreover, the modes which tend to the second asymptotic family are not considered as they are highly attenuated and therefore of no interest for practical applications (Sec. 3.6). Here, only the bilayer SH_0 mode, whose path tends to that of the SH_0^F mode, is studied since the results obtained in this case can be extended to the higher order modes of the first family. Figure 3.15a shows the SH_0 phase velocity as a function of frequency (solid line). As the frequency increases, the phase velocity oscillates around that of SH_0^F. On the other hand, the guided wave attenuation exhibits periodic peaks which occur at the frequencies where the mode would jump if the bilayer
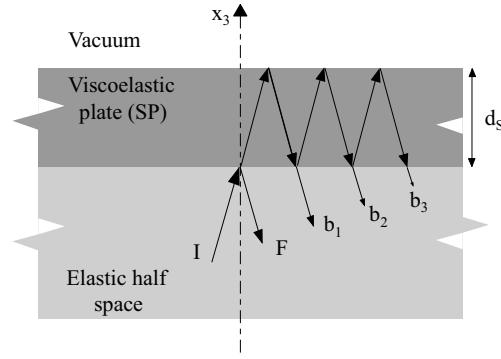
Figure 3.16: Diagram of the reflection at the interface half space-layer showing the echo wave paths.

was elastic (Fig. 3.15b). In order to understand the physical reason for these peaks, it is useful to consider the case in which the elastic plate is bonded to a viscoelastic half space with the same mechanical and acoustic properties as the bilayer SP. For the bilayer, at each frequency, one would expect lower guided wave attenuation than the half space case, as part of the energy transmitted from the FP into the SP is reflected back from the SP free boundary (while in the half space case all the transmitted energy is lost). However, at the peak attenuation frequencies, the bilayer guided wave attenuation is higher than that of the loaded plate (dashed line) as shown in Fig. 3.15b. This suggests that, at these frequencies, the mechanism which causes the guided wave attenuation is strongly affected by the geometry of the wave guide. In particular, with reference to (3.14), it follows that the bilayer has higher energy factor than the loaded plate. However, this does not explain why this phenomenon only occurs at certain frequencies rather than being continuous over the whole frequency range.

The explanation can be found by studying the reflection of an SH bulk wave at the interface between a fast half space and the slow layer. In this case, the reflected wave can be regarded as the superposition of a front reflection, which would occur if the slow layer was infinitely thick, and a series of back reflections from the SP free surface as shown in Fig. 3.16.

If the incident wave, I, is perpendicular to the interface and of unit amplitude and zero phase, the front reflection, F, is given by

$$F = \frac{Z_\mathrm{S} - Z_\mathrm{F}}{Z_\mathrm{S} + Z_\mathrm{F}} = |F|e^{i\Phi_\mathrm{F}}, \tag{3.41}$$

where $Z_\mathrm{S,F}$ are the complex impedances for the two materials defined as

$$Z_\mathrm{S,F} = a_\mathrm{S,F}\rho_\mathrm{S,F}. \tag{3.42}$$

On the other hand, the back reflection, B, is [43]

$$B = \sum_{n=1}^{\infty} b_n = \frac{F^2 - 1}{1 + Fe^{2iq_\mathrm{S}d_\mathrm{S}}}e^{2iq_\mathrm{S}d_\mathrm{S}} = |B|e^{i\Phi_\mathrm{B}}, \tag{3.43}$$

where

$$q = \frac{\omega}{c_\mathrm{S}} + 2\pi i\frac{\omega}{c_\mathrm{S}}\bar{\alpha}_\mathrm{S}. \tag{3.44}$$

As a consequence the total reflection is

$$R = |F|e^{i\Phi_\mathrm{F}} + |B|e^{i\Phi_\mathrm{B}}. \tag{3.45}$$

Since the incident signal has unit amplitude, R can be regarded as a reflection coefficient. In the case of an elastic SP, the total reflection is equal in magnitude to the incident signal, by energy conservation. Moreover, since a unit amplitude incident signal is considered, the total reflected signal has to be of unit amplitude, while the phase can assume any value between zero and π. Figure 3.17 shows the phase shift between the front and the back reflections and the two reflection moduli versus the ratio of layer thickness to wavelength in the layer (the material properties are those of table 3.1).

At the through thickness resonances of the free SP ($d_\mathrm{S}/\Lambda = 0, 0.5, 1, ...$), the two reflections are in phase and constructive interference occurs. On the other hand, at the through thickness resonances of the clamped-free SP ($d_\mathrm{S}/\Lambda = 0.25, 0.75, ...$), the interference is destructive as the two reflections are opposite in phase.

When material damping is considered, the total reflection cannot be studied as a function of d_S/Λ unless the frequency dependence of the SP acoustic properties is known. However, since the purpose here is to explain the reason for the maxima in
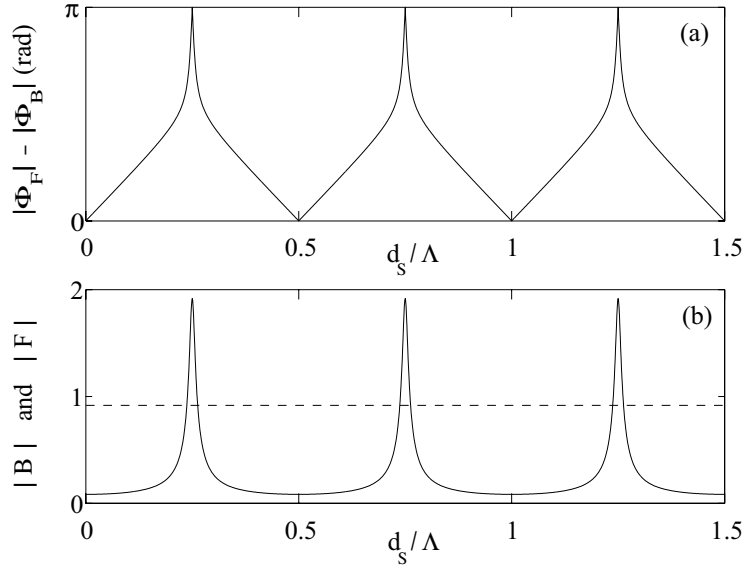
Figure 3.17: Reflection coefficients moduli and phases against the ratio SP thickness to wavelength for the elastic case: (a) phase shift between front and back reflection; (b) (——) back reflection modulus, (− − −) front reflection modulus.

attenuation in the case shown in Fig. 3.15, constant bulk shear velocity and bulk attenuation per wavelength will be assumed.

The total reflection coefficient amplitude has to be lower than unity as energy dissipation within the SP occurs. Figure 3.18a shows the reflection coefficient amplitude when the same acoustic and mechanical properties as the case studied in Fig. 3.15 are considered. According to Fig. 3.18a the total reflection coefficient modulus has maxima close to the free SP resonance frequencies, whereas it has minima around the clamped-free resonance frequencies. Moreover, as the frequency increases, the reflection coefficient tends to the front reflection F (dashed line). These oscillations are due to the interference phenomena as shown in Fig. 3.18b which is similar to Fig. 3.17a. Minima and maxima in the reflection occur where the interference is destructive ($\Delta\Phi = \pi$) and constructive ($\Delta\Phi = 0$), respectively. It is interesting to note that the back reflection peaks and minima decay with the frequency as the amount of the energy dissipated in the SP increases with the frequency, Fig. 3.18c. At high frequencies, the back reflection almost vanishes, and the total reflection coefficient tends to that of the front reflection.
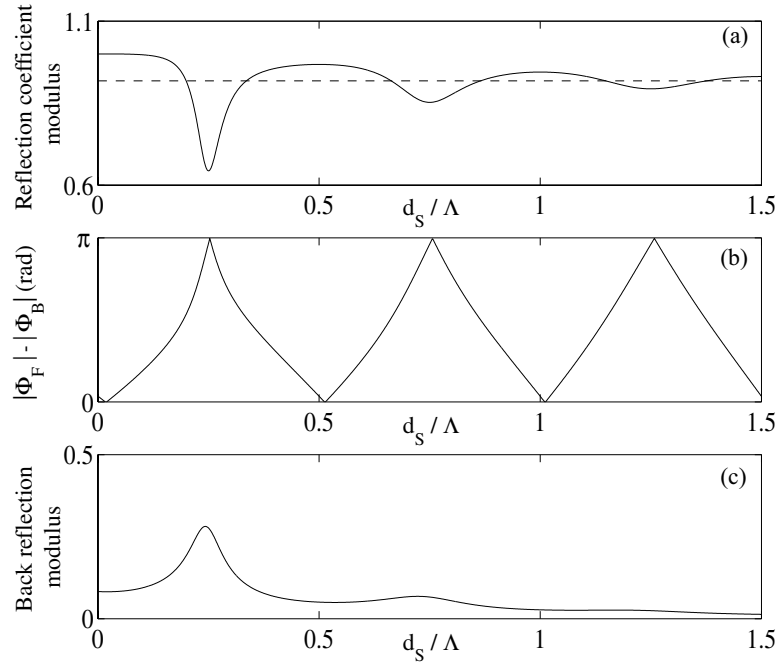
Figure 3.18: Reflection coefficient modulus and phase against the ratio SP thickness to wavelength for the viscoelastic case: (a) (———) total reflection modulus, $(---)$ front reflection modulus; (b) phase shift between front and back reflection; (c) back reflection modulus.

As the total reflection coefficient amplitude accounts for the energy lost in the viscoelastic layer, the comparison of Fig. 3.18a with Fig. 3.15b suggests that guided wave attenuation peaks are due to destructive interference phenomena, which occur at the interface between the two layers. Moreover, as the bulk attenuation increases, the guided wave attenuation tends to that of the plate loaded with viscoelastic half space, since the back reflection tends to zero.

Even though these results have been obtained by considering a simple model for the frequency dependence of the SP material properties (constant shear velocity and bulk attenuation per wavelength), they can be generalized to the case of more complex frequency dependence. In particular, the main effect of shear velocity dispersion is to shift the frequencies of the guided wave attenuation peaks, since the clamped-free SP through thickness resonance frequencies change. In other words,

the guided wave attenuation plot is stretched and contracted along the frequency axis.

3.8 Summary

A theoretical investigation of shear horizontal waves propagation in elastic plates coated with viscoelastic materials has been presented. It has been shown that the bilayer modes originate from the interaction between the free elastic plate modes and the clamped-free viscoelastic layer modes. Moreover, the guided wave attenuation has been related to the strain energy and to the time derivative of the mechanical energy of the viscoelastic layer. This has led to the definition of two energy factors that, for low loss materials, can be assumed to equal those of the equivalent elastic bilayer. As a result, the guided wave attenuation of the attenuative bilayer has been derived from the acoustic response of the equivalent elastic bilayer. Moreover, for low loss materials, a mode jumping (which is equivalent to mode repulsion) phenomenon occurs. It has been shown that the jumping is due to the nature of the asymptotic solution of the equivalent elastic bilayer (existence of intersection points between the two different families of asymptotic modes). For highly attenuative materials, it has been shown that the mode jumping does not occur and an approximate formula has been provided in order to characterise the transition between jumping and non-jumping behaviour as a function of all the acoustic and geometric parameters of the bilayer.

For highly attenuative materials the bilayer modes can be divided into two families: modes whose paths are close to those of the free elastic plate modes, and modes which follow the trajectories of the clamped-free viscoelastic layer modes. The second family of modes is characterised by higher guided wave attenuation than those of the first family. For the first family modes, the guided wave attenuation as a function of frequency exhibits periodic peaks which occur around the through thickness resonance frequencies of the clamped-free viscoelastic layer when it is considered to be elastic. On the other hand, minima of the guided wave attenuation occur at the

Love transition frequency.

Under the hypothesis of large pipe diameter to wall thickness ratio, the SH modes studied in this chapter are equivalent to torsional modes propagating in coated pipelines. Moreover, since bitumen coatings are highly attenuative (see Chapters 7 and 8), the torsional modes tend to either the first or second families as discussed above. However, the modes of the second family have little practical interest due to their large guided wave attenuation which would lead to a very short propagation distance. On the other hand, SH_0 is the most attractive mode for long range inspections as, at the Love transition frequencies, it provides the lowest values of the guided wave attenuation.

Another class of mode which could be employed for the inspection of coated pipelines is represented by longitudinal modes which, according to our assumption on the pipe geometry, correspond to Lamb waves propagating in bilayered plates. Since these modes could have lower guided wave attenuation than SH_0, their dispersion curves will be analysed in the next Chapter.

Chapter 4

Lamb wave propagation in bilayers

4.1 Background

In order to assess the feasibility of longitudinal guided wave inspection of coated pipelines, this Chapter addresses the effects of attenuative coatings on the dispersion characteristics of Lamb waves propagating in elastic plates. Lamb waves originate from the superposition of shear and longitudinal bulk waves, consequently the propagation of these waves depends on both the shear and longitudinal acoustic properties of the material.

After deriving the dispersion equation in Sec. 4.2 the topology of phase velocity and guided wave attenuation spectra is analysed as a function of the coating internal damping (longitudinal and shear bulk attenuations). By analogy with the previous Chapter the possibility of an energy based correspondence between the dispersion of the attenuative bilayer and that of a related elastic bilayer is explored in Sec. 4.3 so as to investigate separately the effects of the longitudinal and shear bulk attenuations on the attenuation of the guided modes. The dispersion characteristics of a perfectly elastic bilayer are considered in Sections 4.4 and 4.5 and the spectra of the bilayer with low and large material absorption are examined in Sections 4.6 and 4.7, respectively.
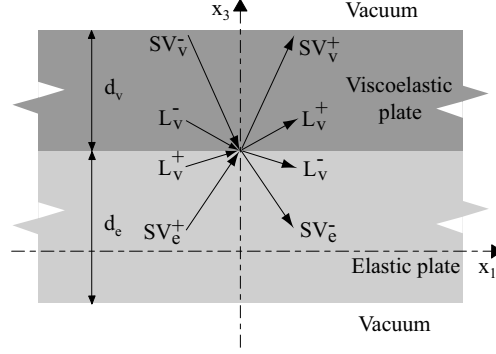
Figure 4.1: Partial waves diagram.

4.2 Secular equations for a bilayer

Let us consider the same bilayer as in the previous Chapter whose longitudinal properties are listed in Tab. 4.1. The propagation of Lamb waves originates from the superposition of one pair of longitudinal bulk waves (2.21), $L^\pm$, and one pair of shear bulk waves (2.28), $SV^\pm$, per layer (Fig. 4.1), the bulk waves being polarized parallel to the plane $x_2 = 0$. The boundary conditions, which are the same as in the case of SH waves, lead to the following secular equation

$$det \begin{bmatrix} T_{3,1_{top}}^{SV_v^+} & T_{3,1_{top}}^{SV_v^-} & T_{3,1_{top}}^{L_v^+} & T_{3,1_{top}}^{L_v^-} & 0 & 0 & 0 & 0 \\ T_{3,3_{top}}^{SV_v^+} & T_{3,3_{top}}^{SV_v^-} & T_{3,3_{top}}^{L_v^+} & T_{3,3_{top}}^{L_v^-} & 0 & 0 & 0 & 0 \\ u_{1_{int}}^{SV_v^+} & u_{1_{int}}^{SV_v^-} & u_{1_{int}}^{L_v^+} & u_{1_{int}}^{L_v^-} & -u_{1_{int}}^{SV_e^+} & -u_{1_{int}}^{SV_e^-} & -u_{1_{int}}^{L_e^+} & -u_{1_{int}}^{L_e^-} \\ u_{3_{int}}^{SV_v^+} & u_{3_{int}}^{SV_v^-} & u_{3_{int}}^{L_v^+} & u_{3_{int}}^{L_v^-} & -u_{3_{int}}^{SV_e^+} & -u_{3_{int}}^{SV_e^-} & -u_{3_{int}}^{L_e^+} & -u_{3_{int}}^{L_e^-} \\ \frac{\rho_v}{\rho_e}T_{3,1_{int}}^{SV_v^+} & \frac{\rho_v}{\rho_e}T_{3,1_{int}}^{SV_v^-} & \frac{\rho_v}{\rho_e}T_{3,1_{int}}^{L_v^+} & \frac{\rho_v}{\rho_e}T_{3,1_{int}}^{L_v^-} & -T_{3,1_{int}}^{SV_e^+} & -T_{3,1_{int}}^{SV_e^-} & -T_{3,1_{int}}^{L_e^+} & -T_{3,1_{int}}^{L_e^-} \\ \frac{\rho_v}{\rho_e}T_{3,3_{int}}^{SV_v^+} & \frac{\rho_v}{\rho_e}T_{3,3_{int}}^{SV_v^-} & \frac{\rho_v}{\rho_e}T_{3,3_{int}}^{L_v^+} & \frac{\rho_v}{\rho_e}T_{3,3_{int}}^{L_v^-} & -T_{3,3_{int}}^{SV_e^+} & -T_{3,3_{int}}^{SV_e^-} & -T_{3,3_{int}}^{L_e^+} & -T_{3,3_{int}}^{L_e^-} \\ 0 & 0 & 0 & 0 & T_{3,1_{bot}}^{SV_e^+} & T_{3,1_{bot}}^{SV_e^-} & T_{3,1_{bot}}^{L_e^+} & T_{3,1_{bot}}^{L_e^-} \\ 0 & 0 & 0 & 0 & T_{3,3_{bot}}^{SV_e^+} & T_{3,3_{bot}}^{SV_e^-} & T_{3,3_{bot}}^{L_e^+} & T_{3,3_{bot}}^{L_e^-} \end{bmatrix} = 0,$$

(4.1)

where the first two rows refer to the traction free condition on the top of the bilayer, the third and fourth rows account for the continuity of the displacement at the bilayer interface, the fifth and sixth come from the stress continuity at the interface and the last two provide the traction free condition at the bottom of the bilayer. In

this case, the resulting displacement field can be expressed as

$$u_1(x_1, x_3, \omega) = h_1(x_3)e^{-\zeta x_1}e^{-i\frac{\omega}{c_{ph}}x_1}, \tag{4.2}$$

$$u_2(x_1, x_3, \omega) = 0, \tag{4.3}$$

$$u_3(x_1, x_3, \omega) = h_3(x_3)e^{-\zeta x_1}e^{-i\frac{\omega}{c_{ph}}x_1}. \tag{4.4}$$

4.3   Lamb wave attenuation

As in the previous Chapter, the purpose of this section is to provide a relationship between the guided wave attenuation, the strain energy in the viscoelastic layer and the longitudinal and shear acoustic properties of the bilayer. For the case of SH waves, it has already been shown that by considering a volume, V, of unit width in the $\hat{x}_2$ direction, and with height equal to the thickness of the bilayer (see Fig. 3.2), the guided wave attenuation, ζ, can be related to the average dissipated power, P_d, in the volume and the average in-plane power flow per unit width, $< P >$, according to (3.9). The same relationship holds in the case of Lamb waves and can be proved by means of the complex acoustic Poynting's vector theorem [28]. The net flux into the rectangular parallelepiped shown in Fig. 3.2 is given by the summation of the flows through the faces of the parallelepiped. However, the flux through each lateral surface perpendicular to $\hat{x}_3$, S_l, is zero due to the traction free condition. Also the flow across the faces perpendicular to $\hat{x}_2$, S_f, vanishes as the only non zero stress is σ_{22} which is perpendicular to the displacement field. By substituting (4.2) and (4.4) into (2.38) the flux through a transversal surface perpendicular to $\hat{x}_1$, S_t, at the position x_1 can be written as

$$\begin{aligned}P_{x_1} &= \frac{1}{2}\omega e^{-2\zeta x_1}\int_{d_e+d_v}\left(\xi\left((\tilde{\lambda}+2\tilde{\mu})|h_1|^2+\tilde{\mu}|h_3|^2\right)\right.\\&\quad + \left. i(\tilde{\lambda}h_3'h_1^*+\tilde{\mu}h_1'h_3^*)\right)dx_3.\end{aligned} \tag{4.5}$$

As a consequence, the total net flow into the parallelepiped is the difference between the fluxes calculated at the two transversal surfaces. Moreover, by considering the real part of (3.6), the power balance can be written as

$$\Delta Re\{P_{x_1}\} + P_d = 0. \tag{4.6}$$

Table 4.1: Elastic parameters used for studying Lamb wave propagation; the values of the material absorption are specified in the text.

	c_{S} (m/ms)	c_{L} (m/ms)	ρ (kg/m^3)	Thickness (mm)
Elastic plate	900	1700	1250	9.00
Metallic plate	3260	5960	7930	8.00

By substituting (4.5) into (4.6) and differentiating with respect to x_1, and by considering that the real part of P_{x_1} is the average in-plane power flow, $< P >$, one obtains

$$\zeta = \frac{\frac{dP_d}{dx_1}}{2 < P >}. \tag{4.7}$$

Note that the eqs (4.6) and (4.7) are the same as in the case of SH waves. Furthermore, eq. (4.6) implies that all the modes are propagating (see Sec. 3.3).

In order to relate the guided wave attenuation to the strain energy let us now consider the peak strain energy and the dissipated power per unit volume which, after some manipulations, can be expressed as

$$e_s = \frac{1}{2}(\tilde{\lambda}_r^v + 2\tilde{\mu}_r^v)\varepsilon_0\varepsilon_0^* + 2\tilde{\mu}_r^v(\varepsilon_{13}\varepsilon_{13}^* - \varepsilon_{11}\varepsilon_{33}^*), \tag{4.8}$$

$$p_d = \frac{1}{2}\omega(\tilde{\lambda}_{im}^v + 2\tilde{\mu}_{im}^v)\varepsilon_0\varepsilon_0^* + 2\omega\tilde{\mu}_{im}^v(\varepsilon_{13}\varepsilon_{13}^* - \varepsilon_{11}\varepsilon_{33}^*), \tag{4.9}$$

which leads to

$$p_d = \omega\left(\frac{\tilde{\lambda}_{im}^v + 2\tilde{\mu}_{im}^v}{\tilde{\lambda}_r^v + 2\tilde{\mu}_r^v}\delta + \frac{\tilde{\mu}_{im}^v}{\tilde{\mu}_r^v}\gamma\right), \tag{4.10}$$

where

$$\delta = \frac{1}{2}(\tilde{\lambda}_r^v + 2\tilde{\mu}_r^v)\varepsilon_0\varepsilon_0^*, \tag{4.11}$$

$$\gamma = 2\tilde{\mu}_r^v(\varepsilon_{13}\varepsilon_{13}^* - \varepsilon_{11}\varepsilon_{33}^*), \tag{4.12}$$

ε_0 being the first invariant of the strain tensor. It is interesting to note that δ only depends on the displacement field resulting from the superposition of the two longitudinal bulk waves propagating in the viscoelastic layer. In order to show this, it is sufficient to consider that the strain tensor due to the superposition of two pairs of longitudinal and shear bulk waves is equivalent to the sum of the strain tensors of

each bulk wave taken separately. Since for a bulk shear wave the first strain invariant vanishes, it follows that ε_0 is the sum of the invariants of the two longitudinal bulk waves only. On the other hand, γ depends on both longitudinal and shear bulk waves due to the presence of extensional and distortional strains in eq. (4.12).

As in the case of SH waves, the derivative of the dissipated power can be expressed as

$$
\begin{aligned}
\frac{dP_d}{dx_1} = \int_{d_v} p_d dx_3 &= \omega \left(\frac{\tilde{\lambda}_{im}^v + 2\tilde{\mu}_{im}^v}{\tilde{\lambda}_r^v + 2\tilde{\mu}_r^v} \int_{d_v} \delta dx_3 + \frac{\tilde{\mu}_{im}^v}{\tilde{\mu}_r^v} \int_{d_v} \gamma dx_3 \right) \\
&= \omega \left(\frac{\tilde{\lambda}_{im}^v + 2\tilde{\mu}_{im}^v}{\tilde{\lambda}_r^v + 2\tilde{\mu}_r^v} \frac{d\Delta}{dx_1} + \frac{\tilde{\mu}_{im}^v}{\tilde{\mu}_r^v} \frac{d\Gamma}{dx_1} \right),
\end{aligned}
\tag{4.13}
$$

where Δ and Γ are the integrals of δ and γ over the portion of the viscoelastic layer contained in V. By substituting (4.13) into (4.7) the guided wave attenuation is given by

$$
\zeta = \frac{1}{2}\omega \left(\frac{\tilde{\lambda}_{im}^v + 2\tilde{\mu}_{im}^v}{\tilde{\lambda}_r^v + 2\tilde{\mu}_r^v} Q_\Delta + \frac{\tilde{\mu}_{im}^v}{\tilde{\mu}_r^v} Q_\Gamma \right),
\tag{4.14}
$$

where the two energy factors Q_Δ and Q_Γ are defined as

$$
Q_\Delta = \frac{\frac{d\Delta}{dx_1}}{<P>},
\tag{4.15}
$$

$$
Q_\Gamma = \frac{\frac{d\Gamma}{dx_1}}{<P>}.
\tag{4.16}
$$

Eq. (4.14) shows that the guided wave attenuation can be expressed as a linear combination of the energy factors, each energy factor being related to the strain energy contained in the viscoelastic layer when unit power flows through the cross section of the bilayer. Moreover, eq (4.14) allows the guided wave attenuation dispersion to be derived from the dispersion of a suitable equivalent elastic bilayer as has already be done for the SH wave case. In order to show this, the Maclaurin expansion of the function $\zeta(\tilde{\lambda}_{im}^v + 2\tilde{\mu}_{im}^v, \tilde{\mu}_{im}^v)$ is considered. In particular, by taking the expansions up to the first order results in

$$
\zeta \simeq \frac{1}{2}\omega \left(\frac{\tilde{\lambda}_{im}^v + 2\tilde{\mu}_{im}^v}{\tilde{\lambda}_r^v + 2\tilde{\mu}_r^v} Q_\Delta \mid_{\tilde{\lambda}_{im}^v + 2\tilde{\mu}_{im}^v = 0} + \frac{\tilde{\mu}_{im}^v}{\tilde{\mu}_r^v} Q_\Gamma \mid_{\tilde{\mu}_{im}^v = 0} \right),
\tag{4.17}
$$

which by considering that for low material damping the bulk attenuations in nepers per meter take the form [28]

$$\bar{\alpha}_{\mathrm{S}} \quad \simeq \quad \pi \frac{\tilde{\mu}_{im}}{\tilde{\mu}_r}, \tag{4.18}$$

$$\bar{\alpha}_{\mathrm{L}} \quad \simeq \quad \pi \frac{\tilde{\lambda}_{im} + 2\tilde{\mu}_{im}}{\tilde{\lambda}_r + 2\tilde{\mu}_r}, \tag{4.19}$$

allows the guided wave attenuation to be written as

$$\zeta \simeq f\bar{\alpha}_{\mathrm{L}}^v Q_\Delta \mid_{\tilde{\lambda}_{im}^v + 2\tilde{\mu}_{im}^v = 0} + f\bar{\alpha}_{\mathrm{S}}^v Q_\Gamma \mid_{\tilde{\mu}_{im}^v = 0} . \tag{4.20}$$

This equation clearly illustrates how splitting the energy into two parts, δ and γ, allows the guided wave attenuation to be thought of as a superposition of the effects of the two material bulk attenuations (longitudinal and shear) taken separately. In particular, the δ energy which depends on the energy carried by the longitudinal partial waves only (it would be zero if there were no longitudinal partial waves) provides, through the energy factor Q_Δ, the part of guided wave attenuation due the longitudinal bulk attenuation. On the other hand, the γ energy gives, through the energy factor Q_Γ, the part of guided wave attenuation due to the bulk shear attenuation.

In equation (4.20), the energy factors are calculated by considering the modes of an artificial bilayer in which the viscoelastic layer has been replaced with an ideal layer whose Lamé moduli are purely real and equal to the real parts of the viscoelastic layer moduli (i.e. $\mu_{art} = Re\{\tilde{\mu}(\omega)\}$ and $\lambda_{art} = Re\{\tilde{\lambda}(\omega)\}$). This assumption leads to the introduction of the equivalent elastic bilayer concept already discussed in Sec. 3.3.

As in the case of SH waves, below the cutoff frequency of a mode of the equivalent elastic bilayer the energy factors are singular since the in-plane power flow vanishes. The same argument considered for SH waves applies to the case of Lamb waves and leads to the definition of the energy factor Π according to eq. (3.20). It follows that, under the zero order approximation, the guided wave attenuation in the attenuative system corresponds to the projection along the bilayer interface of the wavenumber of the nonpropagating mode of the corresponding elastic system.
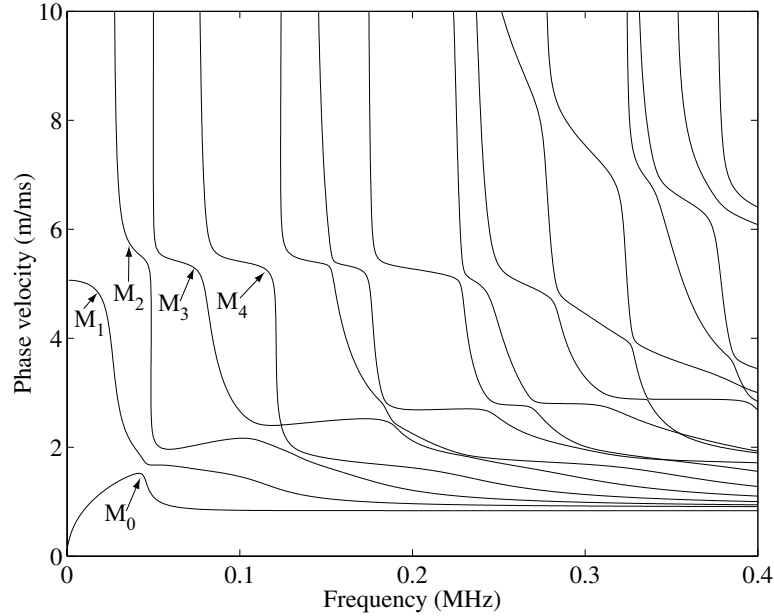
Figure 4.2: Lamb wave phase velocity dispersion curves for the elastic bilayer described in Tab. 4.1.

4.4 Elastic bilayer

As has been shown in the previous section, the guided wave attenuation dispersion can be derived from the energy factors of the equivalent elastic bilayer. For this reason this section is devoted to the study of the dispersion of elastic bilayers. Figure 4.2 shows the Lamb wave dispersion curves obtained by solving eq. (4.1) when the material damping is neglected, the bilayer acoustic properties and the geometry being summarized in Tab. 4.1. It can be seen that these curves are considerably different from those of a metallic plate loaded with an inviscid fluid layer. In the latter case, due to the absence of the shear stiffness in the liquid layer, the dispersion curves are only slightly different from those of the free metallic plate [23].

The Lamb waves of the bilayer originate from the interaction between the modes of the free metallic plate and those of the equivalent viscoelastic layer if it were rigidly clamped at the bilayer interface. In a similar fashion to Sec. 3.4, it can be observed that the matrix in (4.1) can be partitioned into four square matrices, leading to the
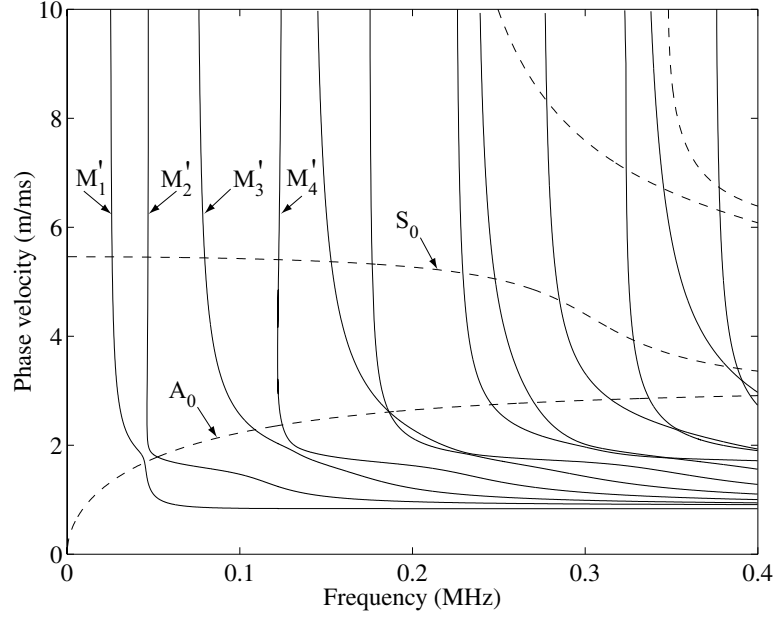
Figure 4.3: Asymptotic solutions to eq. (4.1): $(- - -)$ free metallic plate; (———) clamped-free equivalent viscoelastic layer.

characteristic equation

$$det \begin{bmatrix} \mathbf{C}_{11} & \mathbf{C}_{12} \\ \mathbf{C}_{21} & \mathbf{C}_{22} \end{bmatrix} = 0, \tag{4.21}$$

where the matrices $\mathbf{C}_{ij}$ have now dimension 4×4. By considering the limit as the stiffness and the density of the metallic plate go to infinity while keeping the complex bulk shear and longitudinal velocities constant the characteristic equation becomes

$$det \begin{bmatrix} \mathbf{C}_{11} & \mathbf{C}_{12} \\ \mathbf{0} & \mathbf{C}_{22} \end{bmatrix} = det(\mathbf{C}_{11})det(\mathbf{C}_{22}) = 0. \tag{4.22}$$

As a consequence, the asymptotic solution can again be divided into two families of modes. The first family is represented by the free metallic plate modes while the second one corresponds to the modes of the clamped-free equivalent viscoelastic layer. Figure 4.3 shows the two asymptotic families for the bilayer described in Tab. 4.1. For a finite value of the density and stiffness of the metallic plate, the bilayer mode trajectories jump from one asymptotic mode to another, as shown in Fig. 4.4. For instance, let us consider the path of the bilayer mode M_3. Its cutoff frequency occurs close to that of the M_2' mode of the equivalent clamped-free viscoelastic layer. As the
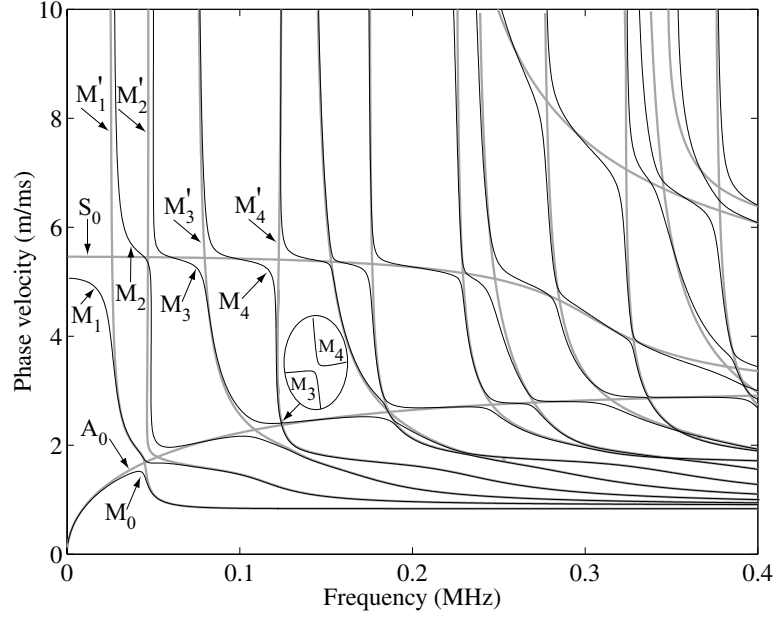
Figure 4.4: Phase velocity dispersion curves: (⸻) asymptotic solution; (⸻) bi-layer modes.

frequency increases, M_3 jumps to the S_0 mode of the free elastic plate. After intersecting S_0, M_3 veers towards the M_3' mode, and as the frequency increases further, M_3 intersects first M_3' and then A_0. M_3 does not intersect the bilayer mode M_4 (see inset), but veers and tends asymptotically to the M_4' mode. As has been shown for SH waves (Chapter 3) , the bilayer modes do not intersect each other. However, the presence of intersections between the two families of asymptotic solutions leads to the mode repulsion phenomenon (see for instance M_3 and M_4), which is particularly evident when the elastic plate is much stiffer and heavier than the viscoelastic layer.

Generally speaking, the bilayer cutoff frequencies tend to those of the clamped-free equivalent viscoelastic layer which correspond, for Lamb modes, to shear or longitudinal through-thickness standing waves and are given by

$$f_{\text{s}} = \frac{c_{\text{S}}^v}{4d_v}(2N - 1), \tag{4.23}$$

$$f_{\text{L}} = \frac{c_{\text{L}}^v}{4d_v}(2N - 1), \tag{4.24}$$

where $N\epsilon\{1, 2, 3, ..\}$.
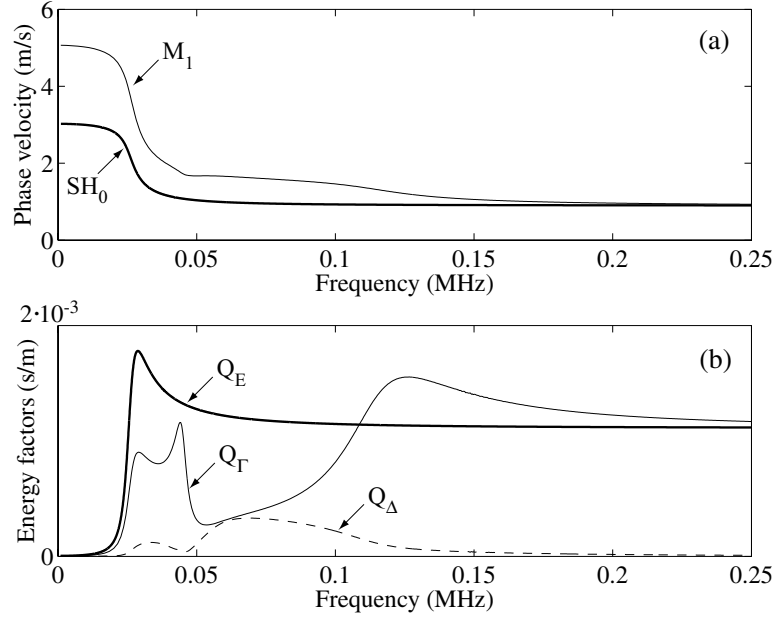
Figure 4.5: (a) Phase velocity; (b) energy factor dispersion curves for the bilayer described in Tab. 4.1: (——) Q_E for the SH_0 mode; (——) Q_Γ for the M_1 mode; $(---)$ Q_Δ for the M_1 mode.

4.5   Elastic energy factor dispersion

The frequency dependence of the energy factors Q_Γ and Q_Δ is much more complex than that of the SH wave energy factor, Q_E (see Sec. 3.5). Fig. 4.5 provides a comparison between the SH_0 mode and the M_1 mode of Fig. 4.2. While Q_E experiences only one peak (Fig. 4.5b) where the mode jumping occurs, Q_Γ and Q_Δ exhibit several peaks due to the more tortuous path of M_1. However, it can be noticed that as the frequency tends to infinity, the phase velocity of M_1 tends to that of SH_0. Moreover, Q_Γ tends to Q_E whereas Q_Δ vanishes. The reason for this behaviour is that at high frequencies, the two SV bulk waves in the equivalent viscoelastic layer become dominant while the L and SV bulk waves in the metallic plate become evanescent. This is because the phase velocity of M_1 becomes lower than the longitudinal and shear bulk velocities of the metallic plate

$$c_{ph} = \frac{\omega}{\xi} < c^e_{\mathrm{L,S}} \Rightarrow \xi > \frac{\omega}{c^e_{\mathrm{L,S}}}. \tag{4.25}$$

For plane waves in the metallic layer ξ has to be lower than $\omega/c^e_{\mathrm{L,S}}$ [which are the moduli of the wavenumbers of the bulk waves, see eq. (2.42)] as it is the projection

of the wavenumber along the bilayer interface. Therefore, in order to realize the condition (4.25) the wavenumbers need to be complex, and the bulk waves become evanescent. Moreover, the lower the phase velocity of the guided mode the higher is the attenuation of the evanescent waves, and as a consequence the lower the energy in the metallic plate.

Even though in the case shown in Fig. 4.5, Q_Δ is always lower than Q_Γ this is not generally true for the other modes as will be shown in the next Chapter, and it is not possible to state general properties for all the modes as in the case of SH waves.
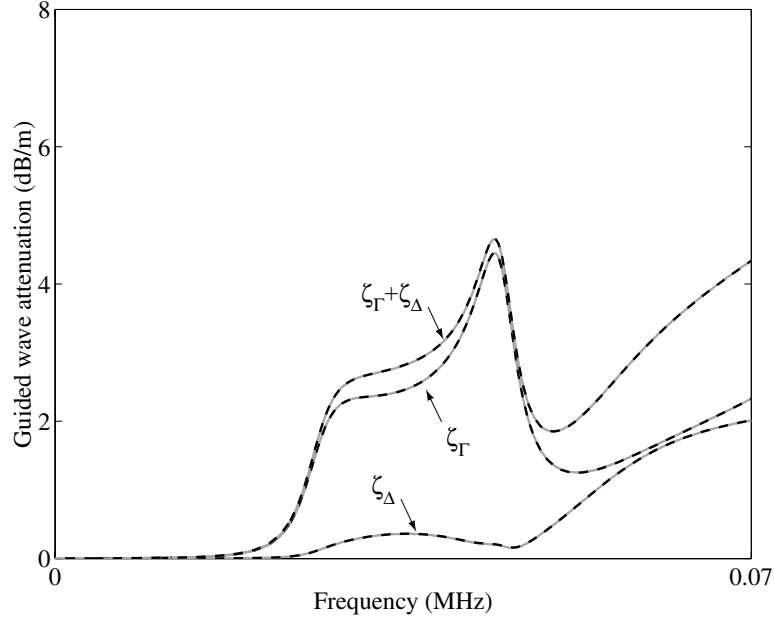
Figure 4.6: Comparison between the first order approximation $(---)$ and the numerical solution ($\rule{1em}{0.4pt}$): ζ_Δ attenuation of $\bar{M}_1$ for $\bar{\alpha}_\mathrm{S} = 0$ and $\bar{\alpha}_\mathrm{L} = 0.01np/wl$; ζ_Γ attenuation of $\bar{M}_1$ for $\bar{\alpha}_\mathrm{S} = 0.01np/wl$ and $\bar{\alpha}_\mathrm{L} = 0$.

4.6   Low material attenuation

The analysis of the dispersion of the equivalent bilayer energy factors allows the guided wave attenuation to be obtained through (4.20). Fig. 4.6 shows a comparison between the first order approximation (dashed lines) and the numerical solution of the exact dispersion equation (grey lines), obtained by using the software Disperse [34]. The curves refer to the bilayer of Tab. 4.1. The curve ζ_Δ provides the attenuation of the Lamb mode M_1 for $\bar{\alpha}_\mathrm{S} = 0np/wl$ and $\bar{\alpha}_\mathrm{L} = 0.01np/wl$. Conversely, ζ_Γ gives the guided wave attenuation associated with M_1 when $\bar{\alpha}_\mathrm{S} = 0.01np/wl$ and $\bar{\alpha}_\mathrm{L} = 0np/wl$. Lastly the grey solid curve labelled $\zeta_\Gamma + \zeta_\Delta$ is the exact dispersion for $\bar{\alpha}_\mathrm{S} = \bar{\alpha}_\mathrm{L} = 0.01np/wl$ while, the dashed line is the superposition of ζ_Δ and ζ_Γ. In all cases, the linear approximation, is in excellent agreement with the numerical solutions. Therefore, the guided wave attenuation of Lamb modes can be obtained as a superposition of the guided wave attenuation due to the bulk longitudinal attenuation $\bar{\alpha}_\mathrm{L}$ and the bulk shear attenuation $\bar{\alpha}_\mathrm{S}$ taken separately.

As was discussed in section 4.3, in order to characterise the dispersion of the vis-
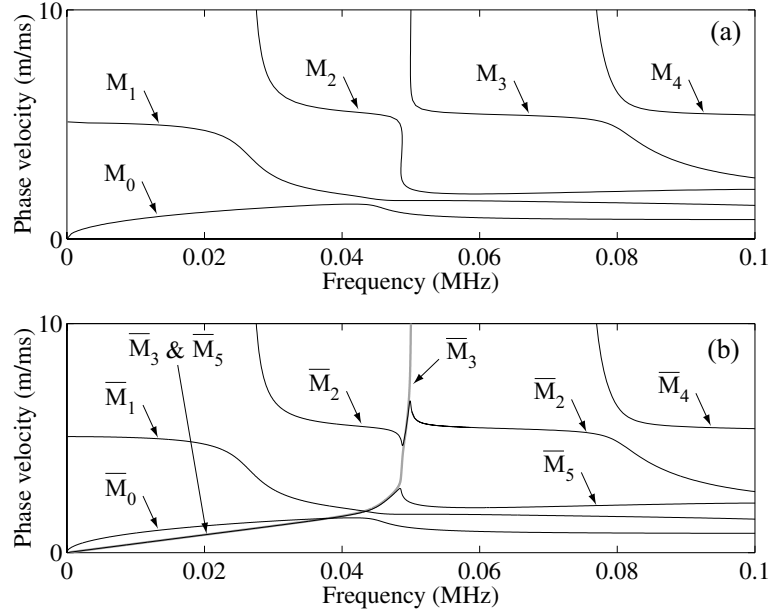
Figure 4.7: Lamb wave phase velocity dispersion curves for the bilayer described in Tab. 4.1: (a) elastic case; (b) $\bar{\alpha}_{\mathrm{S}} = \bar{\alpha}_{\mathrm{L}} = 0.01 np/wl$.

coelastic bilayer through the equivalent elastic bilayer, both the propagating and nonpropagating modes have to be considered. Fig. 4.7b shows the phase velocity dispersion curves of Lamb waves for a slightly attenuative bilayer ($\bar{\alpha}_{\mathrm{S}} = \bar{\alpha}_{\mathrm{L}} = 0.01 np/wl$). These curves almost overlap those of the elastic bilayer, shown in Fig. 4.7a, with the exception of certain regions. In particular, the modes $\bar{M}_0$ and $\bar{M}_1$ are essentially the same as M_0 and M_1. As the frequency increases, the mode $\bar{M}_2$ follows M_2 up to $0.05 MHz$ and then suddenly joins M_3. The mode $\bar{M}_5$ overlaps M_2 above $0.05 MHz$. However, at lower frequencies, $\bar{M}_5$ follows a path which does not belong to the dispersion curves of the elastic bilayer. Similar branches have been observed in the case of Lamb waves propagating in a free isotropic viscoelastic layer [44]. $\bar{M}_3$ (shown in grey) overlaps $\bar{M}_5$ at low frequency, and then jumps to the trajectories of M_2 and M_3 (Fig. 4.7a). Moreover, the power flow of $\bar{M}_3$ is negative as the energy flows along $-\hat{x}_1$. As consequence, the attenuation and the group velocity are negative. The anomalous behaviour of $\bar{M}_3$, and the presence of the unexpected branch of $\bar{M}_5$ at low frequency, which do not occur in the case of SH waves, are due to the presence of nonpropagating modes with non purely imaginary ξ in the dispersion curves of the elastic bilayer (see Chapter 6).

4.7　Large material damping

High material damping is accompanied by large imaginary parts of the Lamé constants which make the zero and first order approximations less accurate. Moreover, the large dispersion of the Lamé moduli may cause high dispersion of the energy factors of the artificial bilayer (Sec. 4.3). As a result, the energy factors obtained for the equivalent bilayer need to be corrected through the perturbation factors. However, as the frequency dependence of the acoustic properties of a viscoelastic material cannot be stated in a general form holding for all the different viscoelastic materials (whereas all Newtonian fluids can be described by one dispersion relationship which depends on one parameter, the viscosity, for a generic viscoelastic material an infinite number of parameters would be required) in the following, the perturbation factor will be neglected. Additionally, the bulk attenuation per wavelength is assumed not to vary with frequency.

Fig. 4.8a shows the phase velocity dispersion curves for Lamb waves propagating in the bilayer described in Tab. 4.1 when a large material attenuation is considered ($\bar{\alpha}_{\mathrm{S}} = \bar{\alpha}_{\mathrm{L}} = 1np/wl$). These curves are considerably different from those obtained in the elastic case (see Fig. 4.7a). In particular, the mode jumping phenomenon, which occurs for the elastic bilayer, has now disappeared. For instance, the trajectory of the $\bar{M}_1$ mode oscillates around that of the free elastic plate mode S_0 rather than jumping to M_1', A_0 and M_2' as happened in the elastic bilayer (see Fig. 4.4). Similarly the M_0 mode follows the A_0 mode path rather than veering toward M_1'. On the other hand, $\bar{M}_2$ follows the trajectory of the clamped free viscoelastic layer M_1' mode rather than jumping to S_0. In general, each bilayer mode follows the trajectory of one asymptotic mode only. A similar phenomenon occurs for Lamb wave propagation in free plastic plates. Chan and Cawley [45] showed that for a large material damping, the Lamb modes split into two families of modes which correspond to the modes of a fluid layer in vacuum (which has zero shear velocity) and those of an artificial layer in vacuum which only supports shear waves (with
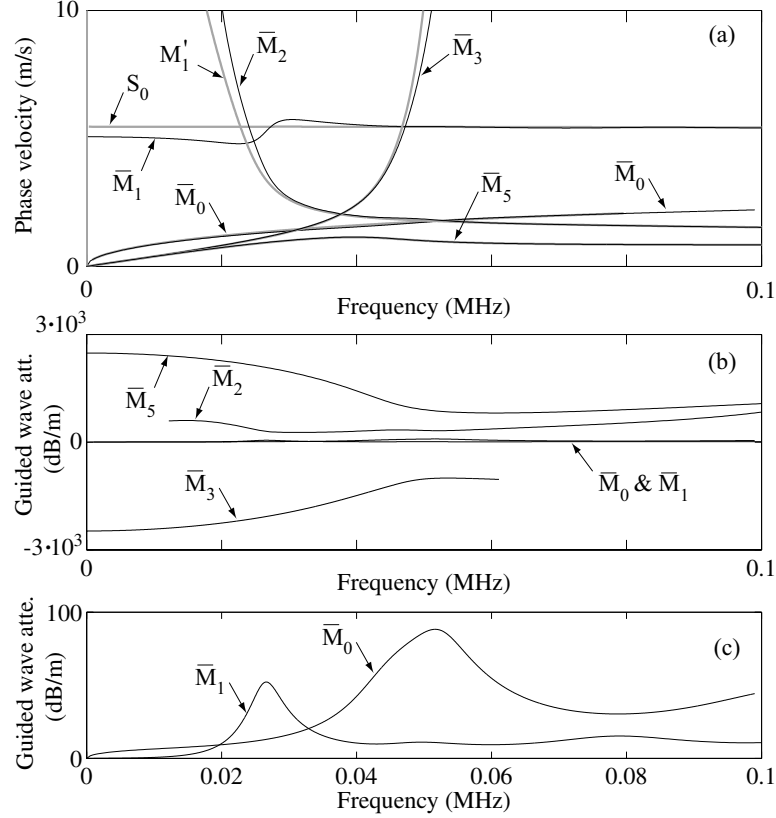
Figure 4.8: Lamb wave dispersion curves for the bilayer described in Tab. 4.1 with $\bar{\alpha}_{\mathrm{S}} = \bar{\alpha}_{\mathrm{L}} = 1 np/wl$: (——) asymptotic solution; (——) bilayer modes: (a) phase velocity; (b) guided wave attenuation; (c) attenuation of the $\bar{M}_0$ and $\bar{M}_1$ modes.

zero longitudinal velocity). These two families have the same role as the asymptotic modes discussed studied in this thesis since Lamb modes in elastic plates can be thought of as an interaction between them as demonstrated by Überall *et* al. [38].

The absence of the mode jumping between the bilayer modes leads to the intersection of the phase velocity spectra of different modes. However, these intersections do not correspond to mode intersections, since two different modes would only intersect each other at a given frequency if the couples (c_{ph}, ζ) were the same for both modes. As an example, $\bar{M}_1$ and $\bar{M}_2$ cross in phase velocity (Fig. 4.8a) but they do not in attenuation (Fig. 4.8b).

The $\bar{M}_3$ has negative attenuation. This is because the mode originates from the complex branches of the M_2 mode of the elastic bilayer whose power flow is directed
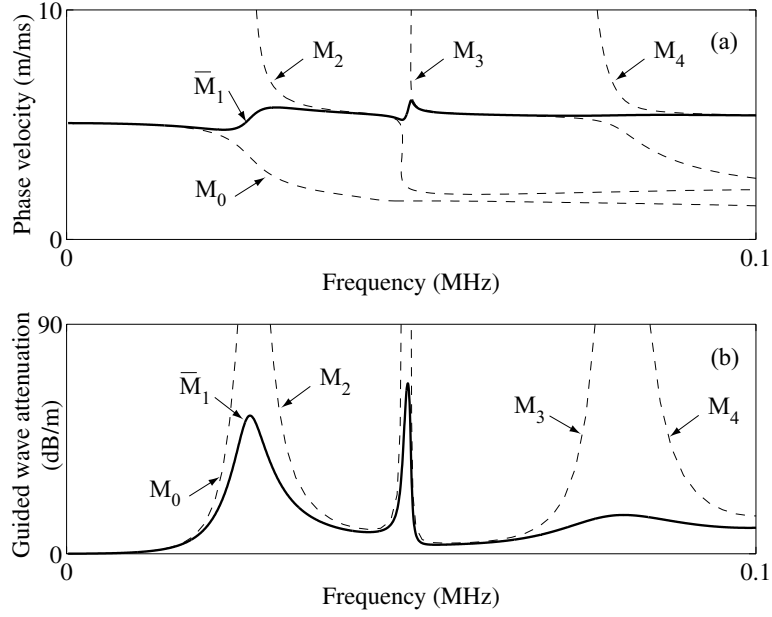
Figure 4.9: Lamb dispersion curves for the bilayer described in Tab. 4.1 with $\bar{\alpha}_{\mathrm{S}} = 1np/wl$ $\bar{\alpha}_{\mathrm{L}} = 0$: (a) phase velocity for $\bar{M}_1$ (——) and the lower modes of the elastic bilayer $(---)$; (b) attenuation of $\bar{M}_1$ (——) and first order approximation $(---)$.

along $-\hat{x}_1$ as mentioned earlier.

Fig. 4.8b shows that the bilayer modes $\bar{M}_1$ and $\bar{M}_0$, which follow the S_0 and A_0 modes of the free elastic plate, have much lower attenuation than the modes that follow the clamped-free modes of the viscoelastic layer. This is due to the fact that in the second case the energy is mainly trapped in the viscoelastic layer while the energy associated with $\bar{M}_1$ and $\bar{M}_0$, flows primarily in the elastic plate. As a consequence, only the modes which tend to the free elastic plate modes can be practically employed. Fig. 4.8c is a comparison between the attenuation spectra of $\bar{M}_0$ and $\bar{M}_1$. Since the attenuation of $\bar{M}_0$ is usually larger than that of $\bar{M}_1$ (especially at low frequency), $\bar{M}_1$ is more attractive than $\bar{M}_0$ for travelling long distances in the bilayer. Fig. 4.9 shows the dispersion curves of this mode (thick solid line) when only a large bulk shear attenuation is considered, the longitudinal attenuation is set to zero. The dashed lines in Fig. 4.9a represent the modes of the elastic bilayer while, the dashed lines in Fig. 4.9b are the guided wave attenuation spectra calculated through the first order approximation 4.20. Note that the dashed lines in Fig. 4.9b have been

labelled M_1, M_2 etc. in order to show the correspondence with the elastic modes of Fig. 4.9a. It is interesting to note that the attenuation spectrum exhibits peaks which occur at the transitions where the phase velocity changes rapidly and mode jumping would occur if the bilayer was elastic. These peaks are due to a resonance phenomenon which causes maximum energy transfer from the metallic plate into the viscoelastic layer (see previous Chapter). The resonances would not occur if the viscoelastic layer was infinitely thick.

The first order approximation provides a satisfactory approximation in the plateau zones of the dispersion curves, while it becomes inaccurate around the guided wave attenuation maxima.

4.8 Summary

The propagation of Lamb waves in metallic plates coated with viscoelastic layers has been investigated.

A general formulation relating the guided wave attenuation to the amount of strain energy stored in the viscoelastic layer per unit in-plane power flow has been derived. It has been shown that the strain energy can be split in two parts, δ and γ, which account separately for the effects of the two material bulk attenuations (longitudinal and shear) on the attenuation of the guided wave.

The topology of the dispersion curves of the elastic bilayer experiences substantial modifications when internal damping is considered. In particular, due to the energy dissipation within the attenuative layer, a mode is always propagating and its dispersion strongly depends on the magnitude of the internal damping. Two different material attenuation regimes can be defined. In the low regime, a bilayer mode embraces both the nonpropagating and propagating branches of the corresponding elastic mode. The non purely imaginary complex branches of the elastic bilayer dispersion curves cause anomalies in the phase velocity and guided wave attenuation

spectra. For large values of the material attenuation, the modes can be classified as: a) modes whose energy travels primarily in the elastic plate; b) modes whose energy is trapped in the viscoelastic layer. While the modes of the second family have little practical interest, as they are highly attenuated with distance, the modes of the first family can be employed in suitable frequency ranges. In particular, the attenuation spectra of these modes exhibit peaks which occur roughly at the through-thickness resonance frequencies of the viscoelastic layer if it were considered elastic and rigidly clamped at the bilayer interface.

The results obtained in this Chapter can be extended to the case of longitudinal modes propagating in coated pipes when the diameter to wall thickness ratio is large. In the case of large material damping, $\bar{M}_1$ is the mode which has the lowest attenuation since its energy mainly travels in the metallic plate. The frequencies which minimise the attenuation of $\bar{M}_1$ maximise the propagation distance, so providing the best conditions for long range inspections.

It is now clear that the modes which must be employed in order to maximise the range of inspection are SH_0 and $\bar{M}_1$. However, it is not yet clear which of them results in the longest propagation distance. Since the ultimate goal of this thesis is to identify the mode which provides the largest range of inspection, in the next Chapter, the characteristics of SH and Lamb waves will be compared.

Chapter 5

Comparison between Lamb and SH waves

5.1 Background

In Chapters 3 and 4 the attenuation characteristics of SH and Lamb waves have been considered separately. This chapter provides a comparison between the attenuation levels associated with the propagation of SH waves and those corresponding to Lamb waves when the same power flows through the bilayer cross section. Since for pipelines with large diameter to wall thickness ratio torsional and longitudinal modes correspond to SH and Lamb waves, the aim of such a comparison is to establish, at each frequency, whether torsional modes are more attenuated than longitudinal waves or vice versa.

In Sec. 5.2 the guided wave attenuation spectra are compared in the low material absorption regime, while in Sec. 5.3 large material attenuation is considered. The dispersion curves showed in Chapters 3 and 4 refereed to specific geometric and acoustic properties of the bilayer. In Sec. 5.4 the possibility of deriving two approximate dispersion curves which can provide the guided wave attenuation of SH and Lamb waves for any bilayer at any frequency is considered.

5.2   Low material damping

In order to compare the guided wave attenuation of SH and Lamb modes in the low damping regime the linear expressions (3.39) and (4.20) are employed.

As has been pointed out in the previous Chapter, the frequency dependence of the energy factors Q_Γ and Q_Δ [see (4.16) and(4.15)] is much more complex than that of the energy factor Q_E [see (3.15)]. However, for practical purposes, a mode can only be employed in the frequency ranges in which its phase velocity is not too dispersive since high dispersion is accompanied by a strong distortion and amplitude decay of the wave packet over long propagation distances. For this reason, in the following, the comparison between Lamb and SH waves is confined to the plateau regions of the dispersion curves. In Fig. 5.1 five different zones, labelled A, B, C, etc., have been identified for the plateaus of the modes of the bilayer described in Tab. 4.1. The corresponding energy factor curves are shown in Fig. 5.2. Note that for clarity, the energy factor dispersion curves refer to the plateau regions of the bilayer modes only.

In zone A, Q_E is always larger than Q_Γ while Q_Δ is negligible. This is proved in Appendix A. Since the Lamb wave attenuation is a linear combination of Q_Γ and Q_Δ through the bulk attenuations $\bar{\alpha}_L$ and $\bar{\alpha}_s$ it follows that the role of the longitudinal attenuation $\bar{\alpha}_L$ is negligible compared to $\bar{\alpha}_s$ and it can be assumed that

$$\zeta_{Lamb} \simeq f\bar{\alpha}_s Q_\Gamma. \tag{5.1}$$

Moreover, as $Q_E \gg Q_\Gamma$ [see equation A.18] the guided wave attenuation of the SH_0 mode is much larger than that of M_1.

Close to the lower limit of zone B (Fig. 5.2), the relationship between the energy factors is the same as in zone A. However, as the frequency increases the inequality changes, and at the upper limit of zone B it is inverted (i.e. $Q_E < Q_\Gamma < Q_\Delta$). This is due to the fact that zone B ends at the second cutoff frequency of the bilayer Lamb modes. This frequency is characterised by longitudinal through-thickness standing waves which have large ε_0 which implies that $\delta > \gamma$ (see (4.11) and (4.12)).
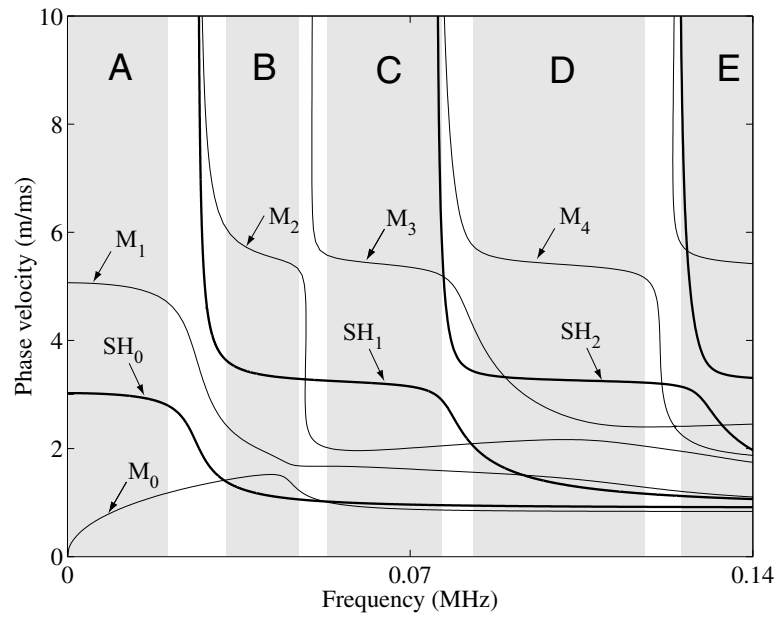
Figure 5.1: The grey bands identify the plateau zones in the dispersion curves of the bilayer: (———) Lamb waves; (━━━) SH waves.
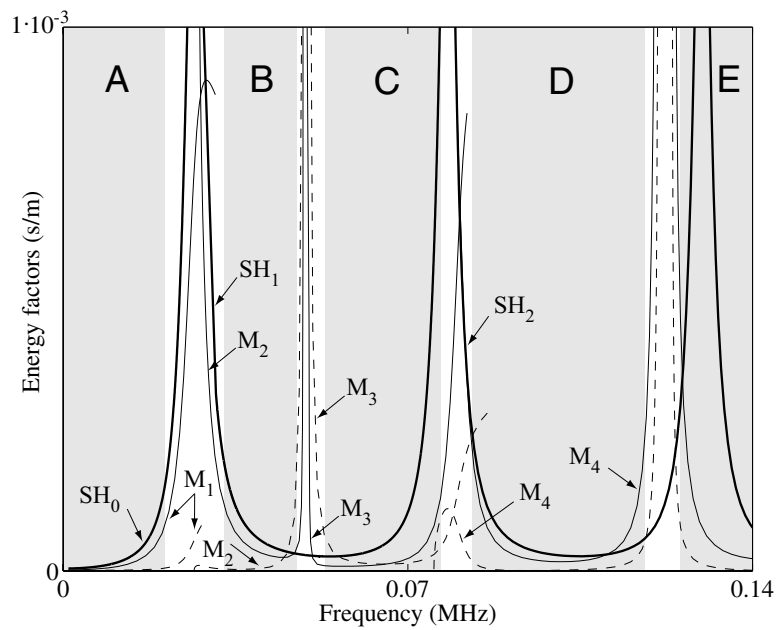
Figure 5.2: Bilayer energy factors: (———) Q_Γ; (− − −) Q_Δ; (━━━) Q_E.

Close to the lower limit of zone C (Fig. 5.2), the energy factors behave as in the upper limit of zone B, while the situation is inverted as the frequency reaches the upper limit of zone C. Here, the third cutoff for Lamb and the second cutoff for SH waves occur. These cutoffs are characterised by shear through-thickness standing waves and consequently $Q_E > Q_\Gamma > Q_\Delta$. Similar considerations hold for all the other zones.

It can be concluded that, in the low material damping regime, the attenuation of Lamb modes is higher than that of SH waves only around the longitudinal cutoff (4.24) of the equivalent bilayer, while in the rest of the spectrum, SH waves are more attenuated.

5.3   Large material damping

As shown in Chapters 3 and 4 when the material damping is large, the modes which tend to the first asymptotic family (modes of the free metallic plate) exhibit the lowest attenuation since the energy primarily flows in the non attenuative layer. Moreover, within the first family, the modes which have the lowest attenuation are SH_0 and $\bar{M}_1$. Therefore, here only these two modes are compared since they provide the highest potential for long range inspections.

Fig. 5.3 provides a comparison between $\bar{M}_1$ and SH_0. In this analysis the bulk longitudinal attenuation is neglected at first (solid lines). The two modes experience the first attenuation peak at the same frequency since the first cutoff frequency is the same for both modes [see eq. (4.23)]. Moreover, in the frequency interval around the first cutoff (0.03MHz in Fig. 5.3), the guided wave attenuation of the SH_0 mode is larger than that of $\bar{M}_1$. This follows from the fact that in the zone A (Fig. 5.2), SH_0 requires a higher strain energy than $\bar{M}_1$ in order to produce unit power flow as has been shown in Sec. 5.2. However, as the frequency approaches the second cutoff frequency (0.05MHz in Fig. 5.3) of the Lamb mode M_3 [eq. (4.24), upper limit of zone B Fig. 5.2], $\bar{M}_1$ has another maximum, while the SH_0 attenuation tends to
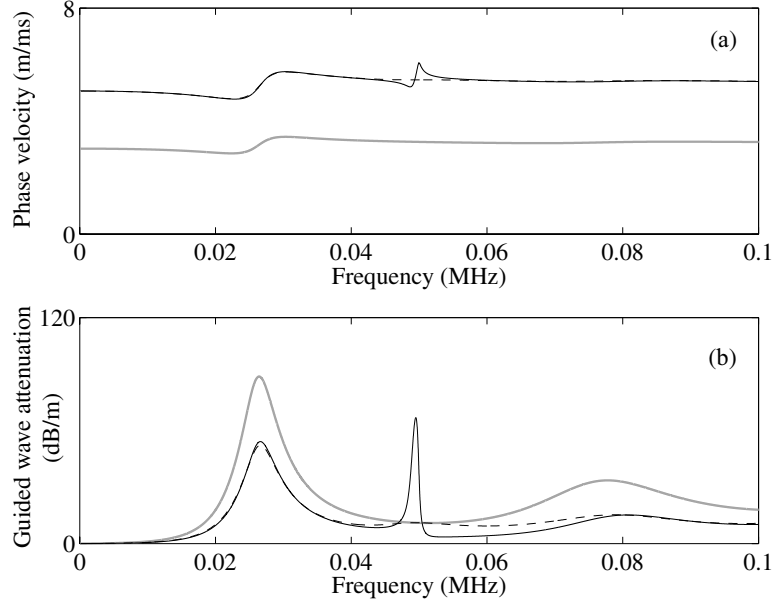
Figure 5.3: Dispersion curves for the bilayer of Tab. 4.1 with $\bar{\alpha}_{\mathrm{S}} = 1np/wl$:(———) SH_0; (———) $\bar{M}_1$ with $\bar{\alpha}_{\mathrm{L}} = 0$; (− − −) $\bar{M}_1$ with $\bar{\alpha}_{\mathrm{L}} = 1np/wl$.

its minimum. On the other hand, if the bulk longitudinal attenuation is considered (dashed line), the second sharp peak disappears. It can be observed that this attenuation maximum is due to a destructive interference phenomenon between the energy reflected at the bilayer interface and the energy reflected from the free face of the viscoelastic layer as was addressed in Sec. 3.7. At this frequency the strain energies, δ and γ [eqs. (4.11) and (4.12)], are primarily carried by longitudinal partial waves. As a consequence, if the longitudinal attenuation increases, the viscoelastic layer behaves as if it were infinitely thick (since all the energy transmitted from the metallic plate is lost into the bulk of the viscoelastic layer) and interference no longer occurs. Moreover, the $\bar{M}_1$ mode is sensitive to the longitudinal bulk attenuation around the peak frequencies given by (4.24) only since, over the rest of the spectrum, the energy in the viscoelastic layer travels in the form of γ energy rather than δ according to Sec. 5.2.

5.4 Universal curves

The aim of this section is to provide a set of curves which enables the prediction of the attenuation of SH and Lamb waves propagating in the bilayer as a function of the frequency and the bilayer acoustic properties and geometry. This can be done by introducing an approximate relationship between two non-dimensional parameters which involve all the variables of the problem (acoustic properties, geometry, densities, frequency and guided wave attenuation).

Let us consider the case of SH_0 first. It has been shown in Chapter 3 that guided wave attenuation minima occur at the Love transition frequencies. Moreover, it has been demonstrated that in both low and large material damping regimes, the first order approximation (3.39) provides accurate results.

Consider the expression of the first energy factor Q_{E} at the Love transition frequencies (3.37). Under the hypothesis of $c_{\mathrm{s}}^v \ll c_{\mathrm{s}}^e$, in the first order approximation, eq. (3.37) becomes

$$Q_{\mathrm{E}} \simeq \frac{1}{2c_{\mathrm{s}}^e} \frac{\rho^v d_v}{\rho^e d_e} = \frac{1}{2c_{\mathrm{s}}^v} \frac{Z^v d_v}{Z^e d_e}, \tag{5.2}$$

where Z is the material shear impedance ($Z = \rho c_{\mathrm{s}}$). As a consequence, by substituting (5.2) into (3.39) the guided wave attenuation becomes

$$\zeta \simeq \frac{f \bar{\alpha}_{\mathrm{s}}^v}{2c_{\mathrm{s}}^v} \frac{Z^v d_v}{Z^e d_e}, \tag{5.3}$$

which rearranging gives

$$\frac{\zeta d_e Z^e}{\bar{\alpha}_{\mathrm{s}}^v Z^v} = \frac{1}{2} \frac{f d_v}{c_{\mathrm{s}}^v}. \tag{5.4}$$

This expression is in the form

$$Y = \frac{1}{2} X, \tag{5.5}$$

where the non-dimensional groups X and Y are defined as

$$X = \frac{f d_v}{c_{\mathrm{s}}^v}, \tag{5.6}$$

$$Y = \frac{\zeta d_e Z^e}{\bar{\alpha}_{\mathrm{s}}^v Z^v}, \tag{5.7}$$
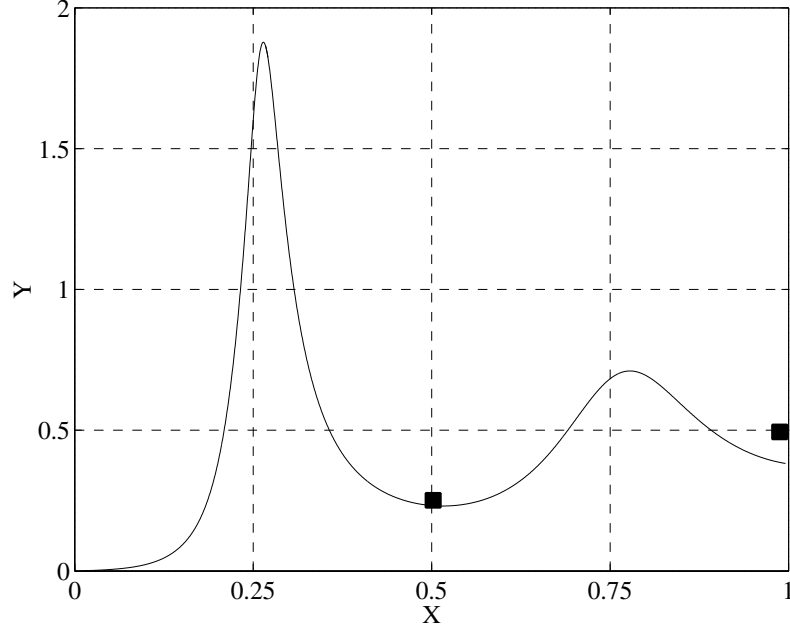
Figure 5.4: Non dimensional representation of the attenuation spectrum for SH_0.

note that $\bar{\alpha}_{\mathrm{s}}^{v}$ is non-dimensional and ζ is $[m^{-1}]$. While X can be thought of as a non-dimensional frequency, Y gives an appreciation of the guided wave attenuation. This suggests a possible transformation of guided wave attenuation spectra ζ versus f to non-dimensional X versus Y form. From (5.5) it follows that if the minima of the guided wave attenuation spectra of SH_0 are transformed according to (5.6) and (5.7), they always correspond to the same points of the $X - Y$ plane regardless of the bilayer material and geometry. Figure 5.4 provides a comparison between the approximation at the Love transition frequencies (5.5) (black squares) and the SH_0 attenuation spectrum calculated for the bilayer of Tab. 4.1 when $\bar{\alpha}_{\mathrm{s}}^{v} = 1$ (solid line). This spectrum, which has been obtained by transforming the attenuation spectrum of SH_0 (calculated for the bilayer of Tab. 4.1 with $\bar{\alpha}_{\mathrm{s}}^{v} = 1$) according to (5.6) and (5.7), will be referred in the rest of this Chapter to as the non-dimensional attenuation spectrum. Around the first Love transition frequency ($X = 0.5$) the exact solution and the approximation (5.5) are very close. However, (5.5) becomes less accurate as the frequency increases (see $X = 1$) due to the increase of the bulk attenuation.

As was explained in Chapter 3 the guided wave attenuation maxima approximately

Table 5.1: Material parameters and geometry for different bilayers.

Bilayer	Layer Material	c_s (m/ms)	c_L (m/ms)	ρ (kg/m^3)	Thickness (mm)
I	Bitumen	900	1700	1250	9.00
	Steel	3260	5960	7930	8.00
II	Epoxy	1100	2610	1170	7.00
	Steel	3260	5960	7930	5.00
III	Perspex	1430	2730	1180	7.00
	Steel	3260	5960	7930	10.00
IV	Epoxy	1100	2610	1170	7.00
	Brass	2200	4400	8400	10.00

occur at the through thickness resonances of the clamped-free viscoelastic layer if it is considered elastic, these frequencies being given by $X = 0.25, 0.75$ [see (4.23)]. Therefore if the attenuation spectrum of SH_0 is transformed according to (5.6) and (5.7), its maxima will approximately occur at the same abscissas $X = 0.25, 0.75$, as shown in Fig. 5.4.

As a consequence, for any bilayer made of a stiff and heavy elastic plate coated with a soft and light attenuative layer, if the guided wave attenuation of the SH_0 mode is transformed according to (5.6) and (5.7), the minima of the guided wave attenuation spectrum always correspond to the same positions in the $X - Y$ plane and the maxima of the attenuation spectrum correspond to the same abscissa X. This suggests that any guided wave attenuation spectrum might correspond to the solid line shown in Fig. 5.4 if transformed according to (5.6) and (5.7). However, there are two considerations to take into account. Firstly, the correspondence is only an approximation as the characteristic equation (3.3) cannot be expressed as a function of X and Y only. Secondly, the correspondence will be more accurate around the attenuation minima since there the first order approximation is more accurate (see Sec. 3.6).

Figure 5.5 shows the non-dimensional attenuation spectra of the SH_0 mode propagating in different types of bilayers whose characteristics are summarized in Tab. 5.1 with $\bar{\alpha}_s^v = 1np/wl$. As expected, different curves overlap well around the guided wave attenuation minima, whereas some differences occur in the regions of attenuation maxima ($X = 0.25, 0.75$). These differences become larger if the bulk attenuation $\bar{\alpha}_s^v$ is increased since the guided wave attenuation exhibits a strongly non-linear behaviour with $\bar{\alpha}_s^v$. This is shown in Fig. 5.6 which provides the non-dimensional dispersion curves for the bilayer I (see Tab. 5.1) when $\bar{\alpha}_s^v$ is increased up to 1.75np/wl. As pointed out before, around the attenuation minima, the different curves are very close each other. On the other hand, around the attenuation maxima, Y monotonically decrease with $\bar{\alpha}_s^v$ or in other words, the guided wave attenuation decreases as $\bar{\alpha}_s^v$ increases. This can be explained on the basis of the argument discussed in Sec. 3.7 where has been shown that the attenuation peaks are due to the destructive interference between the reflections from the bilayer interface and the back of the viscoelastic layer. Therefore, as $\bar{\alpha}_s^v$ increases, the reflection from the back of the viscoelastic layer decreases and the cancellation effect becomes weaker, resulting in a reduction of the guided wave attenuation.

At this stage, it is clear that the non-dimensional attenuation spectra associated with different bilayers can be considered coincident over limited intervals of the X domain, see grey zones in Fig 5.7. Moreover, in these intervals, the non-dimensional dispersion curve can be regarded as a universal curve since it is representative of the attenuation of SH_0 propagating in any bilayer, provided that the non attenuative layer is much stiffer and heavier than the viscoelastic one. On the other hand, around the Y maxima, the non-dimensional spectrum depends on the characteristics of the bilayer, although the abscissas X where the maxima occur are universal (all the peaks occur around $X = 0.5, 1, etc.$).

The curve shown in Fig. 5.7 becomes extremely valuable for practical testing as it provides accurate estimates of the guided wave attenuation when $X < 0.25$ and $0.25 < X < 0.5$ but it also defines the conditions which result in the largest guided wave attenuation. In other words, Fig. 5.7 identifies the conditions which minimise
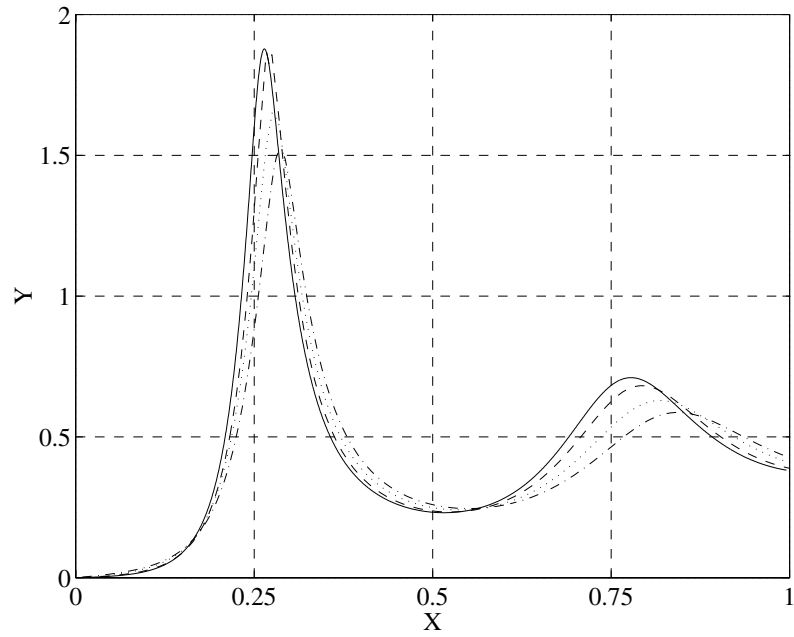
Figure 5.5: Non dimensional attenuation spectra for SH_0 propagating in the bilayers of Tab. 5.1: (——) I; $(- - -)$ II; $(\cdots\cdots)$ III; $(- \cdot -\cdot)$ IV.
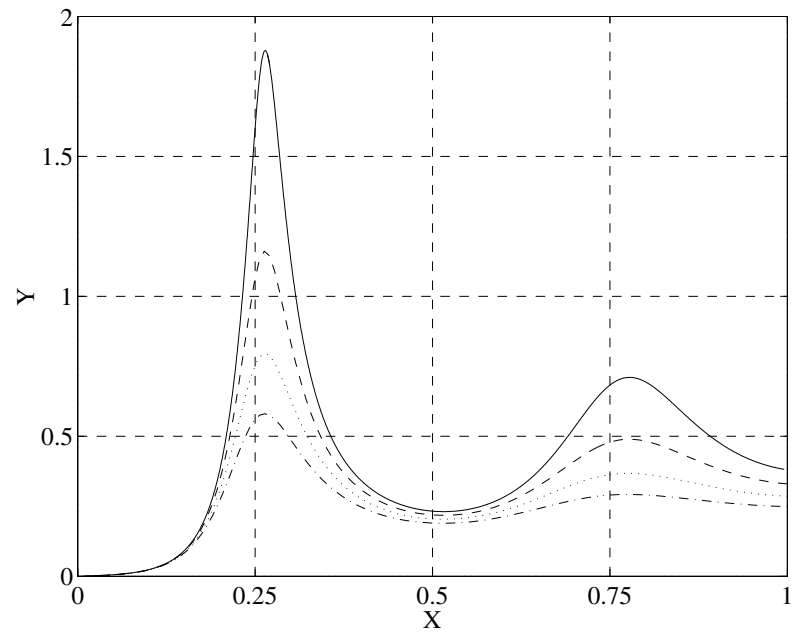
Figure 5.6: Non dimensional attenuation spectra for SH_0 propagating in the bilayer of Tab. 4.1 for different values of the bulk attenuation: (——) $\bar{\alpha}_\mathrm{s} = 1np/wl$; $(- - -)$ $\bar{\alpha}_\mathrm{s} = 1.25np/wl$; $(\cdots\cdots)$ $\bar{\alpha}_\mathrm{s} = 1.50np/wl$; $(- \cdot -\cdot)$ $\bar{\alpha}_\mathrm{s} = 1.75np/wl$.
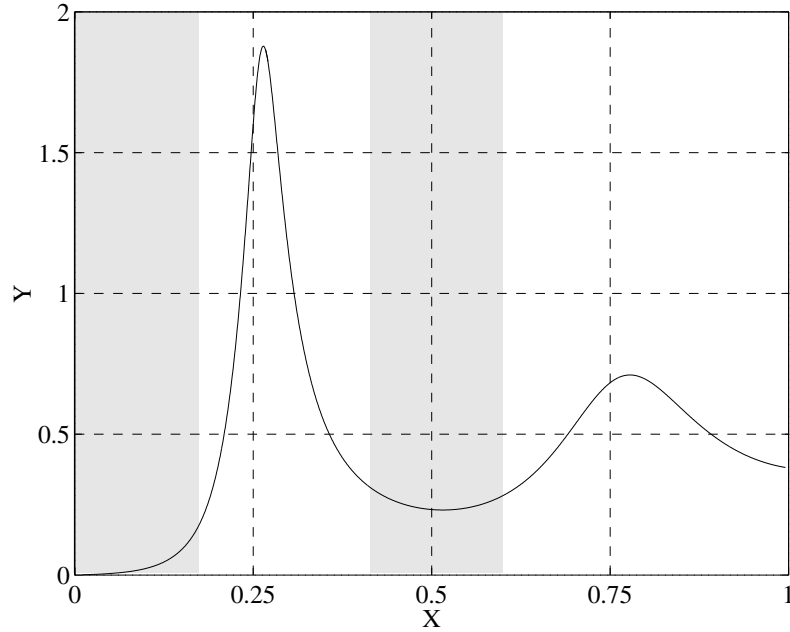
Figure 5.7: Universal chart for the SH_0 mode attenuation characterisation.

the guided wave attenuation so defining the practicability of tests. Moreover, the fact that in the regions of maximum Y the curve cannot predict the guided wave attenuation accurately has little practical relevance, as in these regions the attenuation is extremely high and the guided mode would be completely attenuated after travelling a short distance.

Let us now consider the attenuation spectra of the $\bar{M}_1$ mode. The similarity between the dispersion curves shown in Fig. 5.3 suggests that the attenuation spectrum of $\bar{M}_1$ can also be transformed through (5.6) and (5.7) in certain ranges of X. This is shown in Fig. 5.8 which refers to the different bilayers described in Tab. 5.1 when $\bar{\alpha}_{\mathrm{S}}^v = 1$ and $\bar{\alpha}_{\mathrm{L}}^v = 0.1$. Around the first attenuation peak the transformation (5.6) (5.7) leads to results which are quite similar to the SH_0 case and for low values of X the non-dimensional spectra are coincident. However, as X approaches 0.5 the curves no longer superimpose. This is due to the presence of a longitudinal mode cutoff as discussed in Sec. 5.3 which cannot be transformed through (5.6). For each curve the relative distance between the abscissa of the second maximum, X_2, and the abscissa of the first maximum, X_1, can be related to the bulk velocities of the
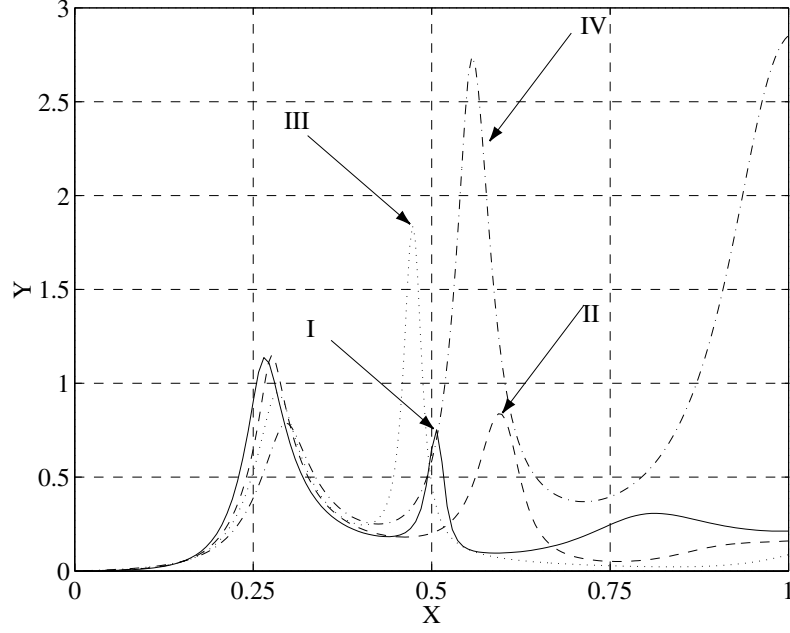
Figure 5.8: Non dimensional attenuation spectra for $\bar{M}_1$ propagating in the bilayers of Tab. 5.1: (———) I; $(- - -)$ II; $(\cdots\cdots)$ III; $(- \cdot -\cdot)$ IV.

viscoelastic layer according to

$$\frac{X_2}{X_1} = \frac{c_L^v}{c_S^v} \tag{5.8}$$

which follows from expressions (4.23) and (4.24). Since for many materials $c_L^v \simeq 2c_S^v$ it follows that the second peak occurs around $X_2 = 0.5$. As a consequence, while the amplitude of the non-dimensional spectrum depends on the bilayer properties around $X = 0.5$, the abscissa of the second peak, X_2, can be considered as universal. Therefore, the condition $X = 0.5$ results in a minimum for the guided wave attenuation of SH_0 as it correspond to the first Love transition frequency, and in a maximum for $\bar{M}_1$. Moreover, the non-dimensional spectrum of $\bar{M}_1$ is universal for $X < 0.25$ only.

Figure 5.9 is a superposition of the curve shown in Fig. 5.7 and the non-dimensional attenuation spectrum of $\bar{M}_1$ propagating in bilayer I (see Tab. 5.1). While the non-dimensional spectrum of SH_0 can be considered universal over ΔX_1 and ΔX_2, that of $\bar{M}_1$ is universal over ΔX_1 only. These curves lead to some important general conclusions.
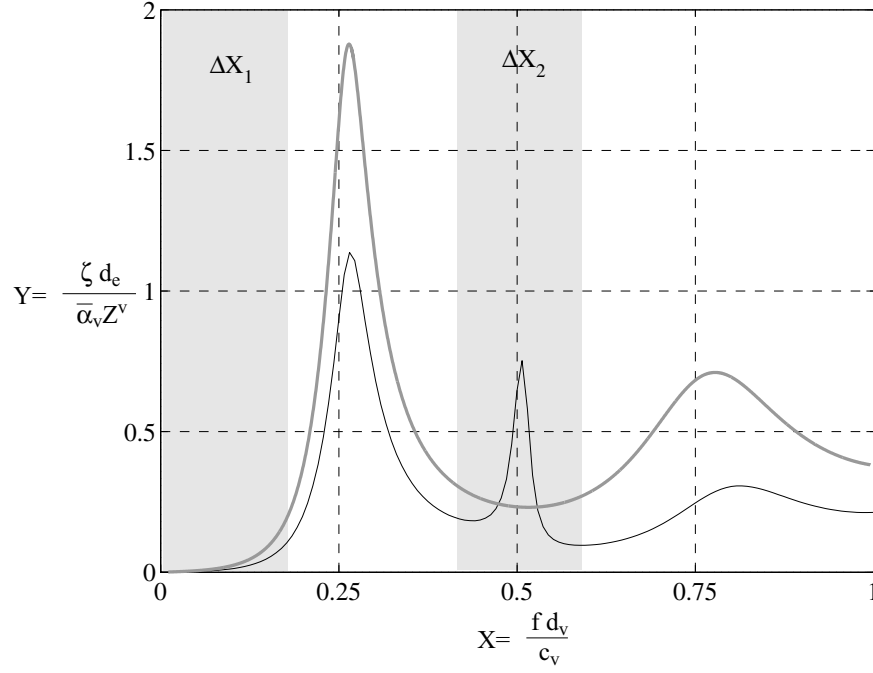
Figure 5.9: Universal non-dimensional attenuation spectra for:(———) SH_0; (———) $\bar{M}_1$.

For low values of X ($X\epsilon\Delta X_1$) the SH_0 mode is always more attenuated than $\bar{M}_1$, this being in agreement with the demonstration provided in Appendix A. As a consequence, at low frequency the $\bar{M}_1$ provides the largest range of inspection.

For $X\epsilon\Delta X_2$ the SH_0 mode is generally less attenuated than $\bar{M}_1$, as in this range the first longitudinal cutoff occurs.

It could be argued that the $\bar{M}_1$ mode is more attractive than SH_0 since it has the lowest guided wave attenuation. However, it is not always possible to perform tests in the region ΔX_1. For instance, in the case of a very thick coating with low shear velocity, in order to have $X\epsilon\Delta X_1$ the frequency needs to be very low [see eq. (5.6)] which might result in a severe reduction of the guided mode sensitivity to defects. In this case, testing in the ΔX_2 range with SH_0 can be beneficial as the frequency can be increased considerably.

5.5 Summary

Universal relationships between the frequency, the guided wave attenuation and the bilayer material properties and geometry have been derived under the hypothesis that the elastic plate is much stiffer and heavier than the viscoelastic layer. These approximate relationships provide a satisfactory accuracy in the frequency ranges where the SH_0 mode attenuation spectrum has minima, and at low frequency for the $\bar{M}_1$ mode.

The comparison between Lamb and SH waves suggests that the guided wave attenuation of SH waves is considerably larger than that of Lamb modes before and immediately after the first attenuation peak. At higher frequencies, the Lamb wave attenuation may be higher than that of the SH mode, depending on the magnitude of the longitudinal attenuation. However, apart from this region, the guided wave attenuation is not sensitive to the magnitude of the longitudinal bulk attenuation.

By virtue of the correspondence between coated pipe and coated plate modes, it can be concluded that long range inspections are not possible where maxima in the non-dimensional curves occur. The critical frequency where the first attenuation maximum occurs is proportional to the ratio between the shear velocity and the thickness of the coating for both longitudinal and torsional modes. At each frequency, the guided wave attenuation decreases with the impedance-thickness product of the pipe wall and increases with the bulk shear attenuation-impedance product of the viscoelastic coating. As a consequence, guided waves can propagate for a long distance in thick metallic pipes coated with thin attenuative layers. Moreover, since tests can be performed at frequencies below the first critical frequency (which is large due to the thin coating), longitudinal modes provide propagation ranges which are much larger than those achievable with torsional modes. On the other hand, a thick coating with low shear velocity leads to a low value of the first critical frequency. Therefore in order to limit the guided wave attenuation, the testing frequency has to be very low. However, the mode sensitivity to defect represents a limit to the extent to which the testing frequency can be reduced. Hence for very thick coatings, the only possibility is to perform tests around the first Love transition frequency,

where the second minimum of the attenuation spectrum of SH_0 occurs. By contrast with the case of thin coatings, the SH_0 mode now has lower attenuation than $\bar{M}_1$ as explained in Sec. 5.4.

Since the first critical frequency strongly depends on the shear velocity of the coating, and due to the dependence of the guided wave attenuation on the shear bulk attenuation of the coating, the feasibility of long range inspections can only be assessed if the shear properties of the coating are known. The characterisation of these properties will be addressed in Chapters 7 and 8.

Chapter 6

Meaning of Lamb mode nonpropagating branches

6.1 Background

The aim of this Chapter is to explain the reason for the low frequency anomalous branches observed in the dispersion curves of Lamb modes propagating in a weakly attenuative bilayer (Fig. 4.7).

The possibility of relating these anomalous branches to the nonpropagating modes of an appropriate elastic system is studied in Sections 6.3 and 6.4 where the modes of an attenuative free plate are studied and subsequently compared with those of the plate considered to be elastic. In Sec. 6.5 the analysis is extended to the bilayer case.

6.2 Previous work

The propagation of stress waves in plates has been extensively studied since Rayleigh [46] and Lamb [47] established the secular equation for the free vibrations of infinite elastic plates in 1889. The study of the dispersion characteristics of propagating modes was initiated by Lamb [48] in 1917 who first investigated the lowest symmetric and antisymmetric modes. In the following half a century, researchers had focused their efforts on the characterisation of the higher order propagating modes by analyzing the dispersion of the real roots (wavenumbers) of the Rayleigh-Lamb equation, [49]. Only in 1955 Lyon [50] calculated the purely imaginary roots of the secular equation which correspond to modes of infinite wavelength starting at the cutoff frequencies of the Lamb modes. A key contribution is the work done by Mindlin who established the existence of modes at the cutoff frequencies whose amplitudes vary linearly with the propagation distance [51] and also demonstrated the presence of complex roots of the Rayleigh-Lamb equation, [52, 53]. A rather complete picture of the topology of real, imaginary and complex wavenumber dispersion is provided by Mindlin [54].

Modes associated with non-real wavenumbers appear to be substantially different from those corresponding to real wavenumbers as they do not carry energy [28] and are exponentially damped with distance (therefore they are generally referred to as nonpropagating modes). As a consequence, there is ground for a sharp separation between propagating and nonpropagating modes on the basis of a strong physical argument such as the energy propagation. However, this separation may lead to a misleading interpretation of the nature of these two families of modes which are representative of the same physical phenomenon, i.e. plate vibrations. This common nature is suggested by the fact that nonpropagating modes, at each frequency, provide the infinity of eigenmodes which, jointly with the finite number of propagating modes, results in a complete set of orthogonal eigenmodes [55]. This, for instance, allows the response of the plate to an arbitrary body force to be studied by expanding the force in terms of the infinite number of plate eigenmodes, both propagating and nonpropagating, according to modal analysis theory [1, 56].
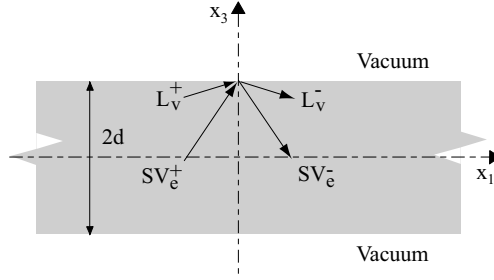
Figure 6.1: Partial waves diagram.

6.3 Dispersion loci

Let us consider a homogeneous, isotropic viscoelastic plate of infinite extent. The motion is independent of the $\hat{x}_2$ direction and takes place in two directions, $\hat{x}_1$, $\hat{x}_3$, the origin being taken in the middle surface of the plate, see Fig. 6.1. The propagation of Lamb waves can be studied by considering two pairs of longitudinal and shear bulk waves as shown in Fig. 6.1. The dispersion equation is obtained by imposing the zero traction condition along the lateral surfaces of the plate which leads to the well known Rayleigh-Lamb equation

$$\frac{\tan q_{\mathrm{s}}b}{\tan q_{\mathrm{L}}b} + \left[\frac{4\xi^2 q_{\mathrm{s}}q_{\mathrm{L}}}{(\xi^2 - q_{\mathrm{s}}^2)^2}\right]^{\pm 1} = 0, \tag{6.1}$$

where ξ is the wavenumber projection along $\hat{x}_1$, q_{L} and q_{s} are the projections of the longitudinal and shear bulk wave wavenumbers along $\hat{x}_3$ and $2b$ is the plate thickness. The plus and minus signs refer to symmetric and antisymmetric modes, respectively.

The first few symmetric modes of a metallic plate (see Tab. 4.1) with low material damping ($\bar{\alpha}_{\mathrm{s}} = \bar{\alpha}_{\mathrm{L}} = 0.01$) are shown in Fig. 6.2a, the frequency and wavenumber being normalized according to

$$\Omega = \frac{2b\omega}{c_{\mathrm{s}}\pi}, \tag{6.2}$$

$$\bar{\xi} = \frac{2b\xi}{\pi}, \tag{6.3}$$

(The mode labelling is justified later). Figure 6.2b shows the dispersion curves for the propagating modes of an elastic plate with the same bulk velocities as the attenuative plate but zero bulk attenuations. It can be observed that the two sets of
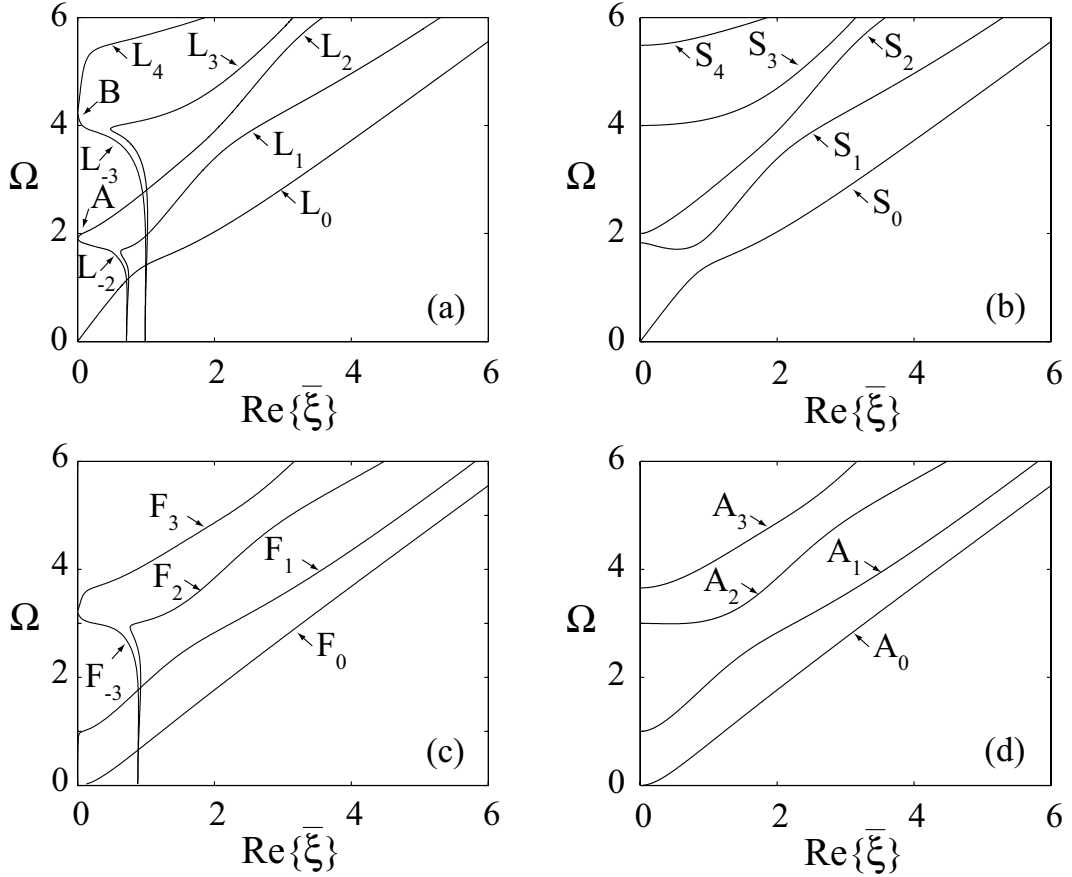
Figure 6.2: Real wave number dispersion curves; (a) attenuative symmetric modes; (b) elastic symmetric modes; (c) attenuative antisymmetric modes; (d) elastic antisymmetric modes.

dispersion curves are very similar except for the zones labelled A and B where the spectrum of the attenuative plate exhibits some extra branches. Moreover, some modes appear to join each other at infinite wavelength (see, for instance, L_2 and L_{-2}). The same considerations hold for the antisymmetric modes which are shown in Figs 6.2c,d for the attenuative and elastic plate, respectively. For this reason, in the following, only symmetric modes are considered.

The understanding of the topology of the dispersion curves can only be gained by considering the dispersion of both the real and imaginary parts of the wavenumber. This leads to a three-dimensional representation of the dispersion loci in the space $(Im\{\bar{\xi}\}, Re\{\bar{\xi}\}, \Omega)$. Figure 6.3c shows such a representation for the modes L_1, L_2, L_{-1} and L_{-2}. Figures 6.3a,b,d are the projections of the mode trajectories over the
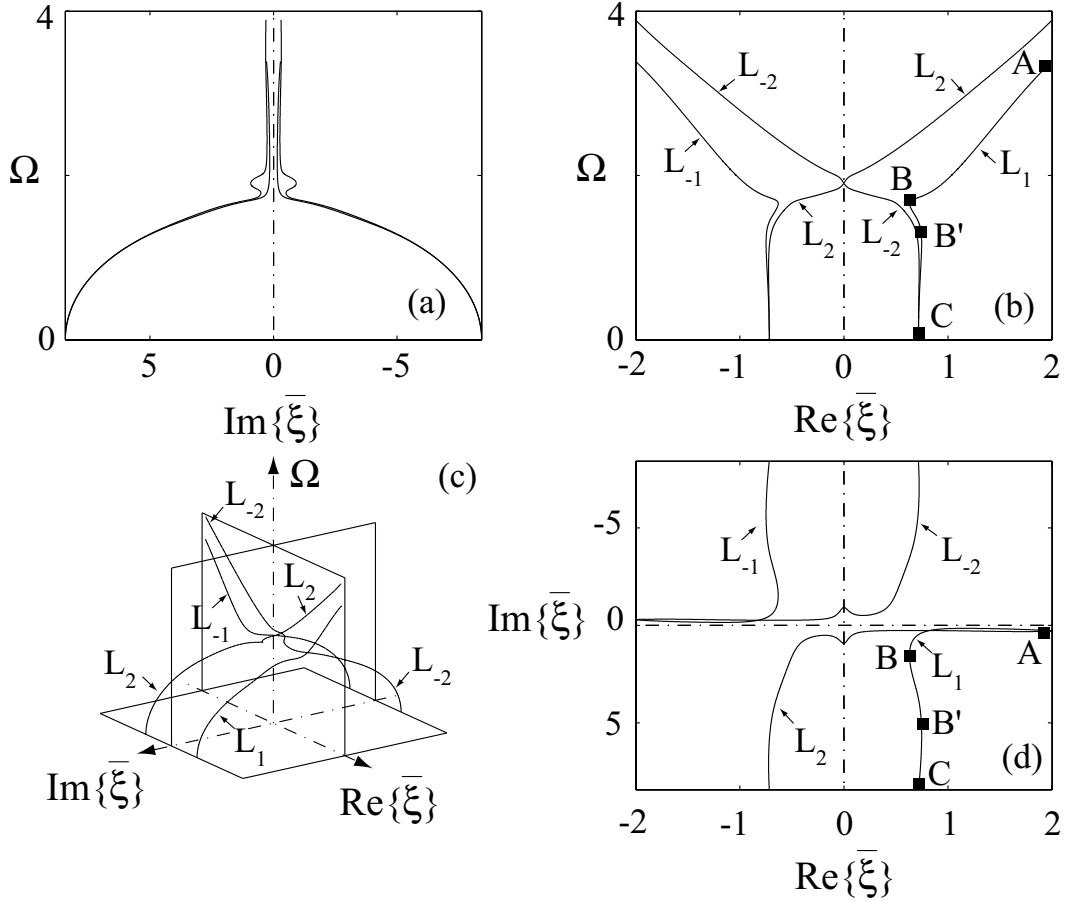
Figure 6.3: Three dimensional dispersion curves for the lossy plate (c) and projections over the planes: (a) $Re\{\bar{\bar{\xi}}\} = 0$; (b) $Im\{\bar{\bar{\xi}}\} = 0$; (d) $\Omega = 0$.

planes $Re\{\bar{\bar{\xi}}\} = 0$, $Im\{\bar{\bar{\xi}}\} = 0$ and $\Omega = 0$, respectively.

Consider the trajectory of the L_1 mode. For large values of the frequency (branch AB Fig. 6.3d), $Re\{\bar{\bar{\xi}}\}$ is dominant with respect to $Im\{\bar{\bar{\xi}}\}$. However, as the frequency decreases, $Im\{\bar{\bar{\xi}}\}$ becomes significant (branch B'C). More interesting is the slope of the function $\Omega(Re\{\bar{\bar{\xi}}\})$ which is negative along the branch BB' at whose edges the derivative $d\Omega/dRe\{\bar{\bar{\xi}}\}$ is singular (Fig. 6.3b). As a consequence, a question arises: is this derivative representative of the group velocity? It can be observed that the original conception of group velocity, introduced by Rayleigh [57], is to predict the speed of a wave packet whose harmonic components travel at different speeds. Such a velocity for a conservative system can be related to the wavenumber, k, according

to

$$V_{gr} = \frac{d\omega}{dk}. \tag{6.4}$$

Note that the wavenumber is real since the system is conservative. A natural, but not necessarily correct, way of defining the group velocity for propagation in lossy media, is to consider the real part of the wavenumber i.e.

$$V_{gr} = \frac{d\omega}{dRe\{k\}}. \tag{6.5}$$

Such a definition, for the attenuative plate, would lead to both negative (branch BB') and supersonic (higher than the material longitudinal velocity) group velocities around the point B and B' of the L_1 mode. Studies on the propagation of electromagnetic waves have shown that the definition (6.5) leads to "abnormal" velocities when the material absorbtion is taken into account, as in any medium there would be frequencies where the group velocity is superluminal, infinite or negative [58]. The debate on whether these abnormal cases are unphysical [59, 60, 61] or not [62, 63] is still open. In the acoustic field, there has been little work on this subject and at present there is no theoretical evidence which suggests a correct and sensible definition of the velocity of a wave packet. However, a possibility is to consider the velocity of energy transport which is defined as the power flow to mechanical energy density ratio. While for a conservative system, group velocity and velocity of energy transport are coincident [64], when material absorbtion is taken into account, the two velocities differ. In particular, Bernard et al. [44] showed experimentally for the L_3 mode that where a group velocity singularity occurs the velocity of the wave packet tends to the velocity of energy transport rather than the group velocity. Moreover, the sign of the velocity of energy transport characterises the modes since it is an invariant for each of them. This can be proved by observing that the propagation direction of a mode has to be constant along the mode path. If there was a propagation inversion, either a frequency where the power flow is zero or discontinuous would exist. However, a zero power flow frequency is not possible as a mode is always propagating. On the other hand, a discontinuous change in the power flow would imply that at the frequency where the discontinuity occurs the mode propagates in both directions $(\pm \hat{x}_1)$ which is unphysical. As a result, for one mode, it can be concluded that the velocity of energy transport sign has to be
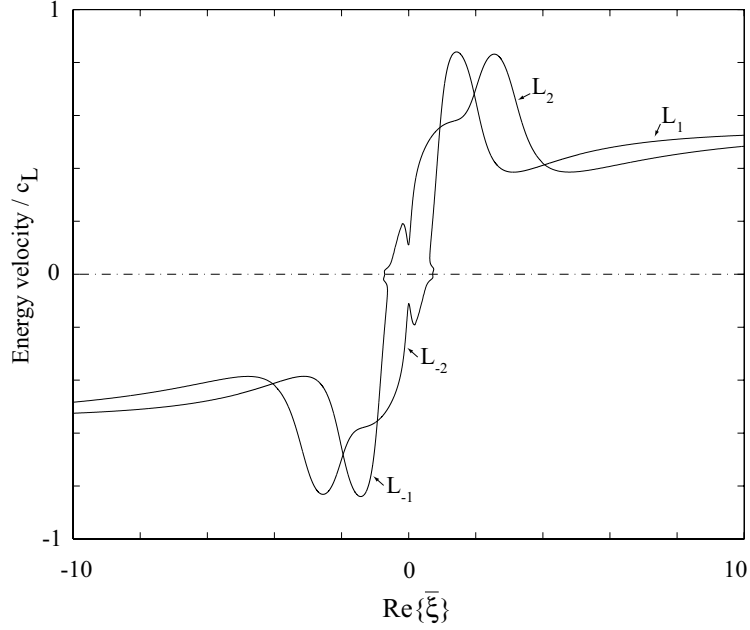
Figure 6.4: Velocity of energy transport versus real wavenumber.

constant with frequency. It has to be emphasized that at a given frequency the same perturbation can propagate in the positive or negative direction, which is confirmed by the fact that only the square of the wavenumber is involved in eq. (6.1). Therefore, the roots ξ and $-\xi$ must equally be solutions to eq. (6.1). However, in the space $(Im\{\bar{\xi}\}, Re\{\bar{\xi}\}, \Omega)$, these roots lay over different paths. As an example, in Fig. 6.3d L_1 corresponds to a mode propagating along $\hat{x}_1$ while L_{-1} represents the same type of vibration propagating in the opposite direction as can be deduced from the signs of the velocity of energy transport shown in Fig. 6.4, this justifies the negative subscript of some modes. Note that the velocity of energy transport is always subsonic.

While for L_1 the real part of the wavenumber is always positive, as the frequency decreases, the L_2 mode crosses the plane $Re\{\bar{\xi}\} = 0$ (Fig. 6.3b,d). At the frequency where the intersection occurs, the wavelength is infinite, but in contrast with the cutoff modes of an elastic plate, the mode still carries energy along $\hat{x}_1$. At this frequency, the real part of the wavenumber associated with each bulk wave is parallel to $\hat{x}_3$ ($\mathbf{n} \parallel \hat{\mathbf{x}}_3$) whereas the angle between the vector $\mathbf{b}$ and $\hat{x}_3$ is non zero. As explained in Chapter 2, the direction of the Poynting vector is always between $\mathbf{n}$ and

b; therefore, the component of the Poynting vector along $\hat{x}_1$ generates the in-plane power flow.

As the frequency decreases further, $Re\{\bar{\xi}\}$ becomes negative while $Im\{\bar{\xi}\}$ is still positive. Since the velocity of energy transport is always positive (Fig. 6.4), the mode still propagates in the direction $\hat{x}_1$. However, when $Re\{\bar{\xi}\} < 0$ the power flow is in the opposite direction to the phase velocity. This type of propagation is known as backward-wave motion and was first theoretically predicted by Tolstoy et al. [65] and experimentally observed by Meitzler [66] and Wolf et al. [67] for elastic plates and cylinders.

6.4   Attenuative versus elastic plate

The understanding of the topology of the dispersion curves of an attenuative plate, provides a clear picture of the structure of the dispersion curves of the elastic case.

Figure 6.5 shows how the dispersion curves of Fig. 6.3 transform as the material damping vanishes. Consider the S_1 mode as the frequency goes to zero. Along the branch AB the mode is propagating along $\hat{x}_1$ and its trajectory is entirely contained in the plane $Im\{\bar{\xi}\} = 0$. At point B, the mode breaks into three more branches, BC, BD and BE. Along the branches BC and BD the mode is nonpropagating, while along BE the group velocity is negative. However, among these branches only BC belongs to S_1. Mindlin clarified that the branch BE is not part of S_1 on the basis of the negativity of the group velocity (hence, of the power flow). However, it is not clear why the branch BC has to belong to S_1 rather than BD or even being a different mode. It is usually argued that a non propagating mode is a vibration which does not propagate and decays from the source. As a consequence, if the S_1 mode propagates in the $\hat{x}_1$ direction, the nonpropagating mode which decays in the same direction (branch BC), is associated to it. In these terms, this would be a mere convention which does not provide a valid motivation for considering the branch BC as a part of S_1 rather than an independent mode.
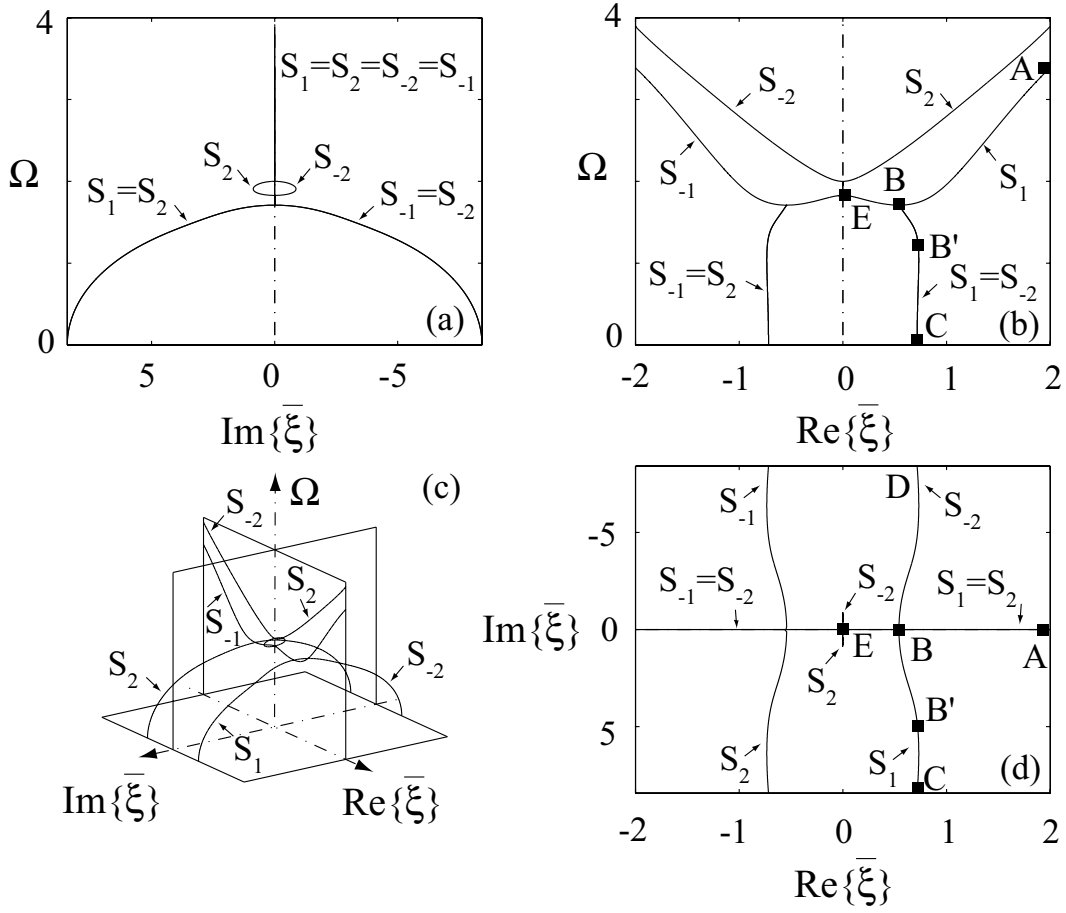
Figure 6.5: Three dimensional dispersion curves for the elastic plate (c) and projections over the planes: (a) $Re\{\bar{\xi}\} = 0$; (b) $Im\{\bar{\xi}\} = 0$; (d) $\Omega = 0$.

The physical reason why the branch BC has to belong to the S_1 mode lies in the dispersion curves of the attenuative plate. Since the trajectories of the attenuative plate modes tend to those of the elastic case as the material damping vanishes (see limiting absorption principle [68]), it follows that for very low material damping the modes of the attenuative plate mark the trajectories of the elastic plate. For instance, the L_1 mode tends to embrace the branches AB and BC (compare Fig. 6.3d and Fig. 6.5d). Therefore, it can be concluded that since the two branches AB and BC of the elastic plate correspond to the limit toward which the trajectory of only one mode (L_1) tends, they belong to the same mode indeed. In a similar fashion, the branches BD and BE belong to the S_{-2} mode since the L_{-2} mode tends to them as the absorbtion vanishes (compare Fig. 6.3d and Fig. 6.5d). Moreover, a nonprop-

agating mode decays along the propagation direction of the corresponding mode of the attenuative plate. This discussion suggests that it would be more appropriate to refer to the nonpropagating branch of a mode rather than to a nonpropagating mode.

It is worthwhile to notice that for a mode of the attenuative plate the branch which approaches the non propagating branch of the corresponding elastic mode is characterised by large guided wave attenuation ($Im\{\xi\}$). As a consequence, the L_1 mode at very low frequency is rapidly attenuated with distance, and from a practical point of view behaves as a nonpropagating mode. This consideration holds for the other higher order modes in the regions where they approach the elastic nonpropagating mode branches.

6.5   Lamb waves in bilayered plates

The intimate link between propagating and nonpropagating branches explains the anomalies in the dispersion curves discussed in Sections 4.6 and 4.7.

Figure 6.6 is the spectrum of the first five Lamb modes of the bilayer studied in Sec. 4.6. For simplicity only the curves with positive $Re\{\bar{\xi}\}$ have been represented. Solid lines refer to modes propagating along the $\hat{x}_1$ direction, while the dashed line represent a backward mode. On the other hand, Fig. 6.7 shows the dispersion loci when the material absorbtion in the viscoelastic layer is neglected. In this case all the propagating modes lie on the plane $Im\{\bar{\xi}\} = 0$. Note that the only nonpropagating branches are AD, AD', and the loops CB, GF and EO.

While the trajectories of M_0 and M_1 are quite similar to those of $\bar{M}_0$ and $\bar{M}_1$, the paths of the other modes exhibit significant changes. In particular, the modes of the elastic bilayer are all connected through complex branches, whereas the modes of the attenuative bilayer are well separated. As in the case of a free plate, the mode paths of the elastic bilayer can be thought of as the limit condition toward which the modes of the attenuative bilayer tend as the material attenuation goes to zero.
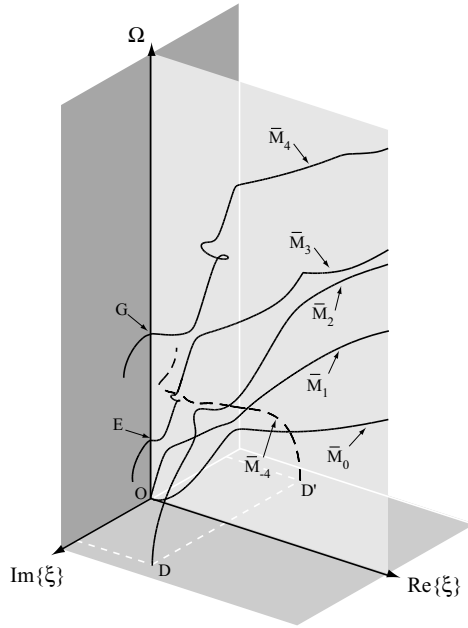
Figure 6.6: Three dimensional Lamb wave dispersion curves for the bilayer described in tab. 4.1 with $k_S = k_L = 0.01np/wl$.
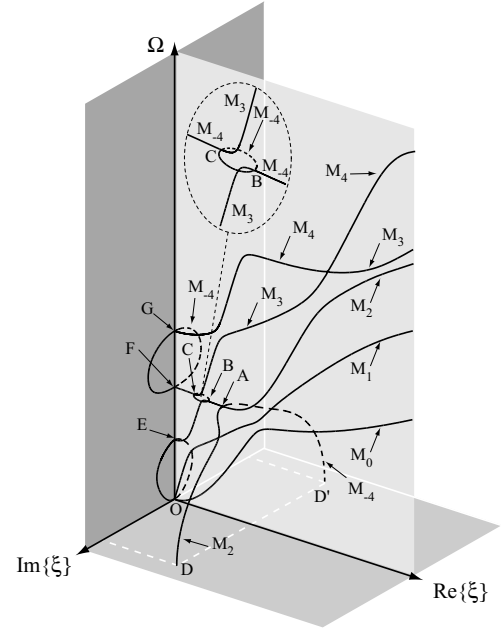
Figure 6.7: Three dimensional dispersion curves for the equivalent elastic bilayer of tab. 4.1.

An interesting feature of the dispersion loci of the elastic bilayer is the presence of a complex loop with diameter BC one half of which belongs to the mode M_3 (space $Im\{\bar{\xi}\} > 0$, solid line) and the other half to M_{-4} (space $Im\{\bar{\xi}\} < 0$, dashed line) as depicted in the zoom at the top of Fig. 6.7. This loop causes the M_3 mode to split into two different branches in the phase velocity versus frequency plane shown in Fig. 6.8a. The apparent separation is due to the fact that the half loop belonging to M_3 is not visible since it is nonpropagating. However, as the attenuation in the viscoelastic layer is considered, the loop becomes propagating and the two branches join together Fig. 6.8b. Moreover, due to the shape of the loop, a maximum in the guided wave attenuation, $Im\{\xi\}$, occurs. Also the branch AD of M_2 and the branches CB, BA and AD' of M_{-4} (Fig. 6.7) appear in the phase velocity dispersion curves as soon as the material absorbtion is taken into account Fig. 6.8b. Note that the dispersion curves shown in this figure are the same as those shown in Fig. 4.7; however, the mode labelling is now more rigorous.
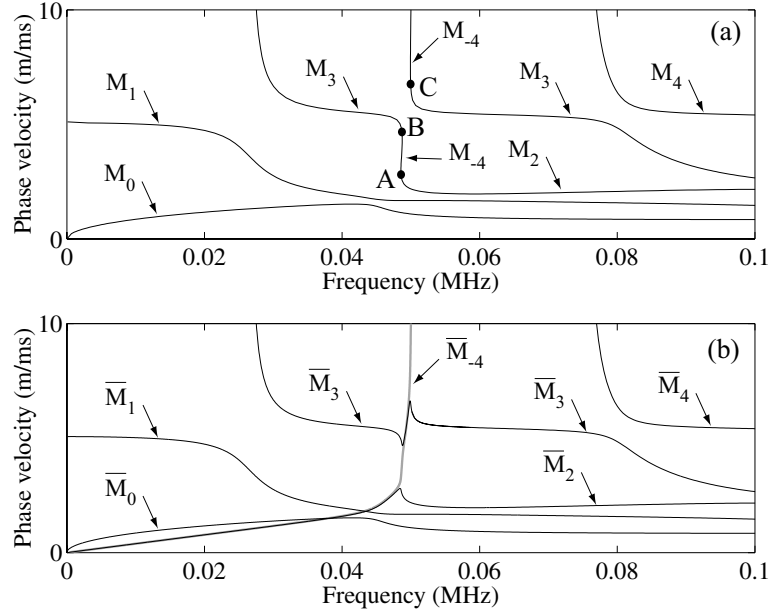
Figure 6.8: Lamb wave phase velocity dispersion curves for the bilayer described in tab. 4.1: (a) elastic case; (b) $k_S = k_L = 0.01np/wl$.

6.6 Summary

The nature of the nonpropagating modes of an elastic plate has been investigated by considering the elastic case as a restriction of the more general viscoelastic problem. It has been emphasized that the existence of nonpropagating branches in the dispersion curves of an elastic plate is due to the elastic hypothesis. In other words, once energy absorbtion within the material is considered, nonpropagating branches begin to carry energy and become a continuous extension of the original elastic propagating mode. As a consequence, a nonpropagating mode should be regarded as a mode branch which jointly with one or more propagating branches forms a mode, rather than a mode itself.

It has been shown that the low frequency anomalous branches in Fig. 4.7, and the negative attenuation of $\bar{M}_{-4}$ are due to the complex branches of the modes of the elastic bilayer. Moreover, the presence of a complex loop (BC) in the dispersion curves of the elastic bilayer causes the attenuation maximum of the $\bar{M}_3$ mode. Such a maximum, in the case of large material damping, corresponds to the second attenuation peak of the $\bar{M}_1$ mode.

Chapter 7

Characterisation of fluid viscoelastic materials

7.1 Background

As has been shown in the previous Chapters, the dispersion characteristics of guided waves propagating in coated pipelines are strongly dependent on the shear acoustic properties of the coating which need to be characterised in order to assess the feasibility of long range inspections.

For this purpose several techniques are available. Reflectometry, for example, uses the successive echoes from both the front and the back faces of a sample rigidly bonded to a delay line, the amount of the reflected energy and its phase being dependent on the sample impedance [69, 70]. However, although the method is relatively easy to carry out, the measurement of the reflected signal is affected by several factors, including beam spreading, transducer coupling, and magnification of bias and variance errors in the time trace of the consecutive echoes emitted from the back of the specimen [71]. This problem can be overcome by considering the front reflection from the delay line-sample interface only. However, since the front reflection is almost insensitive to the material attenuation in the sample, only the bulk velocity can be measured. Transmission methods [72, 73], are affected by the same limitations as reflectometry. However, an improvement in the signal loss is achieved as the signals have to travel only once through the thickness. The ampli-

tude spectrum method [74, 75] and the phase spectrum method [76] are often used as signal processing methods. They do not significantly change the basic limitations.

The use of guided waves is an extremely attractive alternative to solve many of the problems mentioned above. Horizontal shear waves in strips [77] or torsional waves in rods submerged in a Newtonian liquid of known density have been employed to measure the viscosity of the liquid [78, 79]. The viscosity can be obtained by measuring the guided wave attenuation since, at a given frequency, there is a unique relationship between the guided wave attenuation and the viscosity. The method is extremely rapid and ideal for measurement on line and in real time. On the other hand, these techniques cannot be used for viscoelastic materials as the elasticity and the damping of the material cannot be linked uniquely to the guided wave attenuation. In other words, the link between the guided wave attenuation and the two acoustic properties (sound velocity and bulk attenuation) provides one equation only, which does not allow the two unknown acoustic properties to be found.

In the case of a rod embedded in an other medium, the phase velocity of guided waves in the rod is only very weakly dependent on the properties of the second medium (unless the two media are similar). However, with other geometries, the phase velocity in the waveguide is sensitive to the properties of the second medium.

In this Chapter, the possibility of deriving the viscoelastic properties from the dispersion characteristics of guided waves propagating in a hollow cylindrical waveguide filled with the unknown viscoelastic material is considered. The first important feature of this approach is that the guided wave attenuation is only a consequence of the material damping within the inner core. If the core was perfectly elastic no guided wave attenuation would occur (assuming the waveguide to be elastic), in contrast with the case of a rod embedded in an elastic space [31]. By contrast with conventional methods, a full control of the magnitude of the guided wave attenuation can be achieved by varying the geometry (radius and wall thickness) and acoustic properties of the tube. In particular, the physics behind the attenuation mechanism of guided waves propagating in filled tubes is the same as in the case of SH waves

propagating in absorbing bilayers, when a correspondence between the tube and the metallic plate and the inner core and the attenuative coating is set.

The method proposed in this Chapter provides excellent geometry control, since the waveguide works as a mould. As laser interferometry can be used for the detection of the propagating modes, transducer coupling problems can be avoided.

The viscoelastic material is modelled by considering the linear viscoelastic approach discussed in Chapter 2. Moreover, no assumptions about the frequency dependence of the acoustic properties such as Kelvin-Voigt, Maxwell or Newtonian models are made. The technique to obtain the acoustic properties of the viscoelastic core is explained in Sec. 7.3. Bitumen properties (Sec. 7.5) have been measured by employing the setup described in Sec. 7.4.

7.2   Torsional modes

Let us consider a hollow, elastic and isotropic cylinder filled with the unknown viscoelastic material. The geometry of the system suggests that cylindrical coordinates (r,θ,z) are appropriate here (r,θ,z, represent the radial, angular and axial positions respectively).

The tensorial nature of eqs (2.12) and (2.13) implies that these equations hold regardless of the coordinate system. In particular, as in the case of shear bulk waves, torsional waves correspond to the solutions to eq. (2.13). In this case the vector potential $\mathbf{H}$ is parallel to $\hat{\mathbf{z}}$ and is provided by

$$\mathbf{H} = [A_0 J_0(k_{\hat{r}}r) + B_0 Y_0(k_{\hat{r}}r)]e^{-\zeta z}e^{-i\Upsilon z}\hat{\mathbf{z}}, \tag{7.1}$$

where A_0 and B_0 are arbitrary constants, $k_{\hat{r}}$ and $\Upsilon - i\zeta$ are the projections of the complex wavenumber vector $\mathbf{k}_\mathrm{s}$ along $\hat{\mathbf{r}}$ and $\hat{\mathbf{z}}$ respectively, $\mathbf{k}_\mathrm{s}$ being solution to the characteristic equation (2.20). J_0 and Y_0 are the Bessel functions of the first and second kind. Note that the vector potential is no longer equivoluminal as addressed

Table 7.1: Material bulk properties and geometry.

Material	c_s (m/ms)	$\bar{\alpha}_s$ (np/wl)	ρ (kg/m^3)	Thickness/radius (mm)
Copper tube	2.24	0.00	8900	0.70
Inner core	0.43	1.35	970	6.80

by Gazis [80]. The displacement field can be obtained by applying the curl operator to **H**, thus

$$u_\theta = [A_1 J_1(k_{\hat{r}}r) + B_1 Y_1(k_{\hat{r}}r)]e^{-\zeta z}e^{-i\Upsilon z}, \qquad (7.2)$$

where $A_1 = -A_0 k_{\hat{r}}$ and $B_1 = -B_0 k_{\hat{r}}$, the displacement field being tangential. By considering the compatibility equations (2.2) and the constitutive equations (2.7) in cylindrical coordinates, the non zero components of the stress tensor are

$$\tau_{r\theta} = \tilde{\mu}\left(\frac{\partial u_\theta}{\partial r} - \frac{u_\theta}{r}\right), \qquad (7.3)$$

$$\tau_{z\theta} = \tilde{\mu}\frac{\partial u_\theta}{\partial z}. \qquad (7.4)$$

$$(7.5)$$

The displacement field associated with a torsional mode propagating in a filled tube can be expressed according to (7.2) where the constants A_1 and B_1 are different in the wall tube and in the inner core. This would lead to four unknown constants. However, it can be observed that inside the core, the constant B_1 has to vanish since the function Y_1 is singular for $r = 0$. As a consequence, the characteristic equation can be found by imposing the continuity of the displacement and the stress component $\tau_{r\theta}$ at the interface core-tube and the zero traction condition at the free surface of the tube, in agreement with the partial wave technique already employed in Chapters 3 and 4.

The topology of the dispersion curves of torsional modes propagating in a filled tube exhibits the same characteristics as SH waves propagating in layered plates. Fig. 7.1 shows the dispersion curves for torsional modes travelling in the filled tube described in Tab. 7.1 when the bulk attenuation of the core is neglected (the curves have been calculated with the software Disperse). As in the case of SH waves, the
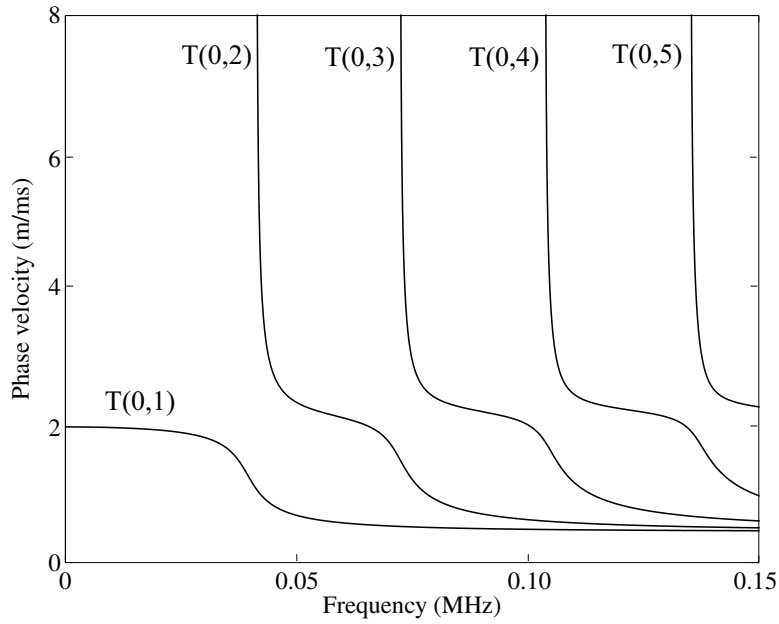
Figure 7.1: Phase velocity dispersion curves for the filled tube when the bulk attenuation is neglected (material properties Tab. 7.1).

filled tube modes originate from the interaction between the torsional modes of the empty tube (which correspond to the first family of asymptotic modes studied in Chapter 3) and the torsional modes of the inner core if it were rigidly clamped at the interface with the tube (second asymptotic family). In particular, the dispersion curves shown in Fig. 7.1 are due to the interaction of the fundamental torsional mode of the empty tube with the first four modes of the clamped core.

The displacement field of the fundamental mode of the empty tube, $T^t(0,1)$, is

$$u_\theta = Bre^{-i\frac{\omega}{c_t}z}, \tag{7.6}$$

where c_t is the shear velocity of the tube. Note that the phase velocity coincides with the bulk shear velocity of the tube, Fig 7.2.

The modes of the clamped core can be obtained by imposing the zero displacement condition at the core-tube interface. This leads to the following characteristic equation [see eq. (7.2)]

$$J_1(k_{\hat{r}}r_0) = 0, \tag{7.7}$$
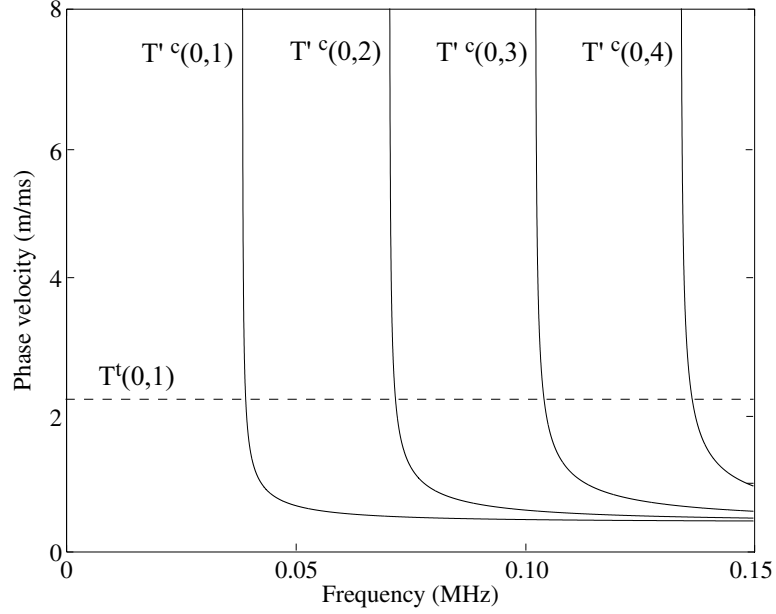
Figure 7.2: Asymptotic modes for the filled tube:$(---)$ empty tube; ($\longrightarrow$) clamped core.

where r_0 is the core radius and the wavenumber component $k_{\hat{r}}$ satisfies the condition

$$k_{\hat{r}}^2 + \Upsilon^2 = \frac{\omega^2}{c_c^2},$$ (7.8)

where c_c is the core shear velocity. The solutions to (7.7) are [81]

$$\frac{k_{\hat{r}} r_0}{\pi} = \quad 0, \quad 1.2196, \quad 2.2332, \quad 3.2384, \quad 4.2410, \dots, \psi_N,$$ (7.9)

where ψ_N represents the Nth solution. The first solution is trivial as it corresponds to zero displacement over the cross section of the core. On the other hand, the phase velocity spectrum associated with the Nth order mode, $T'^c(0, N)$, is given by

$$\frac{f^2}{c_c^2} - \frac{f^2}{c_{ph}^2} = \left(\frac{\psi_N}{2r_0}\right)^2,$$ (7.10)

the dispersion curves of the first four modes being shown in Fig. 7.2. As the mode order increases, ψ_N tends to N and the phase velocity dispersion curves of torsional modes propagating in the clamped core tend to the dispersion curves of SH waves propagating in a free plate with thickness r_0 [see eq. (3.26)]. Moreover, from (7.10) the cutoff frequencies of the clamped core are

$$f_{cutoff} = \frac{c_c \psi_N}{2r_0}.$$ (7.11)
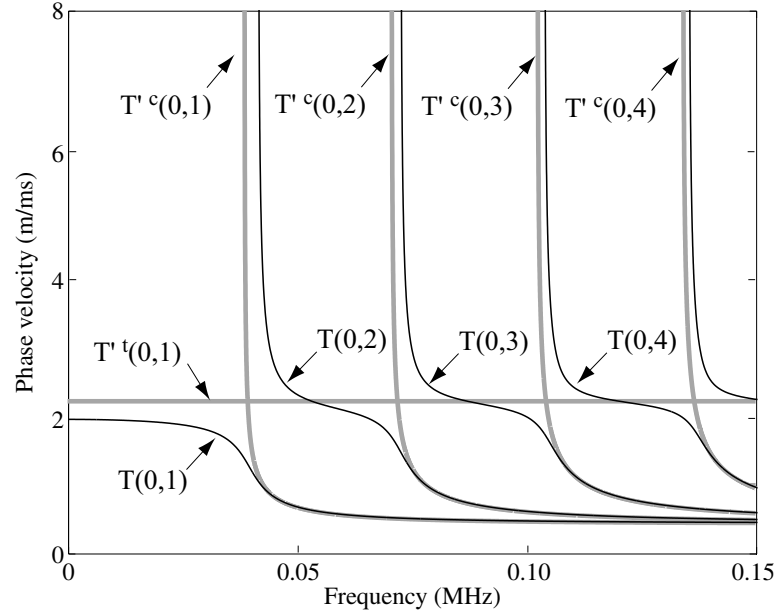
Figure 7.3: Dispersion curves of the asymptotic modes (━━━) and the modes of the filled tube (━━━).

Figure 7.3 is the superposition of the asymptotic modes and the modes of the filled tube. As in the case of SH waves, torsional modes undergo the mode jumping phenomenon (Sec. 3.6) which, as the frequency varies, is accompanied by energy migration from the tube wall into the core and vice versa. In particular, at the cutoff frequencies of the filled tube modes, due to the large impedance difference between the core and the tube, the modes correspond to standing waves in the core (7.11), while there is very little motion of the tube wall. However, as the frequency increases, the amount of energy which travels in the tube wall increases. At the frequencies where the modes intersect the $T^t(0,1)$ mode of the empty tube, most of the energy propagates in the tube rather than in the core. As the frequency increases further, the energy contained in the tube wall decreases, and for very high frequency the energy primarily travels in the core.
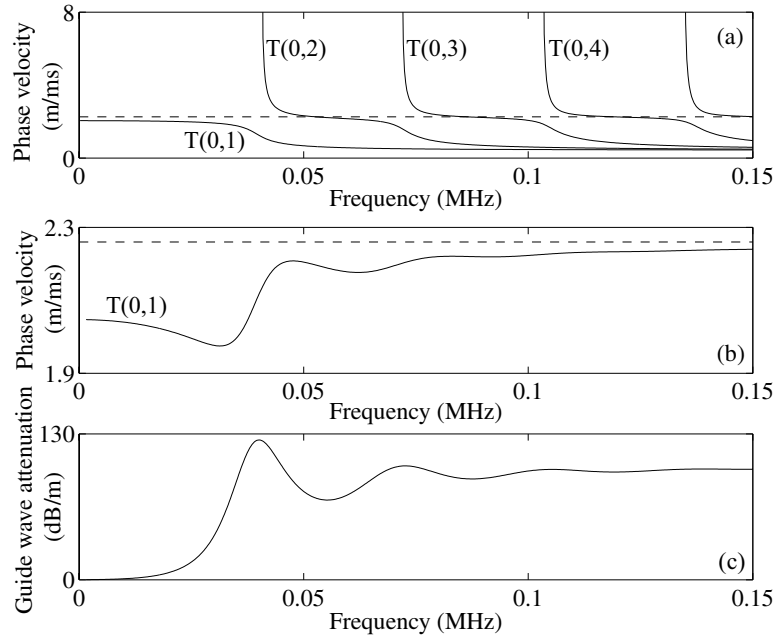
Figure 7.4: Dispersion curves for the system described in tab. 7.1: (a) Phase velocity of the filled tube when the bulk attenuation is neglected (solid line) and phase velocity of the empty tube (dashed line); (b) as (a) but with bulk attenuation in the core material; (c) guided wave attenuation corresponding to (b).

Fig. 7.4b,c show the phase velocity and guided wave attenuation for a viscoelastic core with constant bulk shear velocity and attenuation per wavelength while Fig. 7.4a corresponds to the elastic system (note the velocity scale in Fig. 7.4b is finer than that in Fig. 7.4a). Due to the large value of the material attenuation, the modes no longer jump and as the frequency increases, the $T(0,1)$ mode of the filled tube approaches the $T^t(0,1)$ mode of the empty tube rather than tending to the $T'^c(0,1)$ mode of the clamped core. All the other higher order modes of the filled tube tend to the modes of the clamped core which are highly attenuated (not shown here). Moreover, as for SH waves, the maxima of the attenuation spectrum occur at the frequencies where the modes would jump if the core were elastic [compare Figs (7.4)a and (7.4)c] as explained in Sec. 3.7.
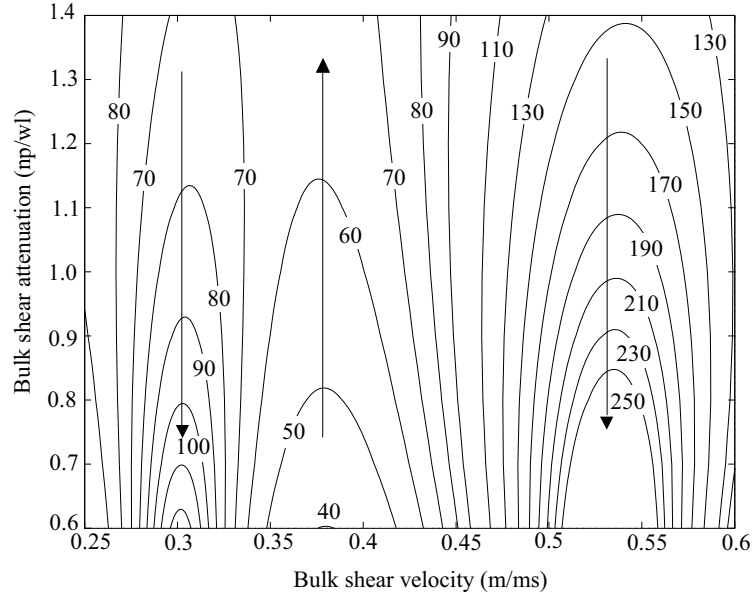
Figure 7.5: Contour plot of the guided wave attenuation (dB/m) as function of the bulk shear velocity and the bulk attenuation at $50kHz$ for a $6.8mm$ inner radius, $0.7mm$ wall thickness, filled copper tube. Core density $970kg/m^3$. The arrows indicate the direction of increasing attenuation.

7.3   Method

For a given frequency and assigned tube geometry and core density, the guided wave attenuation and phase velocity are functions of the bulk shear velocity and the bulk attenuation only. Fig. 7.5 shows the contour plot of the attenuation when all the parameters are kept constant except the acoustic properties of the inner core. Each curve corresponds to a value of ζ and provides all the values of $\bar{\alpha}_s$ and c_s which, at the prescribed frequency and geometry, result in the specified value of guided wave attenuation. In other words, each curve provides $\bar{\alpha}_s$ as a function of c_s and ζ

$$\bar{\alpha}_\mathrm{s} = g_1(c_\mathrm{s}, \zeta). \tag{7.12}$$

While all the couples ($\bar{\alpha}_s$, c_s) provided by (7.12) result in the same value of ζ, they do not result in the same value of the phase velocity. A second relationship can be obtained from the contour plot of the phase velocity (Fig. 7.6). It is possible to obtain a function that, for a given value of the phase velocity, links $\bar{\alpha}_\mathrm{s}$ to c_s and c_{ph}

$$\bar{\alpha}_\mathrm{s} = g_2(c_\mathrm{s}, c_{ph}). \tag{7.13}$$
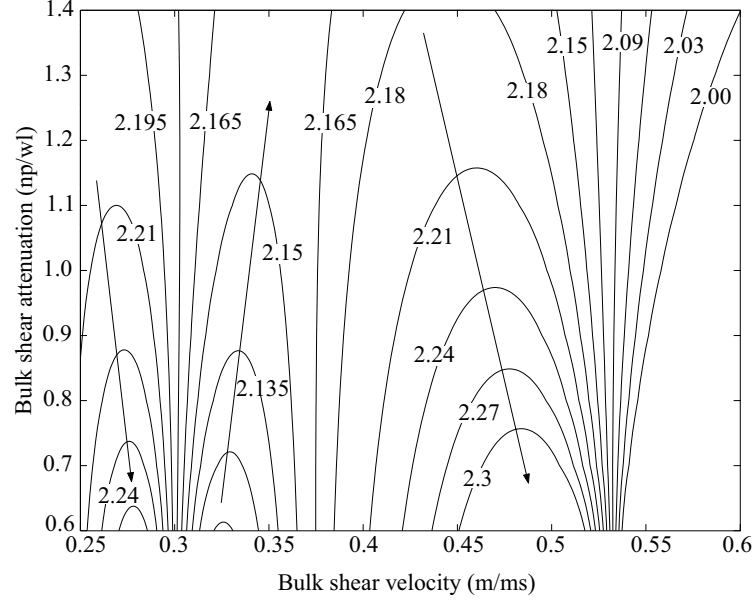
Figure 7.6: Contour plot of the phase velocity (m/ms) as function of the bulk shear velocity and the bulk attenuation at $50kHz$ for a $6.8mm$ inner radius, $0.7mm$ wall thickness, filled copper tube. Core density $970kg/m^3$. The arrows indicate the direction of increasing phase velocity.

In this case all the couples ($\bar{\alpha}_s$, c_s) give the same phase velocity but different guided wave attenuation. At a given frequency, f_0, the phase velocity, c_{ph0}, and the guided wave attenuation, ζ_0, can be measured experimentally. As a consequence, the curve $g_1(c_s, \zeta_0)$ of the guided wave contour plot and the curve $g_2(c_s, c_{ph0})$ of the phase velocity contour plot are known. By overlapping the two curves, the intersection provides the bulk acoustic properties $\bar{\alpha}_s$ and c_s of the viscoelastic material at the prescribed frequency, f_0. This comes from the fact that at the intersection, $\bar{\alpha}_s$ and c_s result in the measured value of the guided wave attenuation, ζ_0, as the intersection point belongs to $g_1(c_s, \zeta_0)$, and in the measured value, c_{ph0}, of the phase velocity as the intersection point belongs to $g_2(c_s, c_{ph0})$. Since the previous procedure can be applied to any frequency, it follows that the dispersion curves of the viscoelastic material [$\bar{\alpha}_s(f)$ and $c_s(f)$] can be determined over the frequency range of interest. Moreover, by contrast with other techniques [82, 83], no assumptions are made about the frequency dependence of the acoustic properties, as the method considers each frequency separately.
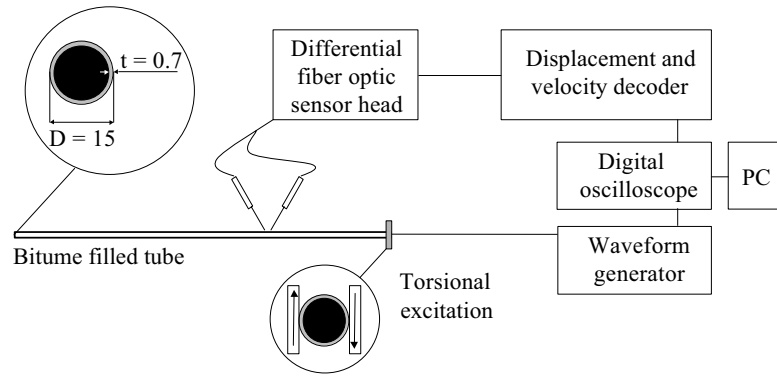
Figure 7.7: Schematic diagram of the setup.

7.4 Experiments

The experiments were performed at the temperature of $298K$ on a $1m$ length copper tube (internal radius $6.8mm$, wall thickness $0.7mm$) filled with bitumen TML 24515 45/60 supplied by Shell Global Solutions. The torsional mode was excited by means of two piezoelectric transducers clamped to the external surface of the tube at one end as shown in Fig. 7.7. The transducers which are similar to those used in pipe testing [17] comprised shear elements mounted on a steel backing mass and oriented as shown in Fig. 7.7 to induce torsion. The transducers were excited by a Hanning windowed toneburst generated by a custom-made waveform generator-power amplifier. The torsional mode was detected by a laser interferometer (Sensor Head: Polytec OFV 512, Controller: Polytec OFV 3001) operating in differential mode. The tangential displacements were measured by focusing the two beams at $\pm 30^0$ with respect to the radial direction and by orienting the beams in the plane perpendicular to the axis of the tube. The displacements were sampled along the tube axis and stored in a PC after 100 averages.

In order to measure the properties of the unknown material over a wide range of frequencies, a relatively wide band signal with a number of cycles ranging from 3, for low frequencies, up to 5 for the higher frequencies was excited. More cycles are needed at higher frequencies since the attenuation tends to be higher and the use of more cycles improves the signal-noise ratio and reduces the effects of dispersion.

In order to obtain the dispersion curves, one can observe that for a propagating mode the Fourier transform of the signal at an arbitrary position, z, can be expressed as a function of the Fourier transform at the origin $z = 0$ multiplied by a suitable complex exponential

$$U(z, \omega) = U(0, \omega)e^{-\zeta z}e^{-i\frac{\omega}{c_{ph}}z}, \tag{7.14}$$

where the argument of the exponential is the projection of the complex wavenumber along the propagation direction. Furthermore, if the ratio R is defined as

$$R = \frac{U(z, \omega)}{U(0, \omega)}, \tag{7.15}$$

it follows that

$$\|R\| = e^{-\zeta z}, \tag{7.16}$$

$$\frac{R}{\|R\|} = e^{-i\frac{\omega}{c_{ph}}z} = \cos\left(\frac{\omega}{c_{ph}}z\right) - i\sin\left(\frac{\omega}{c_{ph}}z\right), \tag{7.17}$$

where $\| \cdot \|$ is the norm operator in the complex domain. Since the ratio R can be measured experimentally, the guided wave attenuation can be determined through a linear interpolation of the experimental, logarithmic distribution of $\|R\|$ versus the axial position. Such a distribution is shown in Fig. 7.8. The slope of the interpolation line gives the guided wave attenuation. Fig. 7.9 shows the distribution of the real part of the ratio $R/\|R\|$ against the axial position. The phase velocity is computed from a cosine interpolation of the experimental data. The argument of the cosine function, ω/c_{ph}, is obtained by minimizing the square root of the error between the experimental distribution and the cosine function. This approach is particularly robust as it does not require the inversion of the cosine function to determine the unknown argument ω/c_{ph} and the successive phase unwrapping procedure due to the periodicity of the cosine function [84].
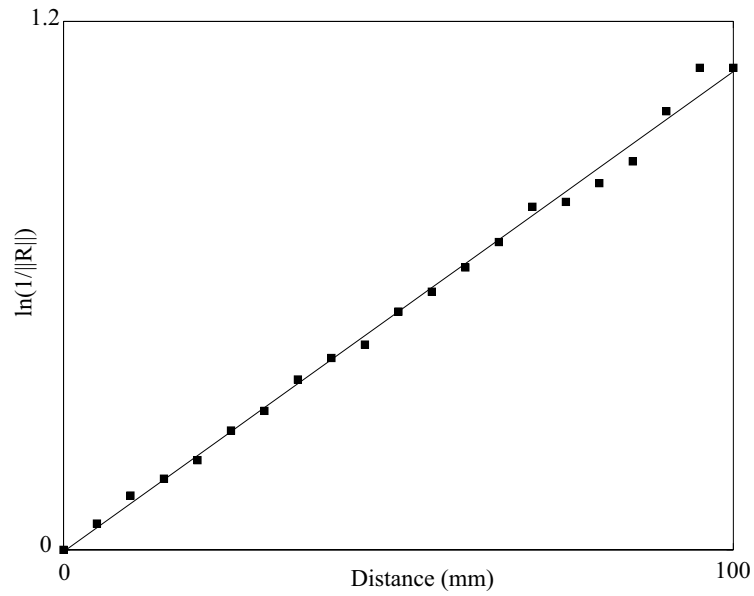
Figure 7.8: $ln\left(\frac{1}{\|R\|}\right)$ against the axial position z, at $50kHz$ for a $6.8mm$ inner radius, $0.7mm$ wall thickness, copper tube filled with bitumen: (■) experiments; (———) linear interpolation.
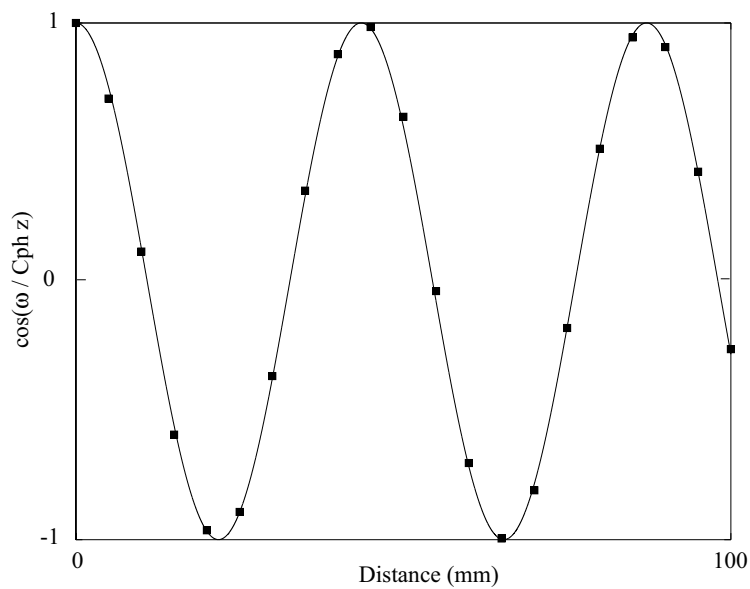
Figure 7.9: $\cos\left(\frac{\omega}{c_{ph}}z\right)$ against the axial position z, at $50kHz$ for a $6.8mm$ inner radius, $0.7mm$ wall thickness copper tube filled with bitumen: (■) experiments; (———) cosine interpolation.
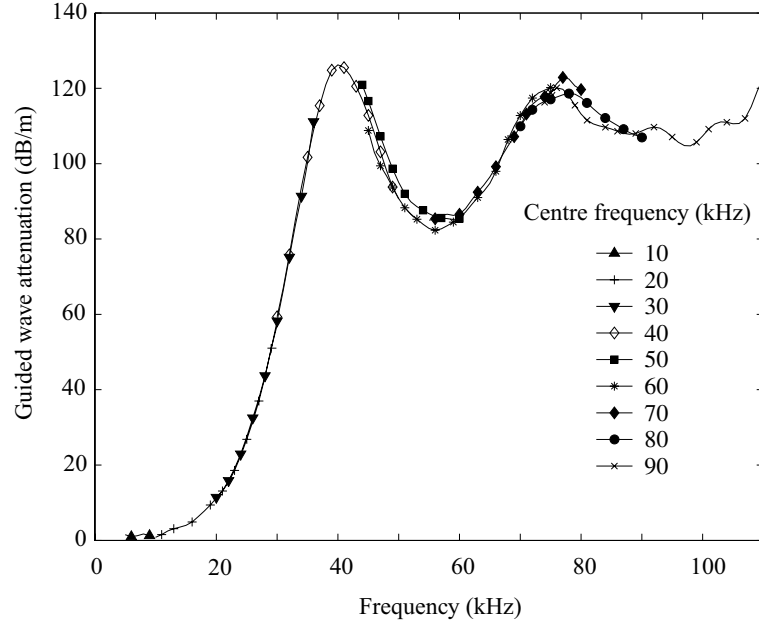
Figure 7.10: Experimental guided wave attenuation versus frequency for a $6.8mm$ inner radius, $0.7mm$ wall thickness copper tube filled with bitumen.

7.5   Bitumen dispersion curves

Here the procedure described in Sec. 7.4 is applied to the characterisation of the bitumen TML 24515 45/60 acoustic properties. For this type of bitumen the measured density was $970kg/m^3$.

Fig. 7.10 shows the measured guided wave attenuation as a function of frequency. The curve is obtained as a superposition of measurements performed at different centre frequencies and successively postprocessed according to the method described in the previous section. Fig. 7.11 shows the experimental phase velocity for the filled tube. The segments of the curves obtained at different centre frequencies overlap very well.

As an example, let us consider the frequency where the first attenuation peak occurs (i.e. $40kHz$, Fig. 7.10). At this frequency the guided wave attenuation is $127dB/m$ while the phase velocity is $2.093m/ms$ (Fig. 7.11). Fig. 7.12 shows the overlapping of the guided wave attenuation and phase velocity contour plots at $40kHz$. The intersection of the curve at constant attenuation ($\zeta = 127dB/m$) and the curve at
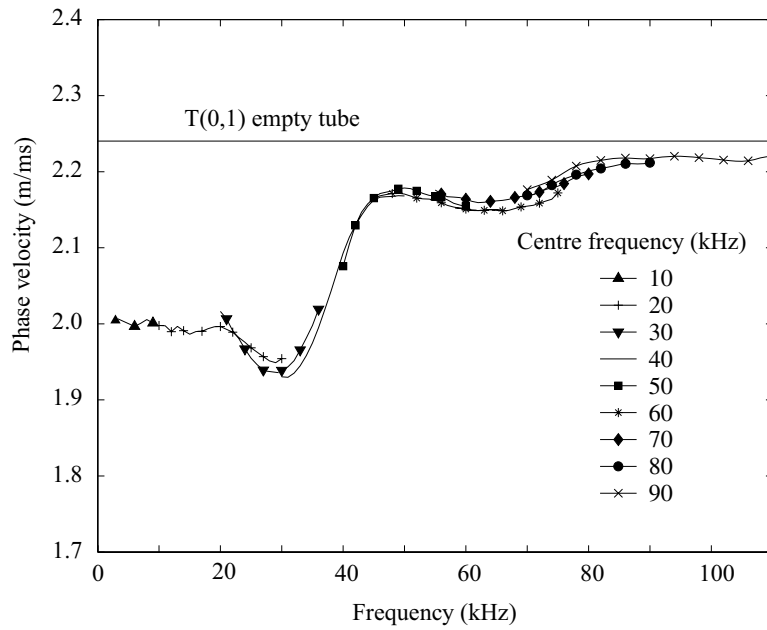
Figure 7.11: Experimental phase velocity versus frequency for a $6.8mm$ inner radius, $0.7mm$ wall thickness copper tube filled with bitumen.
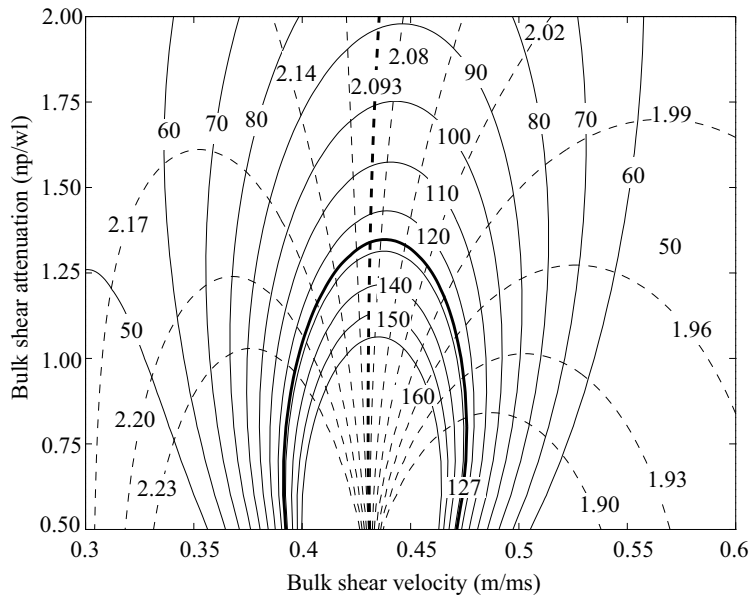
Figure 7.12: Contour plot for the guided wave attenuation (solid lines dB/m) and the phase velocity (dashed lines m/ms) calculated at $40kHz$ for a $6.8mm$ inner radius, $0.7mm$ wall thickness copper tube filled with bitumen (density $970kg/m^3$).
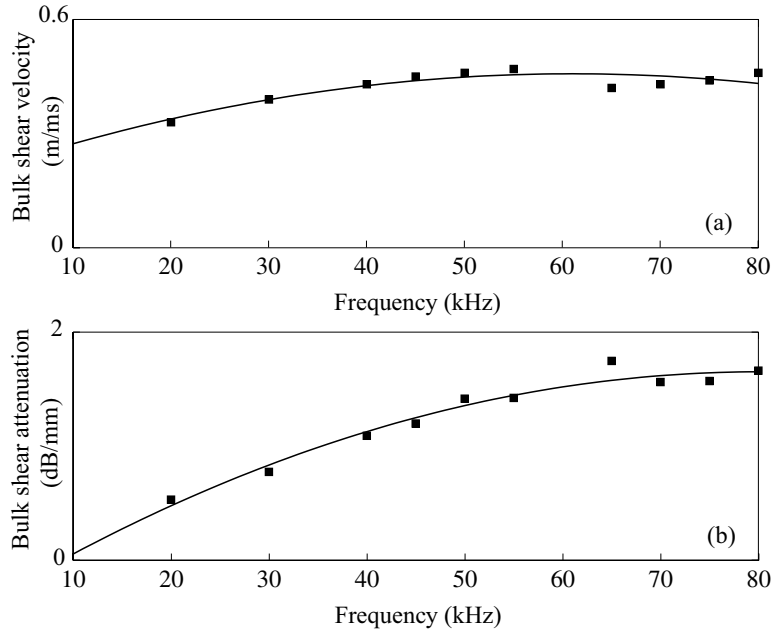
Figure 7.13: Dispersion curves for bitumen TML 24515 45/60: (a) bulk shear velocity against frequency; (b) bulk shear attenuation against frequency.

constant phase velocity ($c_{ph} = 2.093 m/ms$) provides the values of the shear velocity, $0.43 m/ms$, and the bulk attenuation, $1.35 np/wl$, of bitumen at $40 kHz$. It is interesting to note that the two curves intersect each other almost perpendicularly which implies that the method is numerically robust. The bitumen bulk shear velocity versus frequency is shown in Fig. 7.13 (a), and the bulk shear attenuation against frequency is shown in Fig. 7.13 (b). The curves have been derived by applying the former procedure to several frequencies (black squares). The trend lines (solid lines) have been obtained by best fitting second order polynomials. It has to be emphasized that a polynomial interpolation is not strictly representative of the behaviour of a viscoelastic material as it cannot account for the transition between the material rubbery and glassy behaviour. More suitable mathematical expressions are provided by Hartmann et *al.* [85] who show how the Havriliak-Negami model can accurately describe the trend of both modulus and loss factor of a polymer over the entire frequency range. According to the Havriliak-Negami model the complex modulus is given by

$$\tilde{\mu} = \mu_\infty + \frac{\mu_\infty - \mu_0}{(1 + (if/f_0)^\alpha)^\beta}, \tag{7.18}$$

where μ_0 and μ_∞ are the limiting rubbery and glassy moduli, f_0 is the frequency where the transition occurs and α and β are two constants. However, at the low frequencies considered here, due to the large value of f_0 (typically $2MHz$), the real part of $\tilde{\mu}$ is almost constant with frequency, while the imaginary part varies linearly with frequency since the ratio f/f_0 is very low. This suggests that a polynomial interpolation, at low frequencies, should be able to describe with an acceptable level of accuracy the material behaviour, and so avoiding a time consuming last square fit to the measured data with (7.18).

7.6   Validation

In order to evaluate the accuracy of the method, the effect of errors in the phase velocity and guided wave attenuation measurements on the bulk properties evaluation has been studied numerically. For a system with the properties shown in tab. 7.1, it has been found that the best sensitivity is reached around the frequency of the first guided wave attenuation peak over a frequency range of 60% of the peak frequency (60% bandwidth). In particular, for a 10% guided wave attenuation error and a 1% phase velocity error, which are representative of the level of confidence of the measurements, the maximum bulk shear velocity and bulk attenuation errors are about 4% and 20% respectively. However, the errors at the frequency of maximum guided wave attenuation are considerably lower (2% and 12% in the bulk velocity and bulk attenuation estimates respectively).

The lack of data on the acoustic properties of viscoelastic materials makes the validation of the technique very difficult. One possibility would be the use of viscous liquids, such as glycerol whose viscosity data are available in literature. However, due to the low value of the viscosity, the shear impedance of glycerol is much lower than that of any metal. As a consequence, the amount of energy which can be transferred from the tube into the fluid core is very low. This leads to a low value of the guided wave attenuation which is difficult to measure unless a very long tube is used. On the other hand, high viscosity standards are extremely sensitive to
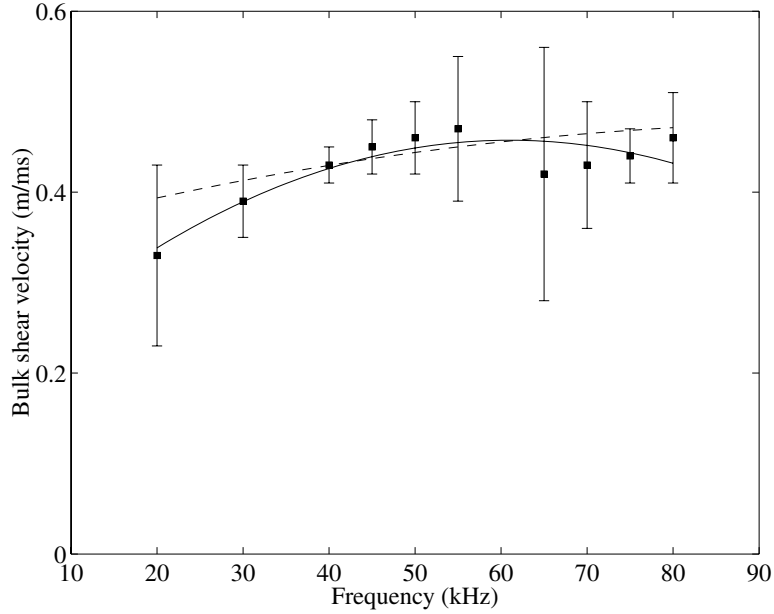
Figure 7.14: Bulk velocity dispersion curve for bitumen TML 24515 45/60: (■) experiments; (———) experimental data interpolation; ($- - -$) Kramers-Krönig formula.

temperature changes. For instance, Polybutene viscosity varies from $36.2 Pa \cdot s$ to $18.3 Pa \cdot s$ when the temperature ranges between $293K$ and $299K$. As a result, an extremely accurate temperature control would be required. Moreover, some concerns arise about the validity of the Newtonian model for these large values of the viscosity.

A partial validation of the technique comes from the fact that the dispersion curves obtained for bitumen are in reasonable agreement with the Kramers-Krönig relationship [32], according to which the bulk shear velocity spectrum can be derived from the bulk attenuation spectrum

$$\frac{1}{c_0} - \frac{1}{c(\omega)} = \frac{2}{\pi} \int_{\omega_0}^{\omega} \frac{\alpha(\omega')}{\omega'^2} d\omega', \tag{7.19}$$

where c_0 is the velocity at the reference angular frequency ω_0 and $\bar{\alpha}$ is the bulk attenuation in neper per unit length. Fig. 7.14 shows the measured bulk shear velocity and the prediction from the Kramers-Krönig formula applied to the experimental bulk attenuation spectrum shown in Fig. 7.13b. The error bars indicate the level of confidence of the measured bulk velocities; the estimated errors vary with velocity as discussed above. The reference frequency in the integral (7.19) was chosen to be equal to the frequency of maximum guided wave attenuation (40kHz) since, at

this frequency, the level of confidence of both bulk attenuation and bulk velocity is optimum. The measured bulk velocities (squares) fit well with the Kramers-Krönig formula prediction (dashed line) for frequencies ranging between 30 and $55kHz$. However, at higher frequency, the fitting becomes less accurate. This is due to the fact that, close to the frequency of the second guided wave attenuation minimum, the sensitivity drops as shown by the error bars in Fig. 7.14. The bulk velocity for a simple viscoelastic material should increase monotonically with frequency whereas Fig. 7.14 suggests that the velocity has a local maximum at around $60kHz$. This apparent maximum is probably due to the increased error in the estimates around the second guided wave attenuation minimum.

7.7   Summary

A novel technique for the characterisation of highly attenuative viscoelastic materials has been presented. It has been shown that by measuring the dispersion curves of a tube filled with the unknown material the shear acoustic properties can be obtained. The method is based on the hypothesis of linear viscoelasticity and no assumptions are made about the frequency dependence of the acoustic properties as a monochromatic approach is followed.

The technique is attractive since many of the limitations common to traditional methods including beam spreading, sample manufacturing, transducer coupling, etc. are overcome. On the other hand, the need for the material to be moulded into the tube represents a limitation in the case of solid materials, since melting the material would dramatically change the properties. By contrast, the method is particularly suitable for materials that will flow as the tube can then easily be filled.

Chapter 8

Shear properties of solid viscoelastic materials

8.1 Background

As has been discussed in the previous Chapters, the measurement of the shear acoustic properties of solid viscoelastic coatings plays a major part in the prediction of the test range of an ultrasonic guided wave propagating in a coated pipeline. Since the properties of viscoelastic materials are extremely sensitive to temperature variations and oxidation phenomena which strongly depend on the surrounding environment, there is a need for a technique which allows rapid in-situ measurements to be performed. The main difficulty comes from the limited dimensions of samples (typically the size of a coin) due to the breakage of the coating as it is detached from the metallic substrate. Moreover, since for guided wave testing the frequency is well below 100kHz, only the low ultrasonic frequency properties of the coating are of interest.

In order to measure the shear properties of solid viscoelastic materials, the technique presented in the previous chapter cannot be employed, unless the material is melted and moulded into the tube. However, such a procedure is not always applicable since the material properties may dramatically change as a result of the thermal treatment. Traditional ultrasonic techniques [69, 70, 73, 74, 75, 76] for the measurement of longitudinal properties are based on the response of a sample to an

acoustic perturbation. Such a response can be measured by placing either solid or fluid delay lines between the sample and the acoustic source/receiver. Measurement of shear properties is more complex. First, shear waves do not propagate in liquid couplants due to the low viscosity; consequently, in order to transmit shear stresses through the contact interface between the excitation source and the sample, rigid coupling is needed. One possibility is to cement the acoustic source onto the sample. However, in order to avoid interference of the acoustic signal with the glue layer, the wavelength of the signal has to be much larger than the glue thickness. Most importantly, chemical reactions between the glue and the sample have to be avoided as they could dramatically change the mechanical properties of the sample. Moreover, such a procedure is time consuming and not suitable for rapid testing. Alternatively, liquid delay lines can be used. In this case, the sample is immersed in a liquid bath and interrogated with an oblique longitudinal wave. The scattered longitudinal field depends on both shear and longitudinal properties of the sample as the incident wave undergoes mode conversion into shear and longitudinal bulk waves within the sample. As a consequence, it is possible to derive the sample properties (shear and longitudinal) from the scattered field through an inversion procedure [72]. However, the accuracy of the measurements decreases when the incident signal wavelength is large compared to the sample dimensions. Solid delay lines are more attractive as they can support shear waves, and the shear properties can directly be derived from the shear scattered field. However, the coupling of the solid buffer with the sample remains an issue.

This Chapter describes and evaluates a new technique for the measurement of the shear properties of viscoelastic solids. A small cylindrical sample is clamped between two buffer rods. Neither glue nor couplant is used at the interfaces between the sample and the two buffers. Sec. 8.3 investigates the possibility of deriving the sample properties from either the reflection or transmission coefficients of the fundamental torsional guided mode, $T(0,1)$, through the sample. Sections 8.4 and 8.5 describe the experimental apparatus and its calibration. Results for bitumen are given is Sec. 8.6, where the technique is also validated.
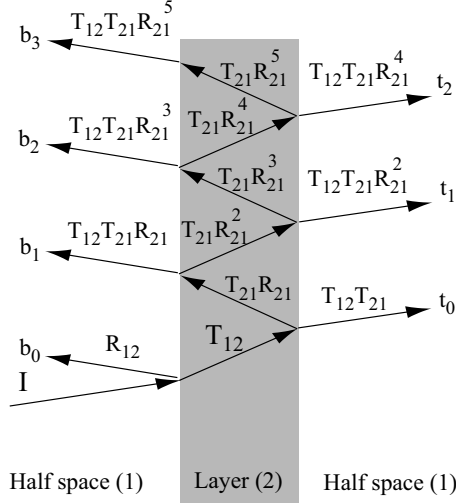
Figure 8.1: Schematic diagram of the reflection and transmission of a normally incident wave through a layer separating two half spaces. (non-perpendicular incidence is shown for clarity)

8.2 Previous work

It is known from optics that if a monochromatic plane wave, I, is incident on a layer which separates two half spaces, it undergoes infinite partial reflections within the layer as shown in Fig. 8.1. Such reflections cause an interference phenomenon between the front reflection, b_0, and the infinite back reflections, b_i emerging from the back face of the layer. Similarly, an interference occurs between the wave which penetrates the layer, t_0, and the reflections from the layer front face, t_i. If the incident plane wave is perpendicular to the layer and of unit amplitude, the total reflection, R, and the total transmission, T, are [43]

$$R = R_{12} + \frac{T_{12}T_{21}R_{21}e^{i2k_2d}}{1 - R_{12}^2 e^{i2k_2d}}, \tag{8.1}$$

$$T = \frac{T_{12}T_{21}e^{ik_2d}}{1 - R_{12}^2 e^{i2k_2d}}, \tag{8.2}$$

where the subscripts 1 and 2 refer to the half spaces and the layer, respectively. The coefficients R_{ij} and T_{ij} are the reflection and transmission coefficients at the interface between the half spaces i and j when an incident wave travels from the half space i to the half space j. For acoustic stress waves, by defining the complex impedance Z as [25]

$$Z = \rho a, \tag{8.3}$$

where ρ is the density, a the complex velocity [(2.14) or (2.15)], the reflection and transmission coefficients of either longitudinal or shear waves are

$$R_{ij} = \frac{Z_j - Z_i}{Z_i + Z_j}, \tag{8.4}$$

$$T_{ij} = \frac{2Z_j}{Z_i + Z_j}. \tag{8.5}$$

By substituting (8.4) and (8.5) into (8.1) and (8.2) the total reflection and transmission coefficients can be related to the material impedances

$$R = \frac{Z_2^2 - Z_1^2}{Z_2^2 + Z_1^2 + 2iZ_2Z_1cot(k_2d)}, \tag{8.6}$$

$$T = \frac{4Z_2Z_1}{(Z_1 + Z_2)^2 e^{-ik_2d} - (Z_1 - Z_2)^2 e^{ik_2d}} \tag{8.7}$$

$$\tag{8.8}$$

In the case of propagation in lossless media, the impedances are real and constant with frequency [see eq. (8.3)], and the total reflection and transmission coefficient moduli are periodic functions of the wavenumber-layer thickness product, k_2d. Reflection coefficient modulus maxima ($|R| = 1$) occur when

$$\frac{d}{\Lambda} = \frac{2N - 1}{4} \qquad N\epsilon\{1, 2, ...\}, \tag{8.9}$$

where Λ is the wavelength within the layer ($\Lambda = c_2/f$). On the other hand, the reflection coefficient vanishes when

$$\frac{d}{\Lambda} = \frac{N}{2} \qquad N\epsilon\{0, 1, 2, ...\}. \tag{8.10}$$

Conversely, by energy conservation, transmission coefficient minima and maxima are given by (8.9) and (8.10), respectively. In other words, at the through thickness resonance frequencies of the free layer [corresponding to condition (8.10)], the incident wave does not "see" the layer and all the energy is transmitted without being reflected.

The resonance condition (8.10) provides two direct methods for the measurement of the bulk velocity c_2. The first method, known as thickness interferometry, is based on the measurement of the reflection or transmission coefficients as a function of the layer thickness, d, at constant frequency (constant wavelength). The reflection

coefficient modulus versus layer thickness, here referred to as the d-spectrum, exhibits minima when the thickness is a multiple of half the wavelength according to (8.10). Therefore, by measuring the distance between two consecutive minima, Δd, the bulk velocity, c_2, can be obtained from (8.10)

$$c_2 = 2f\Delta d. \tag{8.11}$$

In a similar fashion, by measuring the transmission d-spectrum the bulk velocity can be obtained from the distance between two consecutive peaks using (8.11). Thickness interferometry has been employed for the measurement of the longitudinal acoustic properties of gases [86] and several types of liquids such melts [87, 88, 89, 90, 91] and biological tissues in vitro [92, 93]. The application of this technique has been limited to the case of fluids as the layer thickness can be varied continuously by maintaining perfect coupling between the fluid layer and the two half spaces.

Frequency interferometry is based on the same principle as thickness interferometry. In this case either R or T are measured as a function of the frequency at constant thickness. The frequencies where reflection minima and transmission maxima occur correspond to the through thickness resonances of the free layer. As a result, the bulk velocity can be obtained by measuring the frequency interval, Δf, between two consecutive transmission peaks or reflection minima, according to

$$c_2 = 2d\Delta f. \tag{8.12}$$

When material absorbtion is considered, due to the fact that the impedances and the wavenumber k_2 are complex, the ratios d/Λ where maxima and minima of the reflection and transmission coefficients occur are shifted from the values provided by (8.9) and (8.10). However, the magnitude of the shift, which depends on the amount of internal damping, is usually negligible as discussed by Katahara et al. [87]. As a result, c_2 can still be derived from (8.11) and (8.12).

8.3 Method

Frequency interferometry is particularly suitable for the measurement of the acoustic properties of solids as, by contrast with thickness interferometry, there is no need for varying the sample thickness. However, whereas thickness and frequency interferometry are equivalent for a lossless system, a significant difference exists when material damping is considered. In particular, thickness interferometry is a monochromatic method (measurements are performed at constant frequency) and the d-spectra do not depend on the frequency dependence of the layer acoustic properties, $\alpha_2(\omega)$ and $c_2(\omega)$. Therefore, at a prescribed frequency ω_0, $R(d)$ and $T(d)$ are known functions of the layer thickness and the two unknown parameters $c_2(\omega_0)$ and $\alpha_2(\omega_0)$ only [see (8.6) and (8.7)]. Moreover, since $c_2(\omega_0)$ can be obtained from (8.11), $\alpha_2(\omega_0)$, can be found by best fitting either R(d) or T(d) to the corresponding experimental d-spectra [87].

In the case of frequency interferometry, such a procedure cannot be employed since the frequency dependence of the acoustic properties c(ω) and $\alpha(\omega)$ is unknown. As a consequence, the functions $R(\omega)$ and $T(\omega)$ are unknown. In other words, the shape of the reflection and transmission coefficient spectra depends on the shape of the acoustic property spectra. Moreover, for a highly dispersive material, (8.12) can no longer be employed as it requires the periodicity of $R(\omega)$ and $T(\omega)$. However, in a sufficiently narrow band of frequency, outside the transition between the material rubbery and glassy behaviour [94], it can always be assumed that the bulk velocity c is constant with frequency and that α is a linear function of the frequency (see Sec. 2.5)

$$\alpha_2 = \frac{\bar{\alpha}_2}{c_2}f, \tag{8.13}$$

Under these assumptions, the problem becomes formally equivalent to thickness interferometry. The material properties, and consequently $R(\omega)$ and $T(\omega)$, are now known functions of the unknown parameters c_2 and $\bar{\alpha}_2$. The bulk velocity c_2 can be obtained from the frequency interval between two consecutive transmission peaks or reflection minima according to (8.12) (note that the number of peaks or minima occurring in a given frequency band depends on the layer thickness). The bulk at-

tenuation $\bar{\alpha}_2$ is obtained by best fitting the functions $R(\omega)$ or $T(\omega)$ to the measured spectra.

It has to be emphasized that if the assumptions of constant velocity and constant attenuation per wavelength do not hold in the frequency range of interest the method becomes inaccurate. Nevertheless, the acoustic properties can be found by dividing the frequency range into smaller intervals, where the simple rheological model holds, and increasing the sample length so as to have enough reflection maxima and transmission minima in the interval. In each interval, the validity of this model can be assessed by considering the matching between the experimental spectra and the analytical expressions. As an example, if the shear velocity is highly dispersive, transmission maxima and reflection minima are no longer equally spaced in the frequency domain.

The theory discussed so far refers to the case of plane waves propagating in a boundless space containing an infinite plane layer with finite thickness. Formulae (8.6) and (8.7) provide the scattering coefficients for both longitudinal and shear bulk waves when they impinge the layer perpendicularly. Since the purpose of this Chapter is to assess the shear properties of the layer, it would be sufficient to measure the reflection and transmission coefficients of a shear bulk wave through the layer rigidly clamped between two large blocks of known properties. However, the propagation of bulk waves is always accompanied by beam spreading due to the finite size of the acoustic source and receiver.

In order to avoid beam spreading guided waves can be employed. Appendix B shows that the reflection and transmission coefficients of the fundamental torsional mode, $T(0,1)$, through a disk rigidly clamped between two identical, infinite long rods are still provided by (8.6) and (8.7). As a result, the shear properties of the disk can be obtained by measuring the reflection and transmission coefficients of $T(0,1)$ following the procedure previously discussed for bulk waves. It is interesting to observe that while $T(0,1)$ and all the other torsional modes do not undergo mode conversion (see Appendix B), all the longitudinal modes propagating above the cutoff frequency

of the second longitudinal mode [31] experience mode conversion at the interfaces between the two rods. Moreover, while eqs (8.6) and (8.7) are exact expressions for the scattering of $T(0, 1)$, they only represent approximate solutions for the low frequency scattering of longitudinal modes when the bulk velocity c is replaced with the phase velocity of the first longitudinal mode [36].

The interferometry discussed in this Chapter reproduces in principle the resonant bar technique [95, 96]. In this case, the shear velocity of a rod is measured by fixing two accelerometers at the free ends of the rod and then measuring the frequency interval between two consecutive resonances of the free rod according to (8.12). However, the presence of the accelerometers produces a shift of the resonance frequencies which may lead to significant errors especially when the sample dimensions are limited. This problem has been overcome with the split-bar method [97, 98]. In this case, the sample is clamped between two rods and its acoustic properties are derived from the resonance frequencies of the rod-sample-rod system. However, the resonances of such a system are different from those of the free sample as they also depend on the rod properties and the accelerometer masses. This is a consequence of the harmonic excitation of the system which means that the response measured is that of entire rod-sample-rod system due to the superposition of infinite reflections of the harmonic wave at the free ends of the system. On the other hand, the novelty of the method presented in this Chapter is that the two rods work as delay lines which drive an acoustic wave pulse onto the sample. As a consequence, the reflection and transmission through the sample can completely be separated from the reflections at the free ends of the rods and (8.12) remains valid. This method is more advantageous than the split-bar method since the velocity can be derived from the explicit expression (8.12) rather than inverting more complex resonance expressions as in the case of the split-bar method. Moreover, the method proposed here is more robust because expression (8.12) does not involve either the properties of the rods or the transduction which are potential sources of uncertainty.
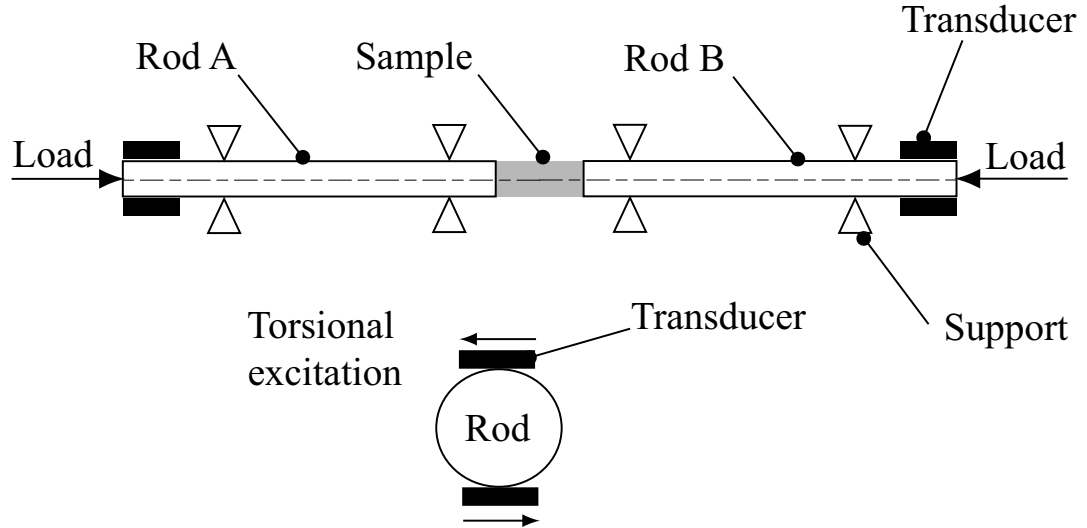
Figure 8.2: Diagram of the apparatus for shear property measurements

8.4   Experimental setup

The setup consisted of two identical stainless steel cylindrical rods of 6mm diameter and 333mm long (the acoustic properties are reported in Tab. 8.1). Alignment of the rods was ensured by two cylindrical supports on each rod which allowed the rod to slide axially as shown in Fig. 8.2.   Moreover, so as to reduce reflections from the contact interfaces rod-support, the support were made of Nylon 6 whose acoustic impedance is much lower than that of steel. In order to excite and detect the $T(0,1)$ mode, at one end of each rod two piezoelectric transducers were firmly clamped onto the rod lateral surface. The transducers, which were similar to those used for pipe testing [17] and in Chapter 7, comprised shear elements mounted on a steel backing mass, excited in parallel and oriented as in Fig. 8.2 to induce torsion. The use of two transducers operating in such a configuration is required in order

Table 8.1: Material bulk properties.

Material	Velocity (m/s)	Attenuation (np/wl)	Density (kg/m^3)
Steel	3260	–	7804
POM	890	0.10	1553

to avoid the generation of a bending mode which would interfere with $T(0,1)$. A custom-made waveform generator-power amplifier excited the transducers on rod A (see Fig. 8.2) by a Hanning windowed toneburst. The acoustic response of the system was monitored by receiving the signal with the transducers of rod A operating in pulse-echo mode and those of rod B in pitch-catch mode. The pulse-echo and pitch-catch signals were amplified and transferred to a digital oscilloscope (LeCroy 9400) for digital capture and then stored in a PC.

According to the theory of linear slip interfaces [99, 100, 101], the dry contact between two surfaces can be model by an interfacial spring stiffness, the condition of perfect bonding [eqs (B.9) and (B.10)] being achieved when the spring stiffness is infinite. The stiffness, which depends on the geometry of the contact and on the surface materials, increases under the effect of an applied pressure [102, 103]. Therefore, in order to ensure the continuity of displacement and stress at the interfaces between the rods and the disk, an axial compressional load was applied at the free end of each rod by means of a screw.

8.5   Measurement procedure

In order to measure the reflection and transmission coefficients the apparatus was calibrated by performing two types of measurement. At first no sample disk was placed between the two rods which were separated by an air gap. In this configuration the pulse-echo response of rod A (see Fig. 8.2), PE_{air}, was recorded. Subsequently, the two rods were put in contact under a compressional load, and the pulse-echo signal of rod A, $PE_{steel/steel}$, and the pitch-catch signal $PC_{steel/steel}$ were measured. Note that the magnitude of the compressional load is arbitrary since, for the calibration purpose, no intimate contact between the rods is required as discussed later in this section.

Once the calibration measurements were completed, a material sample, previously cut into a 6mm diameter disk, was placed between the rods. Neither couplant nor

glue were employed. The rods were gradually loaded axially and the variations of the transmitted signal continuously monitored on the oscilloscope. The load was increased until the transmitted signal became insensitive to load increments, this condition ensuring intimate contact between the rods and the sample. At that point, the pulse-echo signal of rod A, $PE_{steel/disk/steel}$, and the pitch-catch signal, $PC_{steel/disk/steel}$ were recorded.

As the air impedance is negligible with respect to steel, PE_{air} corresponds to unit reflection coefficient therefore, the reflection coefficient R is given by

$$R = \frac{PE_{steel/disk/steel}}{PE_{air}}. \tag{8.14}$$

Note that the quantities appearing in the previous relationship and in the rest of this section are the Fourier transforms of the time traces.

The transmission coefficient cannot be calculated by dividing the pitch-catch response, $PC_{steel/disk/steel}$, by PE_{air} as the rod-transducer transfer functions of the two rods do not necessarily coincide due to differences in the transducers and in the coupling. Moreover, the transfer functions of the pulse-echo and pitch-catch lines are different too. However, it is possible to express the transmission coefficient as

$$T = \eta \frac{PC_{steel/disk/steel}}{PE_{air}}, \tag{8.15}$$

where η is a frequency dependent correction factor which can be derived from the pitch-catch response of the rod-rod contact. In this case, the reflection coefficient at the interface steel-steel, Ψ, is

$$\Psi = \frac{PE_{steel/steel}}{PE_{air}}. \tag{8.16}$$

Due to the low frequency considered, it can be assumed that there is no energy dissipation due to internal damping in steel and at the interface between the two rods. As a consequence, by energy conservation, the transmission coefficient steel-steel, ν, can be related to Ψ according to

$$|\nu| = \sqrt{1 - |\Psi|^2}. \tag{8.17}$$

As a result, since

$$\nu = \eta \frac{PC_{steel/steel}}{PE_{air}}, \tag{8.18}$$

by equating (8.17) and (8.18), it follows that

$$|\eta| = \left| \frac{PE_{air}}{PC_{steel/steel}} \right| \sqrt{1 - |\Psi|^2}. \tag{8.19}$$

Thus, η can be found from the calibration measurements with no need to determine the quality of the steel-steel contact in the pitch-catch calibration test. The correction factor so obtained can be substituted into (8.15) to provide the transmission coefficient T.

8.6   Results

The experiments were performed at room temperature, 298K. Figure 8.3a shows the first and second echo reflected at the free end of rod A measured by operating the transducers in pulse-echo mode. Figure 8.3b is the pulse-echo response of rod A when a 18.5mm long Acetal Copolymer Plastic [chemical name polyoxymethylene copolymer, POM], cylinder is clamped between rods A and B. In this case, each echo consists of a train of signals which contains the front reflection b_0 and the infinite series of back reflections b_i (see Sec. 8.2). The amplitude of the front reflection b_0 is much larger than b_1 since the steel shear impedance is almost twenty times that of POM. Moreover, the amplitude of the back reflections b_i rapidly decays due to energy release into rod B and absorbtion within the POM cylinder. This is more evident from the pitch-catch response shown in Fig. 8.3c. Also in this case there are two trains of signals. The first train corresponds to the transmitted $T(0,1)$ mode and comprises the signal t_0 and all the reverberations from the front face of the cylinder, t_i (see Sec. 8.2). The second train, is the interference of the reverberation of the first train along rod B and the signal transmitted by the train reverberating along rod A.

The reflection and transmission coefficients were calculated by following the procedure discussed in the previous section. It has to be emphasized that formulae (8.6)
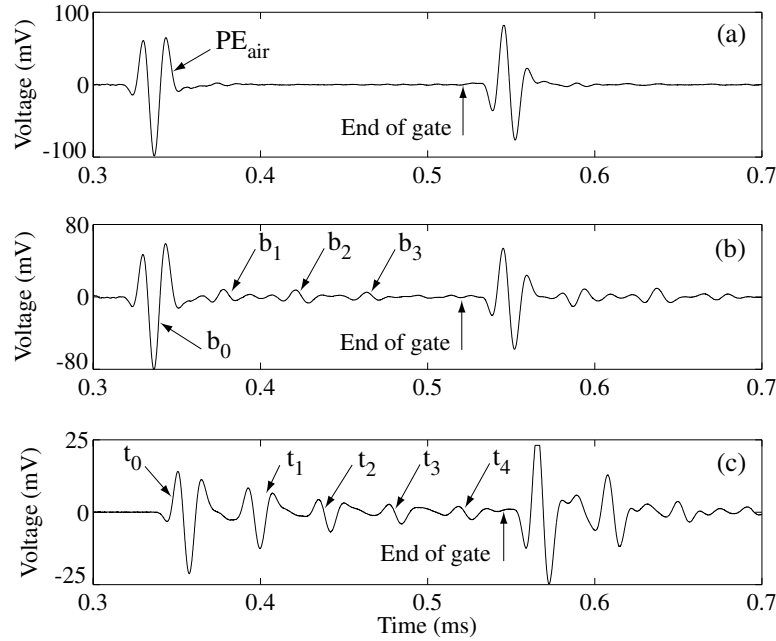
Figure 8.3: (a) Typical time-domain signal reflected from the free end of rod A; (b) signal reflected at the interface between rod A and a 18.5mm thick POM cylinder clamped between rods A and B; (c) signal transmitted in the same configuration as (b).

and (8.7) hold when the steel rods are infinitely long. However, due to the rapid decay of the reverberations within the cylinder, only a finite length of the rods which ensures enough time resolution between the first two trains of signals is required. As a result, for each time trace, the first train of signals was gated out as shown in Fig. 8.3, and subsequently Fourier transformed. The spectra so obtained were processed according to Sec. 8.5 to provide the reflection and transmission coefficient spectra shown in Fig. 8.4. The transmission coefficient exhibits peaks which occur at equally spaced frequencies, $\Delta f = 23.5 kHz$; this confirms that the bulk shear velocity does not change in the frequency range of Fig. 8.4. From eq. (8.12) it follows that the bulk velocity is 870m/s. The same result can be obtained by considering the reflection coefficient minima which occur every 23.5kHz (Fig. 8.4). However, it can be observed that the reflection coefficient spectrum contains more noise than the transmission spectrum (Fig. 8.4). This is due to the fact that, by contrast with the transmitted signal, a large difference between the amplitude of the front reflection b_0 and the back reflections b_i occurs (Figs 8.3b,c). Such a difference amplifies the effect of noise in the time trace when the Fourier transform is performed. As a
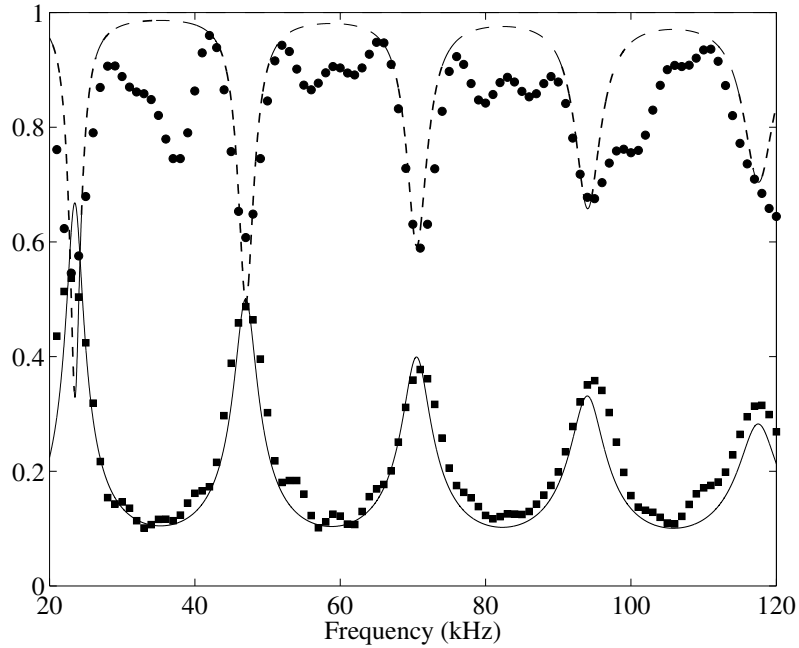
Figure 8.4: Measured reflection (•) and transmission (■) coefficient spectra for the POM cylinder clamped between the two rods. (———) transmission coefficient best fit; $(---)$ reflection coefficient calculated for $c_2 = 870$m/s and $\bar{\alpha}_2 = 0.105$Np/wl.

result, in order to derive the bulk attenuation, only the least square fitting (LSF) of (8.7) to the measured transmission spectrum was considered. For the POM cylinder, the optimum value of $\bar{\alpha}$ was 0.105 Np/wl. The transmission and reflection spectra calculated through (8.7) and (8.6) for $c_2 = 870$m/s and $\bar{\alpha}_2 = 0.105$Np/wl are shown in Fig. 8.4 with solid and dashed lines, respectively. For the transmission coefficient, the fitting is good around the centre frequency of the toneburst (60kHz) and becomes less accurate close to the limits of the pulse band width (around 20 and 110kHz the pulse energy is low). On the other hand, the noise level of the reflection coefficient spectrum is quite large as mentioned before. The noise can be reduced by using plastic rods so as to reduce the impedance mismatch between the sample and the two rods. In this case, the bulk attenuation can be derived by LSF of (8.6) to the experimental reflection coefficient. However, here the analysis is limited to the use of steel rods and the bulk attenuation is derived from the transmission spectrum only.

In order to obtain independent values of the bulk velocity and attenuation of POM,

a 6mm diameter 1m long POM rod was tested. The bulk shear properties were derived from the guided wave attenuation and phase velocity spectra of the $T(0,1)$ mode excited at one end of the POM rod, these spectra corresponding to the dispersion of the bulk properties of the rod [see eq.(7.2)]. The $T(0,1)$ mode was monitored by means of laser scanning along the rod axis, $T(0,1)$ being excited with a pair of transducers arranged as discussed in Sec. 8.4. The signals recorded at different axial positions were Fourier transformed in order to extract the phase velocity and guided wave attenuation spectra as described in Chapter 7. In the frequency range of interest (between 20 and 100kHz), both the shear velocity and the bulk attenuation per wavelength ($\bar{\alpha}$) were constant with frequency, the values being summarized in Tab. 8.1.

The shear velocity obtained from the rod scanning was 2.3% higher than that measured with the frequency interferometry, while the bulk attenuation was 5% lower. These differences are around the error levels of the scanning measurements (1% for phase velocity and 10% for attenuation) therefore, they can be regarded as a relative estimate of the sensitivity of the frequency interferometry method but not as absolute errors. Moreover, the accuracy level of the POM property measurement is affected by the imperfect time resolution between the two trains of signals shown in Fig. 8.3c which produces errors in the evaluation of the transmission coefficient. As a consequence, the previous estimate of the relative error is conservative when more attenuative materials like bitumen are considered since, in this case, perfect time resolution between the first and second transmitted train of signals can be achieved.

8.6.1 Bitumen

Since bitumen is softer than POM the condition of good bonding between the disk and the two rods was reached for very low values of the axial compressional load. Figure 8.5 shows the time traces obtained for a 4.9mm long bitumen cylinder from the coating of a gas pipeline in Dallington (UK), the density being $1750 kg/m^3$. Note that the reverberations in the steel rods are not visible as the time scale is finer than that of Fig. 8.3. Figure 8.5a is the pulse-echo response of the free rod A. Figure 8.5b
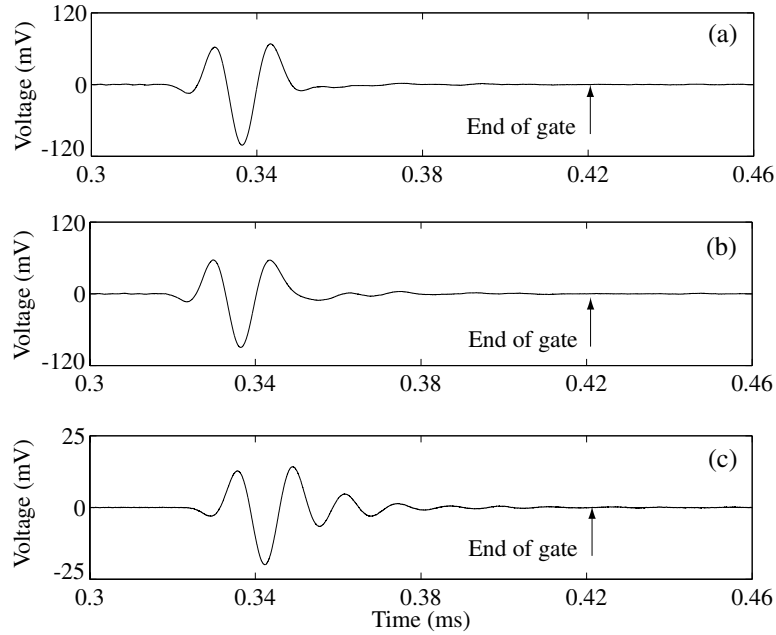
**Figure 8.5:** (a) Time-domain signal reflected from the free end of rod A; (b) signal reflected at the interface between rod A and a 4.9mm thick bitumen disk clamped between rods A and B; (c) signal transmitted in the same configuration as (b)

shows the reflection at the steel-bitumen interface of rod A. Comparison of the time traces (a) and (b) suggests that the reflection coefficient is very little affected by the presence of the bitumen sample since trace (a) and (b) are very similar. Moreover, back reflections cannot be identified due to the low impedance of bitumen and high attenuation. On the other hand, the transmitted signal (Fig. 8.5b) clearly shows the presence of reverberations from the disk front face t_i. However, these signals are not resolved from the first signal t_0 due to the small sample thickness. On the other hand, a perfect resolution between the first and second train of signals is achieved. This allows the transmitted signal to be completely separated from the reverberations inside the steel rods so improving the accuracy of the transmission coefficient measurement.

Figure 8.6 shows the transmission coefficient spectrum derived from the time traces of Fig. 8.5. The transmission peak shown in Fig. 8.6, which occurs at 79kHz, is the second peak as the first peak occurs where the frequency vanishes [see (8.7)]. Therefore, $\Delta f = 79kHz$ and by applying (8.12) the corresponding shear velocity is
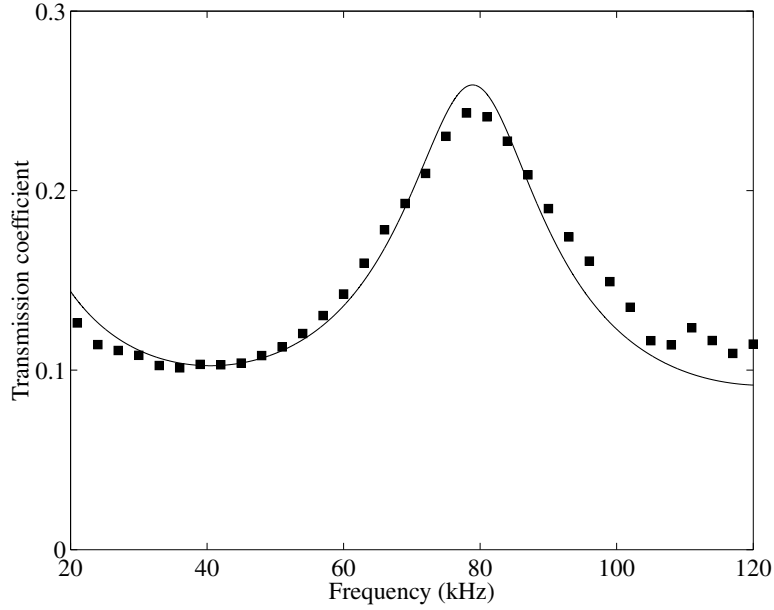
Figure 8.6: (■) Measured transmission coefficient spectrum for the bitumen disk; (———) best fit.

770m/s. The shear attenuation, obtained by LSF of (8.7) to the measured transmission coefficient is 0.591Nepers/wavelength which is much larger than that of POM, expected since bitumen is an extremely attenuative material as shown in Chapter 7. The good agreement between the experimental points and (8.7) indicates that the shear velocity and shear attenuation $\bar{\alpha}$ are roughly constant when the frequency ranges between 20 and 120kHz.

Table 8.2 gives the shear properties of bitumen coating from four different sites and shows how the coating properties can change depending on the location of the pipeline. The data shown in Tab. 8.2, which have been measured with the technique

Table 8.2: Shear properties of bitumen coatings from different sites.

Location	Velocity (m/s)	Attenuation (np/wl)	Density (kg/m^3)
Dallington	770	0.59	1750
Kuwait	1012	0.24	1640
Oncor	1065	0.45	1442
Louisiana	642	0.32	1544

presented in this Chapter, demonstrate the need for in-situ measurements of the coating properties.

8.7   Summary

A technique for the measurement of the bulk shear properties of solid viscoelastic materials has been studied and its sensitivity estimated. It has been shown that the bulk shear velocity of a sample clamped between two rods can be obtained by measuring either the reflection or transmission coefficient spectra of the fundamental torsional mode through the sample. The bulk shear attenuation has been derived through a least square fitting of the analytical expression of the transmission coefficient to experimental data.

The good level of accuracy obtained for the shear properties of Acetal Copolymer Plastic, shows that a "rigid" contact between the sample and the two rods can be achieved by applying a moderate compressional load at the free ends of each rod. As a consequence, since there is no need for the sample to be glued between the rods, the technique is particularly advantageous for rapid measurements. Moreover, as for a lossless sample at the through thickness resonances, all the energy passes through the sample without being reflected irrespective of the impedance difference between the sample and the rods, this technique is particularly suitable for the measurement of very low impedance materials provided the bulk attenuation is low enough.

Moreover, the variability of the shear properties of the coating has been demonstrated by performing tests on a number of samples from different locations. This has proved that, in order to assess the feasibility of long range inspection of coated pipelines, there is a need for in-situ characterisation of the coating shear properties.

Chapter 9

Conclusions

9.1 Thesis Review

This thesis has investigated the propagation of acoustic guided waves in elastic plates coated with viscoelastic layers in order to assess the feasibility of long range inspections of coated pipelines. As discussed in Chapter 1, the possibility of using guided waves is very attractive since the screening of the pipeline can be performed without the need for scanning of the entire pipe surface.

The theory developed in this thesis concentrated on the propagation of SH and Lamb waves in bilayered plates since, when the pipe diameter to wall thickness ratio is large (as in the majority of coated pipelines), these modes are equivalent to torsional and longitudinal waves propagating in hollow cylinders which are the modes employed for the detection of defects in pipes.

The basic concepts of wave propagation in viscoelastic unbounded media were reviewed in Chapter 2, where the effects of the material absorption on the propagation characteristics of elastic waves were examined.

The propagation of SH waves in bilayers was addressed in Chapter 3. Also in this case, the dispersion characteristics of the attenuative bilayer were compared to those of a perfectly elastic system, in order to understand how the material absorption in the coating affects the guided wave.

The study of SH waves was extended to the case of Lamb waves in Chapter 4 where the same analytical approach as in Chapter 3 was employed. However, since Lamb waves originate from the superposition of longitudinal and shear bulk waves, the effects of both dilatational and distortional material absorptions had to be considered.

In order to identify the modes and the frequencies which minimise the guided wave attenuation, so maximizing the distance over which defects can be located, a comparison between SH and Lamb waves was carried out in Chapter 5.

Chapter 6 investigated the role of the nonpropagating modes of a perfectly elastic bilayer on the dispersion curves of the attenuative bilayer, so completing the analysis undertaken in Chapter 4. For this purpose the modes of a free plate, both elastic and viscoelastic, were considered first.

In order to quantify the attenuation of guided waves, in Chapter 7 a novel technique for the measurement of the shear bulk velocity and bulk attenuation of fluid viscoelastic materials was presented.

The technique discussed in Chapter 7 can characterise the coating properties when it is applied in its liquid state. However, when the coating has been exposed to atmospheric agents for a long time, as in the case of old pipelines, its acoustic properties change dramatically, and due to oxidation phenomena, the material behaves as a solid rather than a liquid, though its attenuation is still high. Therefore, in Chapter 8 a new technique for the characterisation of the shear properties of solid viscoelastic materials which allows rapid in-situ measurement to be performed, was addressed.

9.2   Summary of theoretical findings

The theoretical investigation undertaken in this thesis has led to a better understanding of guided wave propagation in absorbing waveguides. In the next subsections a

summary of the general properties of acoustic waves in attenuative waveguides and an overview of the characteristics of guided waves in bilayered plates are given.

9.2.1 General results

Through Chapters 3, 4 and 6 it was shown that if the waveguide is nonelastic (absorbing) nonpropagating modes do not exist. This implies that the concept of mode cutoff (infinite wavelength) which for a conservative system identifies the condition under which a mode stops carrying energy whereas there is still motion in the waveguide, loses its significance for attenuative waveguides. Moreover, as was discussed in Chapter 6, the topology of the dispersion curves of an elastic waveguide can only be understood by considering the elastic modes as the limit towards which the modes of the attenuative system tend as the material damping vanishes. This has been submitted for publication [P7] (see List of publications arising from thesis).

9.2.2 Nature of the bilayer modes

The dispersion curves of the bilayer are characterised by the fact that the metallic layer is much stiffer and heavier than the coating.

If the material damping in the coating is neglected, the bilayer modes result from the interaction between the modes of the free metallic plate, referred to as the first asymptotic family, and the modes of the coating if it were rigidly clamped at the interface with the metallic plate, termed the second asymptotic family. These two families represent the asymptotic solution to the dispersion equations of the bilayer as the density and stiffness of the metallic plate go to infinity while keeping the bulk velocities constant, as was demonstrated in Chapters 3 and 4. These Chapters also showed that each bilayer mode jumps from one asymptotic family to the other, this behaviour being termed the mode jumping. The mode jumping occurs also for attenuative bilayers, provided the material absorption is low. For large material damping, the modes no longer jump, and the bilayer modes tend to the modes of

one asymptotic family only as discussed in Chapters 3 and 4.

In Chapters 3 and 4 it was shown that for large material damping, the modes which tend to the second asymptotic family are characterised by large levels of guided wave attenuation since the vibrations are localised in the attenuative layer while there is little motion in the elastic plate. On the other hand, the modes which tend to the first family have lower attenuation as the energy primarily travels in the elastic plate and they can be employed for practical testing. Moreover, the guided wave attenuation spectra of the modes which tend to the first asymptotic family exhibit maxima which occur where the mode would jump if the bilayer was perfectly elastic as explained in Chapter 3. Furthermore, in the case of SH waves, minima in the guided wave attenuation spectra occur at the Love transition frequencies.

In order to study the effects of longitudinal and shear material absorptions on the attenuation characteristics of guided waves, the guided wave attenuation was related to the energy distribution within the viscoelastic layer. This led to the introduction of the concept of first and second energy factors in Chapters 3 and 4. While the first energy factor accounts for the strain energy contained in the viscoelastic layer when a unit power flows through the bilayer cross section, the second energy factor refers to the difference between the strain and kinetic energies contained in the viscoelastic layer when unit reactive power flows through the bilayer cross section. It was demonstrated that in the first order approximation, the guided wave attenuation can be expressed as a linear combination of the longitudinal and shear bulk attenuations and the first energy factor calculated by neglecting the material absorption in the viscoelastic coating.

These results have been submitted for publication [P4 P5 P6].

9.3 Feasibility of long range inspections

As discussed in Chapters 3 and 4, in the case of large material damping, the modes with the lowest guided wave attenuation are SH_0 and the Lamb mode $\bar{M}_1$. The universal curves derived in Chapter 5 contain all the information needed for identifying the frequencies which maximise the inspection range, as a function of the bilayer acoustic and geometrical properties.

Where maxima in the attenuation spectra of SH_0 and $\bar{M}_1$ occur, long range inspections are never possible due to the large decay of the guided wave with propagation distance. These frequencies mainly depend on the thickness and the shear or longitudinal bulk velocities of the coating (see universal curves in Chapter 5). The first attenuation peak of both SH_0 and $\bar{M}_1$ occurs at a critical frequency which is proportional to the ratio between the shear velocity and thickness of the coating. Long range tests are possible before and immediately after this frequency as the attenuation drops down. In these regions, for a prescribed value of the frequency, the guided wave attenuation decreases almost linearly with the thickness-impedance product of the metallic plate, and increases linearly with shear bulk attenuation-impedance product of the viscoelastic layer. Moreover the attenuation of SH_0 is always larger than that of $\bar{M}_1$. Therefore, guided waves propagate for a large distance in pipeline with thick wall and thin coatings. On the other hand, when the coating is thick, the first critical frequency is low and in order to limit the guided wave attenuation, the testing frequency has to be very low. However, there are practical constraints, such as signal time resolution, which limit the lower value of the testing frequency to around 10kHz. As a consequence, if the coating is too thick the only possibility is to perform tests at frequencies higher than the first critical frequency (see universal curves). It has to be noticed that while below the first critical frequency the $\bar{M}_1$ mode is less attenuated than SH_0, around first Love transition frequency the SH_0 mode is more attractive, due to the presence of the second attenuation maximum of $\bar{M}_1$ (see Chapter 6).

The shear acoustic properties of the coating have a dominant role on the guided wave attenuation. Coatings with low shear velocity and large shear attenuation

increase the guided wave attenuation dramatically. For this kind of coating, the only possibility is to use the SH_0 mode around the first Love transition frequency. On the other hand, coatings with high shear velocity and low shear damping allow guided waves to propagate for longer distances. Unfortunately, the shear properties of viscoelastic materials are extremely variable because of environmental factors, such temperature and oxidation phenomena. As a result, even for a given type of coating such as bitumen, is not possible to predict the guided wave attenuation, unless in-situ measurement of the coating properties are performed. This can be done with the technique presented in Chapter 8.

The universal curves will be submitted for publication [P8].

9.4 Methods for material characterisation

Two novel techniques for the characterisation of the acoustic properties of viscoelastic fluids and solids were presented in Chapters 7 and 8, respectively.

For highly attenuative fluid materials, the shear properties can be evaluated from the dispersion curves of the fundamental torsional mode, T(0,1), propagating in a metallic tube filled with the material to be characterised. The presence of the attenuative core modifies the phase velocity dispersion curve of the T(0,1) mode propagating in the empty tube. Moreover, while the T(0,1) mode propagates without being attenuated in the empty tube (due to the negligible absorption in metals at the low frequencies used), the viscoelastic inner core causes a strong damping of the guided mode. As a consequence, the guided wave attenuation and the phase velocity variations, which are induced by the inner core, allow the properties of the viscoelastic core to be derived. This technique overcomes several of the disadvantages of traditional ultrasonic techniques such beam spreading, transducer coupling and geometry control of the sample. Moreover, this method represents the best alternative for the characterisation of highly attenuative material since in this case traditional methods cannot be employed as bulk waves are completely absorbed by

the material. The main feature of the method is that the geometry of the metallic tube (radius and wall thickness) can be tailored to the core properties in order to have a full control of the magnitude of the guided wave attenuation. The dependence of the guided wave attenuation on the tube geometry is based on the same physics which relates the attenuation dispersion of SH_0 to the bilayer geometry. In this context, a correspondence between the tube wall and the metallic plate thicknesses and the tube inner radius and the coating thickness can be set. As an example, the value of the guided wave attenuation can be reduced by increasing the tube wall thickness. This method has been published in [P1].

In Chapter 8 it was shown that the shear properties of a solid viscoelastic material can be derived from either the reflection or transmission coefficient spectra of the fundamental torsional mode through a sample of the material clamped between two rods. Since the sample is just clamped between the rods and neither glue nor couplant is used, the technique is rapid and ideal for in-situ measurements of the coating shear properties. This technique has been published in [P2 P3].

9.5   Future work

A possible future application of the knowledge gained on the guided wave propagation in attenuative bilayers could be the detection of blockages in pipelines. Precipitation of paraffins and asphaltenes in crude oil transportation and processing pipelines may cause deposition which leads to the plugging of the pipeline and severe pumping problems. As a result, a NDT technique able to locate and estimate the thickness of the deposition would be extremely beneficial.

One possibility would be the measurement of the guided wave attenuation spectrum of either the fundamental torsional mode propagating along the pipeline or the SH_0 mode propagating around the pipe circumference [19]. If the deposition thickness were uniform around the pipe circumference, by measuring the frequency where the first guided wave attenuation maximum occurs, the thickness of the deposition could

be derived from the simple expression (4.23), provided the shear velocity of the deposit is known in advance (for instance, by using one of the techniques developed in this thesis).

However, due to gravity, the deposition occurs mainly on the bottom of the pipe, leading to a non axisymmetric geometry of the waveguide (pipe plus deposit). As a consequence, the propagating modes are also non axisymmetric and pure torsional and longitudinal modes no longer exist. Nevertheless, the resonance phenomenon which leads to maxima in the attenuation spectrum of SH_0 should still exist in the non axisymmetric case. If so, it should be possible to relate the resonance frequency to the acoustic properties of the deposit and its geometry.

A further difficulty arises from the limited axial and circumferential extents of the blockage, which cause the scattering of the incident guided mode. The scattering, might result in a number of transmitted and reflected modes due to the mode conversion phenomenon which occurs where the guided mode impinges the deposit. Since the energy of the incident mode is distributed among all the scattered modes, the signal amplitude decays, resulting in an apparent attenuation which superimposes on the energy dissipation in the viscoelastic layer. Therefore, in order to separate the apparent attenuation from the attenuation due to the material absorption, which can be related to the size of the blockage, it is crucial to study and characterise the scattering phenomenon.

Appendix A

Energy factors at low frequency

In order to show the validity of the inequality $Q_E > Q_\Gamma > Q_\Delta$ in zone A (see Fig. 5.2), let us consider the limit case as the frequency approaches zero. For both SH and Lamb waves, the displacement field tends to be constant across the thickness of the bilayer (i.e. $h_2(x_3) = \bar{h}_2$ and $h_1(x_3) = \bar{h}_1$ see eqs (3.5) and (4.2)). For SH waves, the only non zero strain is ε_{12} and the peak strain energy in the equivalent viscoelastic layer can be obtained by substituting the displacement expression (3.5) into ε_{12} and integrating (3.10) over the viscoelastic layer thickness

$$\frac{dE}{dx} = \frac{1}{2}\tilde{\mu}_r^v d_v \xi^2 \bar{h}_2^2. \tag{A.1}$$

The in-plane power flow is obtained by integrating the real part of the Poynting vector component along $\hat{x}_1$ over the thickness

$$< P > = \frac{1}{2}\omega(\tilde{\mu}_r^e d_e + \tilde{\mu}_r^v d_v)\xi \bar{h}_2^2, \tag{A.2}$$

thus, by the definition of Q_E (3.15)

$$Q_E = \frac{1}{c_{ph}}\frac{\tilde{\mu}_r^v d_v}{\tilde{\mu}_r^v d_v + \tilde{\mu}_r^e d_e}, \tag{A.3}$$

where the phase velocity can be obtained by considering the propagation of a plane wave along the bilayer

$$c_{ph}^2 = \frac{\tilde{\mu}_r^v d_v + \tilde{\mu}_r^e d_e}{\rho_v d_v + \rho_e d_e}. \tag{A.4}$$

If $\tilde{\mu}_r^v d_v / \tilde{\mu}_r^e d_e \ll 1$, the expression (A.3) in the first order approximation, takes the form

$$Q_E \simeq \frac{1}{c_{ph}}\frac{\tilde{\mu}_r^v d_v}{\tilde{\mu}_r^e d_e}. \tag{A.5}$$

In the case of Lamb waves the traction free condition at the two boundaries of the bilayer implies that the stresses σ_{33} and σ_{31} are negligible compared to σ_{11} and σ_{22} across the thickness. Under this hypothesis, from the consitutive equations (2.7) the strain tensor components are

$$\varepsilon_{33} = -\frac{\tilde{\lambda}_r^v}{\tilde{\lambda}_r^v + 2\tilde{\mu}_r^v}\varepsilon_{11}, \tag{A.6}$$

$$\varepsilon_{31} = 0, \tag{A.7}$$

in which (A.6) takes into account the Poisson effect for plane strain deformation. The strain ε_{11} is derived from the displacement (4.2) with $h_1(x_3) = \bar{h}_1$. By substituting the strains (A.6) and (A.7) into (4.11) and (4.12) and integrating the expressions so obtained over the viscoelastic layer thickness, one obtains

$$\frac{d\Delta}{dx} = \tilde{\mu}_r^v \frac{2\tilde{\mu}_r^v d_v}{\tilde{\lambda}_r^v + 2\tilde{\mu}_r^v}\xi^2\bar{h}_1^2, \tag{A.8}$$

$$\frac{d\Gamma}{dx} = \tilde{\lambda}_r^v \frac{2\tilde{\mu}_r^v d_v}{\tilde{\lambda}_r^v + 2\tilde{\mu}_r^v}\xi^2\bar{h}_1^2. \tag{A.9}$$

The in-plane power flow is

$$< P > = 2\omega\left(\tilde{\mu}_r^e d_e \frac{\tilde{\lambda}_r^e + \tilde{\mu}_r^e}{\tilde{\lambda}_r^e + 2\tilde{\mu}_r^e} + \tilde{\mu}_r^v d_v \frac{\tilde{\lambda}_r^v + \tilde{\mu}_r^v}{\tilde{\lambda}_r^v + 2\tilde{\mu}_r^v}\right)\xi\bar{h}_1^2, \tag{A.10}$$

and

$$Q_\Delta = \frac{1}{c_{ph}}\frac{\tilde{\mu}_r^v \frac{\tilde{\mu}_r^v d_v}{\tilde{\lambda}_r^v + 2\tilde{\mu}_r^v}}{\left(\tilde{\mu}_r^e d_e \frac{\tilde{\lambda}_r^e + \tilde{\mu}_r^e}{\tilde{\lambda}_r^e + 2\tilde{\mu}_r^e} + \tilde{\mu}_r^v d_v \frac{\tilde{\lambda}_r^v + \tilde{\mu}_r^v}{\tilde{\lambda}_r^v + 2\tilde{\mu}_r^v}\right)}, \tag{A.11}$$

where the phase velocity is given by

$$c_{ph}^2 = 4\frac{\left(\tilde{\mu}_r^e d_e \frac{\tilde{\lambda}_r^e + \tilde{\mu}_r^e}{\tilde{\lambda}_r^e + 2\tilde{\mu}_r^e} + \tilde{\mu}_r^v d_v \frac{\tilde{\lambda}_r^v + \tilde{\mu}_r^v}{\tilde{\lambda}_r^v + 2\tilde{\mu}_r^v}\right)}{\rho_e d_e + \rho_v d_v}. \tag{A.12}$$

Relationship (A.11), in the first order approximation, provides

$$Q_\Delta \simeq \tilde{\mu}_r^v \frac{1}{c_{ph}}\frac{\tilde{\mu}_r^v d_v}{\tilde{\mu}_r^e d_e}\frac{\tilde{\lambda}_r^e + 2\tilde{\mu}_r^e}{(\tilde{\lambda}_r^e + \tilde{\mu}_r^e)(\tilde{\lambda}_r^v + 2\tilde{\mu}_r^v)}, \tag{A.13}$$

and similarly

$$Q_\Gamma \simeq \tilde{\lambda}_r^v \frac{1}{c_{ph}}\frac{\tilde{\mu}_r^v d_v}{\tilde{\mu}_r^e d_e}\frac{\tilde{\lambda}_r^e + 2\tilde{\mu}_r^e}{(\tilde{\lambda}_r^e + \tilde{\mu}_r^e)(\tilde{\lambda}_r^v + 2\tilde{\mu}_r^v)}. \tag{A.14}$$

As a consequence, by taking the ratio of (A.14) to (A.13)

$$\frac{Q_\Gamma}{Q_\Delta} \simeq \frac{\tilde{\lambda}_r^v}{\tilde{\mu}_r^v}, \tag{A.15}$$

which proves that, at low frequencies, $Q_\Gamma \gg Q_\Delta$. It is interesting to note that, although in zone A for a Lamb mode the amplitude of the longitudinal partial waves is larger than that of the shear partial waves, Q_Γ is larger than Q_Δ as the γ energy depends on both longitudinal and shear bulk waves as explained in sec. 4.3.

The comparison between Q_Γ and Q_E leads to

$$\frac{Q_E}{Q_\Gamma} \simeq \frac{c_{ph}^{Lamb}}{c_{ph}^{SH}} \frac{(\tilde{\lambda}_r^e + \tilde{\mu}_r^e)(\tilde{\lambda}_r^v + 2\tilde{\mu}_r^v)}{\tilde{\lambda}_r^v(\tilde{\lambda}_r^e + 2\tilde{\mu}_r^e)}. \tag{A.16}$$

Moreover, for $\tilde{\mu}_r^v d_v / \tilde{\mu}_r^e d_e \ll 1$

$$\frac{Q_E}{Q_\Gamma} \simeq 2\left(\frac{\tilde{\lambda}_r^e + \tilde{\mu}_r^e}{\tilde{\lambda}_r^e + 2\tilde{\mu}_r^e}\right)^{\frac{3}{2}} \left(1 + 2\frac{\tilde{\mu}_r^v}{\tilde{\lambda}_r^v}\right), \tag{A.17}$$

which, when the metal considered is steel, gives

$$\frac{Q_E}{Q_\Gamma} \simeq 1 + 2\frac{\tilde{\mu}_r^v}{\tilde{\lambda}_r^v}. \tag{A.18}$$

It can be concluded that, in the zone A (Fig. 5.2), $Q_E > Q_\Gamma > Q_\Delta$. Moreover, from (3.39) and (4.20) it follows that SH modes are more attenuated than Lamb waves.

Appendix B

Scattering of torsional waves

This appendix studies the scattering of a torsional mode, $T(0, N)$, by a disk rigidly clamped between two identical rods and demonstrates that torsional modes do not undergo mode conversion, as would happen for longitudinal modes propagating above the cutoff frequency of the second longitudinal mode. The scattering of $T(0, 1)$ will be considered first.

The displacement field of the $T(0, 1)$ mode propagating in a viscoelastic homogeneous and isotropic infinite long rod can be written according to [36]

$$u_\theta = A_1 r e^{-ik_z z}, \tag{B.1}$$

where k_z is given by

$$k_z = \frac{\omega}{a_s}, \tag{B.2}$$

where a_s is the complex shear velocity of the material. When two different rods, 1 and 2, with the same diameter are rigidly bonded together forming a single infinitely long rod, the $T(0, 1)$ mode travelling along the rod 1 is scattered at the interface between the two rods. Let us assume that the $T(0, 1)$ mode is scattered in a transmitted and a reflected wave only, the displacement fields of the incident, reflected and transmitted waves being

$$u_I = r A_I e^{-ik_{1z} z}, \tag{B.3}$$

$$u_R = r A_R e^{ik_{1z} z}, \tag{B.4}$$

$$u_T = r A_T e^{-ik_{2z} z}. \tag{B.5}$$

On the other hand, the stress fields over the plane $z = 0$, $\tau_{z\theta}$, are

$$\tau_I = -i\tilde{\mu}_1 k_{1z} r A_I e^{-ik_{1z}z}, \tag{B.6}$$

$$\tau_R = i\tilde{\mu}_1 k_{1z} r A_R e^{ik_{1z}z}, \tag{B.7}$$

$$\tau_T = -i\tilde{\mu}_2 k_{2z} r A_T e^{-ik_{2z}z}. \tag{B.8}$$

The continuity of the displacement and stress at the interface between the two rods requires that

$$u_I + u_R = u_T, \tag{B.9}$$

$$\tau_I + \tau_R = \tau_T, \tag{B.10}$$

which lead to a system of two equations in the unknown amplitudes A_R and A_T

$$A_I + A_R = A_T, \tag{B.11}$$

$$\tilde{\mu}_1 k_{1z}(A_I - A_R) = \tilde{\mu}_2 k_{2z} A_T. \tag{B.12}$$

Such a system is identical to that describing the scattering of plane shear horizontal waves at the interface between two different media [31]. Therefore, R_{12} and T_{12} are still provided by (8.4) and (8.5). It is worth emphasizing that the existence of the solution to the system (B.11) (B.12) implies that the $T(0,1)$ mode does not undergo mode conversion [i.e. $T(0,1)$ is scattered in the $T(0,1)$ mode only] at the interface between the two rods. This contrasts with $L(0,1)$ where mode conversion to $L(0,2)$ and higher order modes can occur above their cutoff frequencies.

Let us now consider the case of a disk of thickness d rigidly clamped between two identical rods of infinite length. When $T(0,1)$ impinges on the disk, it undergoes infinite reflections as in the case of plane waves. Moreover, since the interface reflection and transmission coefficients, R_{ij} and T_{ij}, of $T(0,1)$ are the same as those of shear plane waves, the total reflection and transmission coefficients are still given by (8.6) and (8.7). As a result, the shear properties of a disk clamped between two rods can be obtained by measuring the reflection and transmission coefficients of the fundamental torsional mode following the procedure discussed in Sec. 8.3.

The previous demonstration can be extended to case of higher order modes, by observing that the displacement field of a $T(0,N)$ mode can be written according

to (7.2)

$$u_\theta = A_1 J_1(k_{\hat{r}}r)e^{-ik_z z}, \tag{B.13}$$

where the second kind Bessel function, Y_0, has been discarded since it is singular for $r = 0$. k_z is now the projection of the wavenumber along $\hat{z}$ (complex) whereas $k_{\hat{r}}$ is the wavenumber projection along $\hat{r}$. The secular equation describing the propagation of torsional modes in rods can be found by imposing the zero traction condition along the lateral surface of the rod. As a consequence, by substituting (B.13) into (7.3) one obtains [36]

$$k_{\hat{r}}r_0 J_0(k_{\hat{r}}r_0) = 2J_1(k_{\hat{r}}r_0), \tag{B.14}$$

where r_0 is the rod radius. Eq. (B.14) admits infinite solutions, each of them corresponding to a single mode. Moreover, for a given mode, since eq. (B.14) does not involve the material properties of the rod, $k_{\hat{r}}$ depends on the rod radius only.

Consider the scattering of $T(0, N)$ at the interface between two rods. In a similar fashion to the case of $T(0, 1)$ let us assume that the $T(0, N)$ mode is scattered in a transmitted and a reflected wave only, the displacement fields of the incident, reflected and transmitted waves being

$$u_I = J_1(k_{\hat{r}}r)A_I e^{-ik_{1z}z}, \tag{B.15}$$

$$u_R = J_1(k_{\hat{r}}r)A_R e^{ik_{1z}z}, \tag{B.16}$$

$$u_T = J_1(k_{\hat{r}}r)A_T e^{-ik_{2z}z}. \tag{B.17}$$

On the other hand, the stress fields over the plane $z = 0$, $\tau_{z\theta}$, are

$$\tau_I = -i\tilde{\mu}_1 k_{1z} J_1(k_{\hat{r}}r)A_I e^{-ik_{1z}z}, \tag{B.18}$$

$$\tau_R = i\tilde{\mu}_1 k_{1z} J_1(k_{\hat{r}}r)A_R e^{ik_{1z}z}, \tag{B.19}$$

$$\tau_T = -i\tilde{\mu}_2 k_{2z} J_1(k_{\hat{r}}r)A_T e^{-ik_{2z}z}. \tag{B.20}$$

Note that $k_{\hat{r}}$ is an invariant for the two rods, provided the radii of the two rods and the mode order are the same. The continuity of stress and displacement at the interface between the rods leads to the system (B.11) and (B.12), where k_z is now the projection of the wavenumber along the rod axis.

By introducing the generalized impedance χ

$$\chi = \frac{\tilde{\mu} k_z}{\omega}, \tag{B.21}$$

the stress reflection and transmission coefficients can be obtained by solving the system (B.11) (B.12) i.e.

$$R_{12} = \frac{\chi_2 - \chi_1}{\chi_1 + \chi_2}, \tag{B.22}$$

$$T_{12} = \frac{2\chi_2}{\chi_1 + \chi_2}. \tag{B.23}$$

The existence of this solution proves that the assumption that a $T(0, N)$ mode is scattered in a transmitted and reflected waves which have the same order as the incident wave is valid. In other words, the $T(0, N)$ mode does not undergo mode conversion.

References

[1] R. L. Weaver and Y. Pao. Axisymmetric elastic waves excited by a point source in a plate. *Journal of Applied Mechanics*, 49:821–836, 1982.

[2] M. G. Silk and K. F. Bainton. The propagation in metal tubing of ultrasonic wave modes equivalent to lamb waves. *Ultrasonics*, 17(1):11–19, 1979.

[3] W. Bottger, H. Schneider, and W. Weingarten. Prototype emat system for tube inspection with guided ultrasonic waves. *Nuclear Eng. Design*, 102:356–376, 1987.

[4] J.L. Rose, J.J. Ditri, A. Pilarski, K. Rajana, and F. Carr. A guided wave inspection technique for nuclear steam generator tubing. *NDT & E Int.*, 27:307–310, 1994.

[5] W. Mohr and P. Holler. On inspection of thin-walled tubes for transverse and longitudinal flaws by guided ultrasonic waves. *IEEE Trans. Sonics Ultrason.*, SU-23:369–378, 1976.

[6] D. N. Alleyne and P. Cawley. The interaction of lamb waves with defects. *IEEE Trans. Ultrason. Ferroelectr. Freq. Control*, 39:381–397, 1992.

[7] D. N. Alleyne and P. Cawley. The excitation of lamb waves in pipes using dry coupled piezoelectric transducers. *J NDE*, 15:11–20, 1996.

[8] D. N. Alleyne and P. Cawley. Long range propagation of lamb waves in chemical plant pipework. *Material Evaluation*, 55:504–508, 1997.

[9] D. N. Alleyne, M. J. S. Lowe, and P. Cawley. The reflection of guided waves from circumferential notches in pipes. *Journal of Applied Mechanics*, 65:635–641, 1998.

[10] M. J. S. Lowe, D. N. Alleyne, and P. Cawley. The mode conversion of a guided wave by a part-circumferential notch in a pipe. *Journal of Applied Mechanics*, 65:649–656, 1998.

[11] P. Cawley, M. J. S Lowe, F. Simonetti, C. Chevalier, and A. G. Roosenbrand. The variation of the reflection coefficient of extensional guided waves in pipes from defects as a function of defect depth, axial extent, circumferential extent and frequency. *Journal of Mechanical Engineering Science*, 216(C):1131–1143, 2002.

[12] P. Fromme, P. Wilcox, and P. Cawley. Remote monitoring of plate-like structures using guided wave arrays. In D. O. Thompson and D. E. Chimenti, editors, *Review of Progress in Quantitative NDE*, volume 22A, pages 157–164, 2002.

[13] P. Wilcox. Guided wave beam steering and modal selectivity from omni-directional transducer arrays. In D. O. Thompson and D. E. Chimenti, editors, *Review of Progress in Quantitative NDE*, volume 22A, pages 761–768, 2002.

[14] O. Diligent, T. Grahn, A. Boström, P. Cawley, and M. Lowe. The low-frequency reflection and scattering of the s_0 lamb mode from a circular through-thickness hole in a plate: Finite element, analytical and experimental studies. *Journal of the Acoustical Society of America*, page under press, 2002.

[15] A. Demma, P. Cawley, M. Lowe, and A. G Roosenbrand. The reflection of fundamental torsional mode from cracks and notches in pipes. *Submitted to Journal of the Acoustical Society of America*, 2000.

[16] T. Kundu. Scattering of torsional waves by a circular crack in a transversely isotropic solid. *Journal of the Acoustical Society of America*, 88(4):1975–1980, 1990.

[17] D. N. Alleyne, B. Pavlakovic, M. J. S. Lowe, and P. Cawley. Rapid, long range inspection of chemical plant pipework using guided waves. *Insight*, 43:93–96,101, 2001.

[18] P. Cawley, M. J. S Lowe, D. N Alleyne, B. Pavlakovic, and P. Wilcox. Practical long range guided wave testing: application to pipes and rail. *Material Evaluation*, 61(1):66–74, 2003.

[19] D. Gridin, R. V. Craster, J. Fong, M. Lowe, and M. Beard. The high-frequency asymptotic analysis of guided waves in a circular elastic annulus. *Wave Motions*, 38:67–90, 2003.

[20] J. P. Jones. Wave propagation in a two-layered medium. *Journal of Applied Mechanics*, 31(2):213–222, 1964.

[21] J. Laperre and W. Thys. Experimental and theoretical study of lamb wave dispersion in aluminium / polymer bilayers. *Journal of the Acoustical Society of America*, 94(1):268–278, 1993.

[22] Z. Zhu and J. Wu. The propagation of lamb waves in a plate bordered with a viscous liquid. *Journal of the Acoustical Society of America*, 98:1057–1064, 1995.

[23] C. L. Yapura and V. K. Kinra. Guided waves in a fluid-solid bilayer. *Wave motion*, 21:35–46, 1995.

[24] A. H. Nayfeh and P. B. Nagy. The interaction of lamb waves with defects. *Journal of the Acoustical Society of America*, 101(5):2649–2658, 1997.

[25] R. M. Christensen. *Theory of viscoelasticity: an introduction.* Academic Press, New York, London, 1971.

[26] Y. M. Haddad. *Viscoelasticity of engineering materials.* Chapman and Hall, New York, London, 1995.

[27] P. M. Morse and H. Feshbach. *Methods of theoretical physics.* McGraw-Hill Book Company, New York, London, 1953.

[28] B. A. Auld. *Acoustic Fields and Waves in Solids*, volume 1. Krieger Publishing Company, Malabar, Florida, 1990.

[29] A. H. Nayfeh. *Wave propagation in layered anisotropic media with application to composites.* Elsevier, Amsterdam, 1995.

[30] M. J. S. Lowe. Matrix techniques for modelling ultrasonic waves in multi-layered media. *IEEE Trans. Ultrason. Ferroelectr. Freq. Control*, 42:525–542, 1995.

[31] B. A. Auld. *Acoustic Fields and Waves in Solids*, volume 2. Krieger Publishing Company, Malabar, Florida, 1990.

[32] M. O'Donnell, E. T. Jaynes, and J. G. Miller. Kramers-kronig relationship between ultrasonic attenuation and phase velocity. *Journal of Applied Mechanics*, 69(3):696–701, 1981.

[33] A. H. Nayfeh. The propagation of horizontally polarized waves in multilayered anisotropic media. *Journal of the Acoustical Society of America*, 86(5):2000–2012, 1989.

[34] B. N. Pavlakovic, M. J. S. Lowe, D. N. Alleyne, and P. Cawley. Disperse: A general purpose program for creating dispersion curves. In D. O. Thompson and D. E. Chimenti, editors, *Review of Progress in Quantitative NDE*, volume 16, pages 185–192. Plenum Press, New York, 1997.

[35] J. L. Rose. *Ultrasonic Waves in Solid Media*. Cambridge University Press, Cambridge, UK, 1999.

[36] K. F. Graff. *Wave motion in elastic solids*. Clarendon Press, Oxford, 1975.

[37] R. Vein and P. Dale. *Determinants and their applications in mathematical physics*. Springer, New York, Berlin, 1999.

[38] H. Überall, B. Hosten, M. Deschamps, and A. Gérard. Repulsion of phase-velocity dispersion curves and the nature of plate vibration. *Journal of the Acoustical Society of America*, 92(2):908–917, 1994.

[39] A. H. Nayfeh and D. E. Chimenti. Propagation of guided waves in fluid-coupled plates of fiber-reinforced composite. *Journal of the Acoustical Society of America*, 83(5):1736–1742, 1988.

[40] S. I. Rohklin, D. E. Chimenti, and A. H. and Nayfeh. On the topology of the complex wave spectrum in a fluid-coupled elastic layer. *Journal of the Acoustical Society of America*, 85(3):1074–1080, 1989.

[41] H. Dabirikhah and C. W. Turner. The coupling of the a_0 and interface scholte modes in fluid loaded plates. *Journal of the Acoustical Society of America*, 100:3442, 1996.

[42] P. B. Nagy. Longitudinal guided waves propagation in a transversely isotropic rod immersed in fluid. *Journal of the Acoustical Society of America*, 98(1):454–457, 1995.

[43] L. M. Brekhovskikh. *Waves in layered media*. Academic Press, New York, London, 1980.

[44] A. Bernard, M. J. S. Lowe, and M. Deschamps. Guided waves energy velocity in absorbing and non-absorbing plates. *Journal of the Acoustical Society of America*, 110(1):186–196, 2001.

[45] C.W. Chan and P. Cawley. Lamb waves in highly attenuative plastic plates. *Journal of the Acoustical Society of America*, 104(2):874–881, 1998.

[46] Lord Rayleigh. On the free vibrations of an infinite plate of homogeneous isotropic elastic matter. *Proceedings London Mathematical Society*, 20(357):225–237, 1888-1889.

[47] H. Lamb. On the flexure of an elastic plate. *Proceedings London Mathematical Society*, 21:85, 1889-1890.

[48] H. Lamb. On waves in an elastic plate. *Proceedings Royal Society*, 93:114–128, 1916-1917.

[49] R. D. Fay and O. V. Fortier. Transmission of sound through steel plates immersed in water. *Journal of the Acoustical Society of America*, 23(3):339–346, 1951.

[50] R. H. Lyon. Response of an elastic plate to localized driving forces. *Journal of the Acoustical Society of America*, 27(2):259–265, 1955.

[51] R. D. Mindlin. Vibrations of an infinite elastic plate at its cutoff frequencies. *Proc. Third U.S. National Congress of Applied Mechanics*, page 225, 1958.

[52] R. D. Mindlin and M. Onoe. Mathematica theory of vibrations of elastic plates. In *Proceedings of the Eleventh Annual Symposium of Frequency Control*, pages 17–40. U.S. Army Signal Engineering Laboratories, New Jersey, 1957.

[53] R. D. Mindlin and M. A. Medick. Extensional vibrations of elastic plates. *Journal of Applied Mechanics*, 26:561–569, 1959.

[54] R. D. Mindlin. Waves and vibrations in isotropic, elastic plates. In J. N. Goodier and N. J. Hoff, editors, *Structural Mechanics*, pages 199–232. Pergamon Press, New York, 1960.

[55] W. B. Fraser. Orthogonality relation for the rayleigh-lamb modes of vibration of a plate. *Journal of the Acoustical Society of America*, 59(1):215–216, 1976.

[56] C. Scandrett and N. Vasudevan. The propagation of time harmonic rayleigh-lamb in a bimaterial plate. *Journal of the Acoustical Society of America*, 89(4):1606–1614, 1991.

[57] Lord Rayleigh. *The theory of sound*, volume 1. Dover, New York, 1945.

[58] E. L. Bolda, R. Y. Chiao, and J. C. Garrison. Two theorems for the group velocity in dispersive media. *Physical Review*, 48(5):3890–3894, 1993.

[59] K. Suchy. Real hamilton equations of geometrical optics for media with moderate absorption. *Radio Science*, 16:1179–1182, 1981.

[60] D. Censor. Alternative methods for ray propagation in absorbing media. *Proc. of IEEE*, 69:750–751, 1981.

[61] I. Gurwich. On the pulse velocity in absorbing and non-linear media and parallels with the quantum mechanics. *Progress In Electromagnetics Research*, 33:69–96, 2001.

[62] C. G. B. Garrett and D. E. McCumber. Propagation of gaussian light pulse through an anomalous dispersion medium. *Physical Review A*, 1(2):305–313, 1970.

[63] S. Chu and Wong S. Linear pulse propagation in an absorbing medium. *Physical review letters*, 48(11):738–741, 1982.

[64] M. A. Biot. General theorems on the equivalence of group velocity and energy transport. *Physical Review*, 105(4):1129–1137, 1957.

[65] I. Tolstoy and E. Usdin. Wave propagation in elastic plates: low and high mode dispersion. *Journal of the Acoustical Society of America*, 29(1):37–42, 1956.

[66] A. H. Meitzler. Backward-wave transmission of stress pulses in elastic cylinders and plates. *Journal of the Acoustical Society of America*, 38:835–842, 1965.

[67] J. Wolf, T. D. K. Ngoc, R. Kille, and W. G. Mayer. Investigation of lamb waves having a negative group velocity. *Journal of the Acoustical Society of America*, 83(1):122–126, 1988.

[68] D. Eidus. The limiting absorption principle. *Russian Mathematical Surveys*, 24:97–167, 1969.

[69] D. K. Mak. Comparison of various methods for the measurement of reflection coefficient and ultrasonic attenuation. *British Journal of NDT*, 33(9):441–449, 1991.

[70] D. K. Mak. Ultrasonic phase velocity measurement incorporating couplant correction. *British Journal of NDT*, 35(8):443–449, 1993.

[71] R. E. Challis, G. P. Wilkinson, and Freemantle R. J. Errors and uncertainties in the ultrasonic pulse-echo reflectometry method for measuring acoustic impedance. *Measurement Science Technology*, 9:692–700, 1998.

[72] M. Castaings, B. Hosten, and T. Kundu. Inversion of ultrasonic, plane-wave transmission data in composite plates to infer viscoelastic material properties. *NDT and E Internetional*, 33:377–392, 2000.

[73] A. Di Meglio and L. S. Wang. A variational method for identification of viscoelastic parameters from experimental data. *Journal of the Acoustical Society of America*, 6(108):2476–2753, 2000.

[74] T. Pialucha, C. C. H. Guyott, and P. Cawley. Amplitude spectrum method for the measurement of phase velocity. *Ultrasonics*, 27(9):270–279, 1989.

[75] N. Guo, M. K. Lim, and T. Pialucha. Measurement of the attenuation using a normalized amplitude spectrum. *Journal of Nondestructive Evaluation*, 14(1):9–19, 1995.

[76] W. Sachse and Y. H. Pao. On the determination of phase and group velocities of dispersive waves in solids. *Journal of Applied Physics*, 49:4320–4327, 1978.

[77] P. Kielczynski and R. Plowiec. Determination of the shear impedance of viscoelastic liquids using love and bleustein-gulyaev surface waves. *Journal of the Acoustical Society of America*, 86(2):818–827, 1989.

[78] J. O. Kim, Y. Wang, and H. H. Bau. The effect of an adjacent viscous fluid on the transmission of torsional stress waves in a submerged waveguide. *Journal of the Acoustical Society of America*, 89(3):1414–1422, 1991.

[79] T. Vogt, M.J.S. Lowe, and P. Cawley. Ultrasonic waveguide techniques for the measurement of material properties. In D. O. Thompson and D. E. Chimenti, editors, *Review of Progress in Quantitative NDE*, volume 21, pages 1742–1749. American Institue of Physics, New York, 2002.

[80] D. C. Gazis. Three dimensional investigation of the propagation of waves in hollow circular cylinders. *Journal of the Acoustical Society of America*, 31(5):568–578, 1959.

[81] G. N. Watson. *The theory of Bessel Functions*. Cambridge, London, New York, 1952.

[82] J. Vollman and J. Dual. High-resolution analysis of the complex wave spectrum in a cylindrical shell containing a viscoelastic medium. part i. theory and numerical results. *Journal of the Acoustical Society of America*, 102(2):896–908, 1997.

[83] J. Vollman, R. Breu, and J. Dual. High-resolution analysis of the complex wave spectrum in a cylindrical shell containing a viscoelastic medium. part

ii. experimental results versus theory. *Journal of the Acoustical Society of America*, 102(2):909–920, 1997.

[84] R. B. Randall. *Frequency analysis.* Brüel & Kjaer, Nærum, Denmark, 1987.

[85] B. Hartmann, G. F. Lee, and J. D. Lee. Loss factors height and with limits for polymer relaxations. *Journal of the Acoustical Society of America*, 95(1):226–233, 1994.

[86] R. C. Williamson and D. Eden. Coherent detection technique for variable-path-length measurements of ultrasonic pulses. *Journal of the Acoustical Society of America*, 47(5):1278–1281, 1970.

[87] K. W. Katahara, C. S. Rai, M. H. Manghnani, and J. Balogh. An interferometric technique for measuring velocity and attenuation in molten rocks. *Journal of Geophysical Research*, 86(B12):11779–11786, 1981.

[88] M. L. Rivers and S. E. Carmichael. Ultrasonic studies of silicate melts. *Journal of Geophysical Research*, 92(B9):9247–9270, 1987.

[89] R. A. Secco, M. H. Manghnani, and T. Liu. Velocities and compressibility of komatiitic melts. *Geophysical Research Letters*, 18(8):1397–1400, 1991.

[90] P. M. Nasch, M. H. Manghnani, and R. A. Secco. A modified ultrasonic interferometer for sound velocity measurements in molten metals and alloys. *Review of Scientific Instruments*, 65(3):682–688, 1993.

[91] N. Yoshimoto, M. Ikeda, M. Yoshizawa, and S. Kimura. Sound velocity of molten silicon. *Physica B*, 219-220:623–625, 1996.

[92] J. kushibiki, N. Akashi, T. Sannomiya, N. Chubachi, and F. Dunn. Vhf/uhf range bioultrasonic spectroscopy system and method. *IEEE Trans. Ultrason. Ferroelect. Freq. Cont.*, 42(6):1028–1039, 1995.

[93] N. Akashi, J. Kushibiki, and F. Dunn. Acoustic properties of egg yolk and albumen in the frequency range 20-400 mhz. *Journal of the Acoustical Society of America*, 102(6):3774–3778, 1997.

[94] J. D. Ferry. *Viscoelastic properties of polymers*. Wiley, New York, 1980.

[95] J. L. Buchanan. Numerical solution for the dynamic moduli of a viscoelastic bar. *Journal of the Acoustical Society of America*, 81(6):1775–1786, 1987.

[96] S. L. Garrett. Resonant acoustic determination of elastic moduli. *Journal of the Acoustical Society of America*, 88(1):210–221, 1990.

[97] R. D. Adams and J. Coppendale. Measurement of the elastic moduli of structural adhesives by a resonant bar technique. *Journal Mechanical Engineering Science*, 18(3):149–158, 1976.

[98] B. G. Ferguson. Calculation of the loss tangent for viscoelastic materials using the triple-bar composite resonance technique. *Journal of the Acoustical Society of America*, 76(5):1577–1579, 1984.

[99] H. G. Tattersall. The ultrasonic pulse-echo technique as applied to adhesion testing. *J. Phys. D Appl. Phys.*, 6:819–832, 1973.

[100] M. Schoenberg. Elastic wave behaviour across linear slip interfaces. *Journal of the Acoustical Society of America*, 68(5):1516–1521, 1980.

[101] M. D. Verweij and H. Chapman. Transmission and reflection of transient elastodynamic waves at a linear slip interface. *Journal of the Acoustical Society of America*, 101(5):2473–2484, 1996.

[102] B. Drinkwater, R. Dwyer-Joyce, and P. Cawley. A study of the transmission of ultrasound across solid-rubber interfaces. *Journal of the Acoustical Society of America*, 101(2):970–981, 1996.

[103] A. I. Lavrentyev and S. I. Rokhlin. Ultrasonic spectroscopy of imperfect contact interfaces between a layer and two solids. *Journal of the Acoustical Society of America*, 103(2):657–664, 1998.

List of Publications Arising from Thesis

P1 F. Simonetti and P. Cawley. A guided wave technique for the characterisation of highly attenuative viscoelastic materials. *Journal of the Acoustical Society of America*, 114(1):158-165, 2003.

P2 F. Simonetti and P. Cawley. Ultrasonic interferometry for the measurement of shear velocity and attenuation in viscoelastic solids. *Journal of the Acoustical Society of America*,115(1):157-164, 2004.

P3 F. Simonetti and P. Cawley. Rapid low frequency measurement of the acoustic properties of solid viscoelastic materials. In D. O. Thompson and D. E. Chimenti, editors *Review of Progress in Quantitative NDE*, Plenum Press, New York, 2003 in press.

P4 F. Simonetti, P. Cawley and and M. J. S. Lowe. Long range inspection of lossy bilayers. In D. O. Thompson and D. E. Chimenti, editors *Review of Progress in Quantitative NDE*, Plenum Press, New York, 2003 in press.

P5 F. Simonetti and P. Cawley. On the nature of shear horizontal wave propagation in elastic plates coated with viscoelastic materials. *Proc. Royal Society*, 2004 in press.

P6 F. Simonetti. Lamb wave propagation in elastic plates coated with viscoelastic materials. *Submitted to Journal of the Acoustical Society of America.*

P7 F. Simonetti and M. J. S. Lowe. On the meaning of Lamb mode nonpropagating branches. *Submitted to Proc. Royal Society.*

P8 F. Simonetti and P. Cawley. Universal charts for guided wave inspection of coated pipelines. *To be submitted.*